CARBON NANOTUBES FUNCTIONALIZED WITH DYE MOLECULES AND METAL NANOPARTICLES

PAR

Tilman ASSMUS

Dipl.-Phys., Technische Universität Darmstadt, Allemagne
et de nationalité allemande

EPFL

ÉCOLE POLYTECHNIQUE
FÉDÉRALE DE LAUSANNE

Suisse
2008

Abstract

Single-walled carbon nanotubes are highly interesting quasi one-dimensional nano-structures. They possess a multitude of fascinating optical, mechanical and electrical properties, which can be even further expanded through appropriate functionalization strategies. This thesis covers a number of functionalization strategies and their effects on the nanotube's optical and electrical properties.

The first part deals with the functionalization of carbon nanotubes with dye molecules and the characterization of the functionalized system. Both covalent and noncovalent approaches were investigated with the goal of modifying the nanotubes' photoelectrical properties. Upon excitation with light of the appropriate wavelength, a clear electrical response could be observed on some functionalized individual nanotubes. Depending on the attached dye molecule, the conductivity change is either induced by a light-induced conformational change or by a charge transfer between the nanotube and the excited dye molecule. The perspectives of constructing an optoelectronic nanoswitch based on these effects are discussed.

The second part of the thesis addresses carbon nanotubes functionalized by a low density of electrodeposited gold nanoparticles with sizes in the range between 10 and 100nm. In this case, the functionalization is targeted on amplifying the nanotube's Raman response (SERS effect). The novel sample preparation technique developed in this thesis allowed for an investigation of SERS on the level of individual molecule / nanoparticle hybrids. The optical emission spectra of the nanotube-nanoparticle hybrid structure disclosed Raman peaks associated with the nanotubes, which are superimposed on a broad luminescence background originating from the metal particles. Wavelength dependent experiments revealed maximum Raman intensity when both the nanotube and the metal particle are in optical resonance. In well-prepared samples the Raman signals collected over isolated particles exhibited an intensity enhancement by at least one

order of magnitude, as compared to bare sections on the same tube, without appreciably interfering with polarization dependent Raman measurements.

Résumé

Les nanotubes "monoparois" ("single-walled carbon nanotubes") sont des nanostructures quasi-unidimensionnelles particulièrement intéressantes. Ils possèdent un grand nombre de propriétés optiques, mécaniques, et électriques fascinantes, qui peuvent même être étendues grâce à des stratégies de fonctionnalisation appropriées. Cette thèse s'intéresse à un certain nombre de ces stratégies et à leurs effets sur les propriétés optiques et électriques des nanotubes.

La première partie concerne la fonctionnalisation de nanotubes de carbone avec des molécules colorantes et la caractérisation du système fonctionnalisé. Les approches covalentes et non-covalentes ont été étudiées dans le but de modifier les propriétés photoélectriques des nanotubes. À partir d'une excitation électromagnétique d'une longueur d'onde adaptée, une réponse électrique claire peut être observée sur certains nanotubes fonctionnalisés individuels. En fonction de la molécule colarante attachée, le changement de conductivité est soit induit par un changement de conformation dû à la lumière, soit par un transfert de charge entre le nanotube et la molécule marquée excitée. Les possibilités de construire un nanocommutateur optoélectronique à partir de ces effets seront discutées.

La deuxième partie de la thèse traite des nanotubes de carbone fonctionnalisés par une faible densité de nanoparticules d'or électrodéposées d'une taille de 10 à 100 nm. Dans ce cas, l'objectif de la fonctionnalisation est d'amplifier l'effet Raman des nanotubes (SERS). La technique innovante de préparation d'échantillon développée dans cette thèse permet l'étude du SERS au niveau des molécules individuelles ou des nanoparticules hybrides. Le spectre optique d'émission des nanotubes-structure hybride de nanoparticules laisse apparaître les pics de Raman associés aux nanotubes sur le fond étendu de luminescence des particules de métal. Des expériences faisant varier la longueur d'onde permettent de mettre en évidence le maximum de la diffusion Raman

lorsque les nanotubes et les particules de métal sont en résonance optique. Dans des échantillons bien préparés, les signaux Raman collectés à partir de particules isolées montrent une augmentation de l'intensité d'au moins un ordre de grandeur, comparé à des sections nues sur le même tube, et cela sans interférer de façon notable sur les mesures Raman dépendantes de la polarisation.

Mots clés: nanotubes de carbone, molécules colorantes, fonctionnalisation, transfert de charge, nano-commutateur, électrochimie, Raman, SERS, phonon, RBM, nanoparticules.

Contents

Contents

1 Introduction

By definition, nanotechnology deals with scales in the nm (10^{-9}m) range. In the last years nanotechnology has become a major industry with a billion dollar sales volume and products in a multitude of fields including microelectronics, cosmetics, automotive, pharmaceutical and food industries. While this development has mainly occurred within the last decade, nanotechnology has a considerably longer history: Already around the year 400 AD, the "lycurgus cup" was made by the Romans [1]. The cup is made of glass and has a greenish appearance, but when it is illuminated from within, it glows red (see Fig. 1.1). The red glow comes from gold nanoparticles embedded in the glass. At a wavelength of $\approx 520nm$ (green) collective electron oscillations (surface plasmons, see section 2.3.4 on page 23) are excited in the nanoparticles and lead to a strong absorption of the greenish light.

(a)   (b)
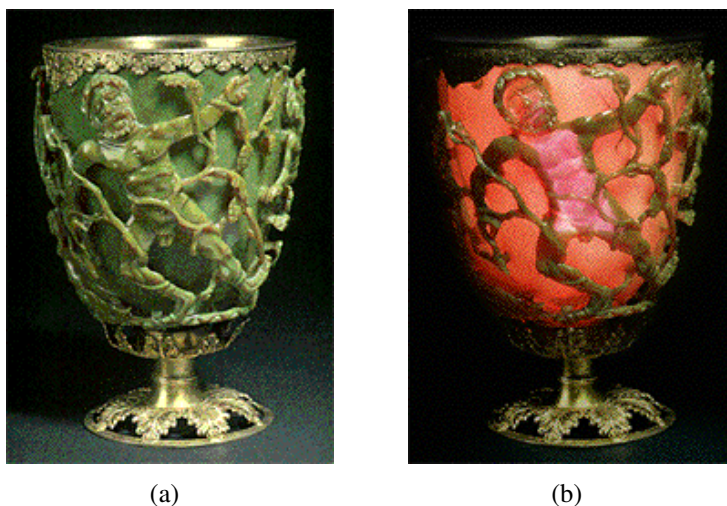
Figure 1.1: The lycurgus cup glows red when illuminated from within due to the incorporation of gold nanoparticles.

Another example of ancient nanotechnology, which has been understood only very recently, is the secret of damascus steel. This steel was mainly used for forging blades, and swords with unequalled hardness and malleability could be produced. However, after the ore mines were exploited around 1750, damascus blades could no longer be forged. Many attempts have been made to explain the extraordinary properties and to rediscover the manufacturing procedure, but only in 2006 carbon nanotubes (see section 2.2 on page 9) and cementite nanowires were found to be embedded in the damascus steel (see Fig. 1.2, [2]). It can be inferred, that the nanotubes were formed during the forging process due to rare earth impurities in the iron ore. Being the material with the highest Young's modulus known until today, carbon nanotubes might very well have contributed to the properties of damascus steel.

(a)   (b)
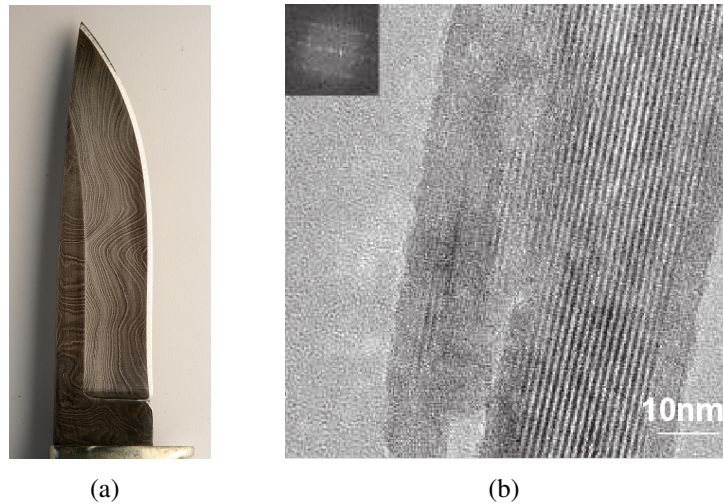
Figure 1.2: (a) Damascus blades are known for their complex wave structures (b) TEM images show carbon nanotubes and cementite nanowires embedded in the steel.

While the structures described so far contained nanosized objects, the manufacturers were unaware of their presence. The dawn of modern nanotechnology came with the idea of actually controlling the structure at the nanoscale, envisioned by Feynman in his speech "There's plenty of room at the bottom" in 1960 [3]. The invention of the scanning tunnelling microscope by Binnig and Rohrer in 1981 [4] allowed for the investigation and manipulation of surfaces with atomic precision. In the 1990s nanotechnology became one of the fastest growing research subject as well as one of the fastest growing industries.

After the (re-) discovery of carbon nanotubes by Iijima (1991) [5] and their foreseen applications in electronic circuits and sensing devices, a major branch of today's nanotechnology research is aimed towards tailoring nanotube-based structures towards specific applications. In order to create new functions on a nanotube, it is necessary to combine it with other nanostructures such as molecules or nanoparticles. Understanding and controlling the interactions between nanotubes and other nanostructures is the main focus of this thesis.

Interactions between nanotubes and molecules can be covalent or noncovalent. While the covalent interactions are more stable and therefore more favourable from an application point of view, covalent interactions also introduce defects to the nanotubes, which results in a lower electrical conductivity. For applications that require a very high conductivity, noncovalent interactions are thus better suited. However, conductivity changes induced by noncovalent interactions are usually less pronounced and therefore harder to detect than conductivity changes induced by covalent functionalizations. By attaching dye molecules to carbon nanotubes, the nanotubes' conductivity can be controlled with light, realising an optical nanoswitch.

Another interesting nanostructure hybrid system is formed by attaching individual metal nanoparticles to carbon nanotubes. Upon excitation with visible light, a surface plasmon is created in the nanoparticle, which leads to a pronounced enhancement of the nanotube's Raman signal. While this effect is known for over 30 years it has previously not been possible to study it on the individual molecule / individual nanoparticle level.

This thesis is organized as follows: The second chapter gives an overview of the properties of carbon nanotubes and possible functionalization pathways. In the third chapter the experimental methods of sample preparation, modification and analysis are discussed. The results of the functionalization of nanotubes with various dye molecules are presented in chapter four. Chapter five is devoted to the functionalization of nanotubes with metallic nanoparticles and the analysis of the nanotube-nanoparticle system by polarized confocal Raman spectroscopy. The thesis ends with a summary and discussion of the obtained results.

2 Carbon Nanotubes

2.1 Allotropes of Carbon

Carbon is an element of the 4th main group of the periodic table. Due to its half-filled L-shell, carbon can form a multitude of compounds, turning it into the element with the biggest variety of compounds. Carbon compounds are the basis for all life forms on earth. The ubiquitous presence of carbon compounds in organic material is attributed to the various bonding abilities of carbon. For a detailed understanding of the different bonding types one needs to consider the electron shell structure of the carbon atom.

(a) sp^3 hybridization   (b) sp^2 hybridization
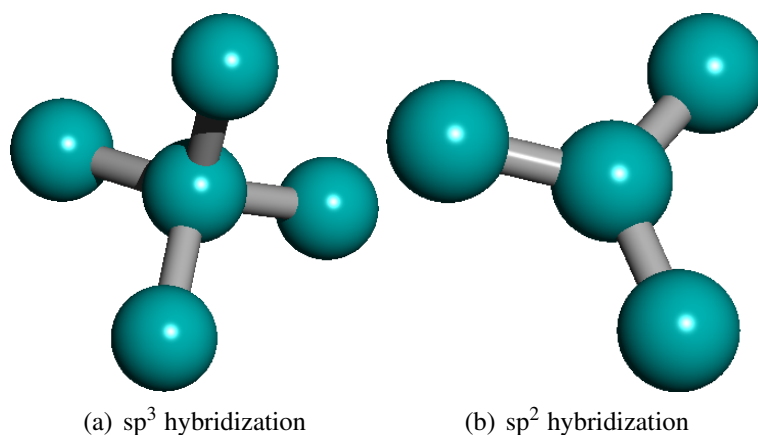
Figure 2.1: Sketch of the sp^3 and sp^2 configurations of carbon atoms. While in the sp^3 the carbon atoms form a tetrahedron and thus extends into three dimensions, the sp^2 atoms are arranged in a plane and thereby form a two-dimensional object.

Elemental carbon has six electrons. Two electrons are in the 1s shell, another two in the 2s shell. The remaining two electrons populate the $2p_x$ and $2p_y$ levels. The 2s and 2p orbitals of carbon often appear in a linear combination, they hybridize.

- In the sp^3 hybridization (Fig. 2.1 a) the three 2p levels and the 2s level form 4 sp^3 orbitals in a tetrahedral configuration. Under high pressure and temperature the carbon atoms form covalent bonds and crystallize in a fcc structure (Fig. 2.2). Due to the strong σ-bonds between the carbon atoms diamond is extremely stable (melting point: 3547°C). The name diamond comes from the ancient Greek word adamas (later on translated as diamas), meaning impregnable.
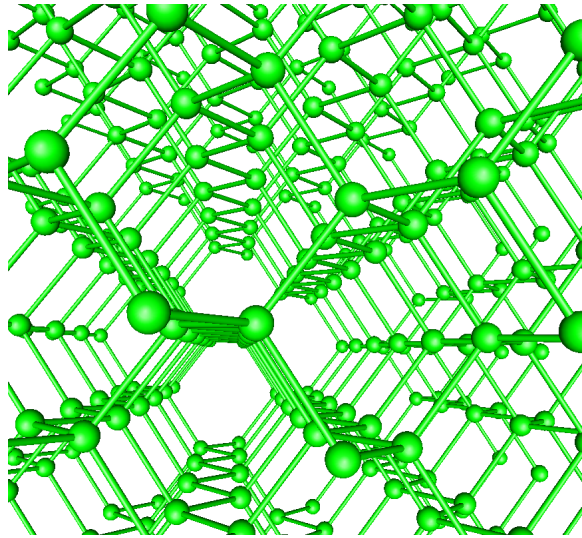
Figure 2.2: 3D view of a diamond lattice.

- In the sp^2 configuration (Fig. 2.1 b) hybridization occurs between two 2p levels and the 2s level. The resulting three sp^2 orbitals arrange in a plane orthogonal to the remaining 2p orbital and form an equilateral triangle. Thus, σ-bonds are only formed in one plane. Several interesting carbon allotropes comprising the sp^2 bond have been discovered:

    - A two-dimensional layer of carbon atoms using the sp^2 bonding is called a graphene sheet (Fig. 2.3). When graphene sheets are stacked via van-der-Waals interactions, the well-known graphite (in ancient Greek graphein means writeable) is formed (Fig. 2.4).

    - In 1985 it was observed, that sp^2 hybridized carbon also exists in near-spherical assemblies [7], the fullerenes or buckyballs. A prominent example is C_{60}, but also much larger versions like C_{720} exist (Fig. 2.5). The carbons are arranged into truncated icosahedral shape. The names fullerenes or
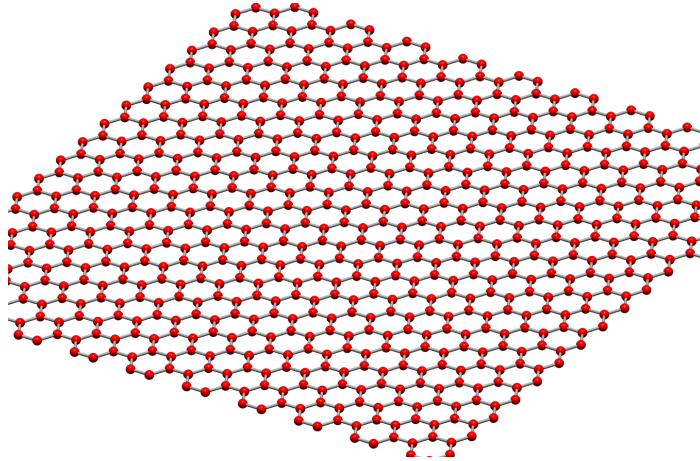
Figure 2.3: A single layer of graphene. The carbon atoms are arranged in a hexagonal (honeycomb) lattice. The atom to atom distance is $1.41\mathring{A}$
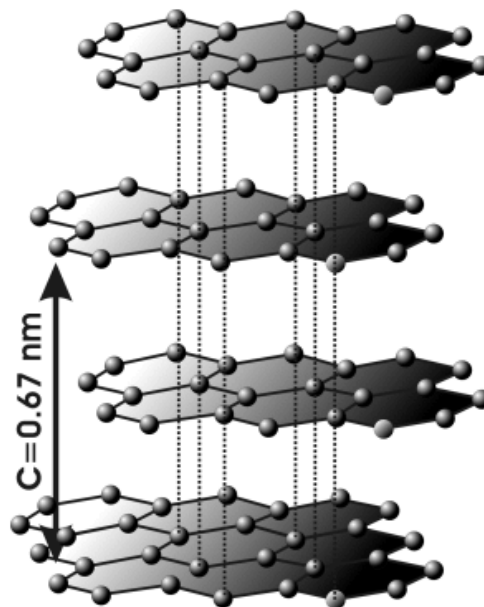
Figure 2.4: The sketch shows stacked graphene layers, the constituents of graphite [6].

buckyballs come from the architect Richard Buckminster Fuller, who built geodetical domes, which resemble the shape of the carbon spheroids. While planar graphene sheets are known to be quite unreactive, in fullerenes the sp^2-hybridized carbon atoms have to be bent in order to form the near-spherical structure. The hereby induced angular strain renders the fullerenes more reactive. For the discovery of fullerenes Harold Kroto, Robert Curl and Richard Smalley were awarded the 1996 Nobel Prize in Chemistry.

(a) C_{60} fullerene
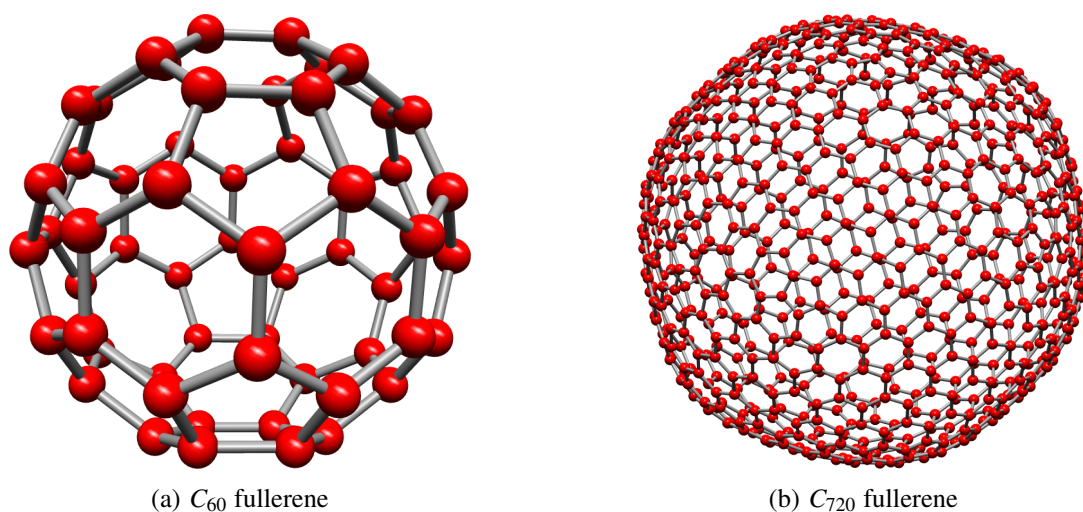
(b) C_{720} fullerene

Figure 2.5: Fullerenes exist in a great variety of shapes and sizes. One of the smallest fullerenes, and possibly the most famous one, is shown in (a), the C_{60} fullerene. A large fullerene made out of 720 carbon atoms (C_{720}) is depicted in (b).

– Probably the most prominent sp^2 hybridized carbon structures are carbon nanotubes (Fig. 2.6). Until recently it was generally agreed that they were discovered in 1991 by Iijima [5], but it has been shown lately [8], that already as early as 1952 Radushkevich and Lukyanovich published TEM images of nanosized, tubular carbon structures, most likely being multi-walled carbon nanotubes [9]. Additionally, in 1974 carbon filaments most likely comprising multiwall carbon nanotubes were observed by Endo [10]. Nanotubes can be thought of being graphene sheets that are rolled into a tubular structure and have half-fullerene like caps at the ends. Carbon nanotubes have very interesting mechanical as well as electrical properties, which will be discussed in the next section.
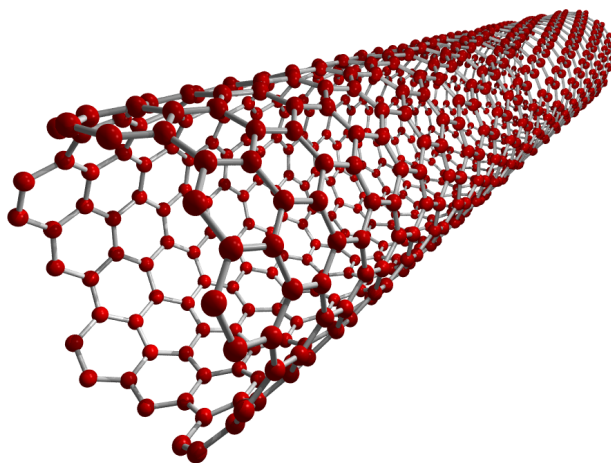
Figure 2.6: A single-walled nanotube

- The sp^1 hybridization does not exist in elementary carbon structures. It is quite common for compounds (e.g. ethine), however (Fig. 2.7).
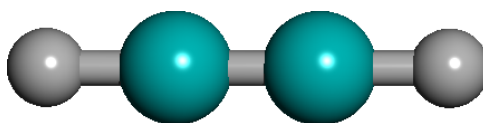
Figure 2.7: Ethine is the most simple molecule with a $C \equiv C$ bond. This bonding type does not exist in carbon-only structures. Colour code:. Carbon: cyan, Hydrogen: grey

Though many carbon allotropes possess intriguing properties and are the subject of active research, the following sections will focus on the properties of carbon nanotubes.

2.2 Structure and properties of Carbon Nanotubes

2.2.1 Structure of Carbon Nanotubes

Carbon Nanotubes have many unique electronic and mechanical properties. They have the highest Young's modulus of all known materials (>1TPa) [11], their tensile

strength is a hundred times that of steel (150GPa)[12], their maximum electrical current density is 100 times greater than that of copper wires ($> 10^9 A/cm^2$) [13] and the room temperature hole mobility is larger than that of silicon ($10^5 cm^2/Vs$) [14].
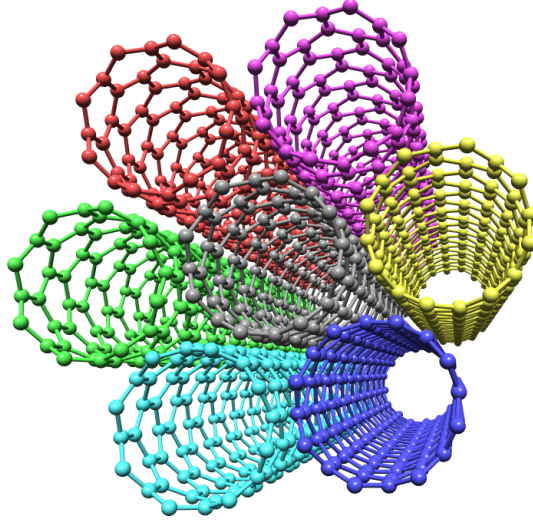
Figure 2.8: Nanotubes usually appear in bundles, which stick together due to $\pi - \pi$ interactions (Fig. 2.8). In order to analyse the properties of a single nanotube it is necessary to debundle the nanotube agglomeration (see section 3.1.1)

Carbon nanotubes are almost perfect one-dimensional objects: With a typical diameter of one nm and maximum lengths in the cm range [15, 16] their aspect ratio (i. e. length to width quotient) can exceed 10^7, rendering them an ideal subject for basic and applied research in 1D phenomena. Their walls consist of a hexagonal (*honeycomb*) lattice of carbon atoms in the sp^2 configuration. While carbon nanotubes can consist of many layers of rolled-up graphene sheets (multi-walled carbon nanotubes, see Fig. 2.9), single-walled carbon nanotubes are the most promising candidates for applications in electronic circuits. Single-walled carbon nanotubes can be classified according to the way the graphene sheet is rolled up. The unit cell vectors of a graphene sheet $\vec{a}_1$ and $\vec{a}_2$ define the chiral vector $\vec{C}_h$:

$$\vec{C}_h = n\vec{a}_1 + m\vec{a}_2 \tag{2.2.1}$$

with $n \geq m$. $\vec{C}_h$ is usually represented by the integer pair (n,m) and uniquely defines a particular nanotube. $\vec{C}_h$ also defines the roll-up direction of the graphene sheet. The
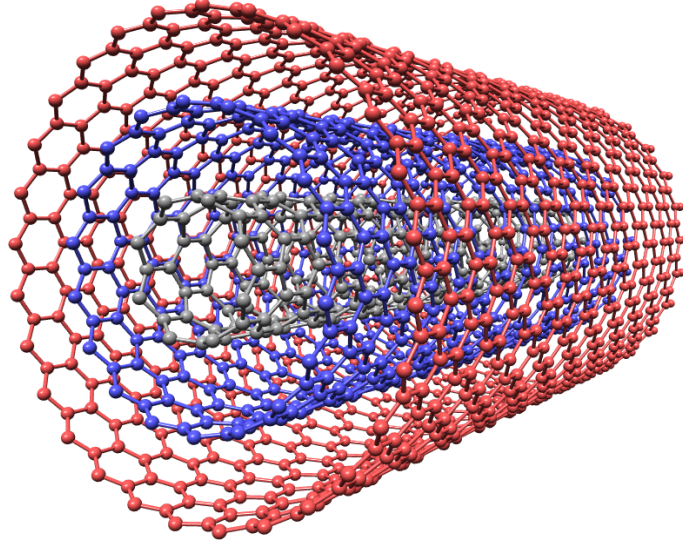
Figure 2.9: Depending on the growth conditions, nanotubes can be single-walled, double-walled or multi-walled.

angle between $\vec{C}_h$ and lattice vector $\vec{a}_1$ is given by

$$\Theta = \arctan\left(\frac{\sqrt{3}m}{m+2n}\right) \tag{2.2.2}$$

The unit vectors of the underlying graphene sheet are given by

$$\vec{a}_1 = a_0\left(\frac{\sqrt{3}}{2}, \frac{1}{2}\right) \qquad \vec{a}_2 = a_0\left(\frac{\sqrt{3}}{2}, -\frac{1}{2}\right) \tag{2.2.3}$$

with $a_0 = 2.461\text{Å}$. The nanotube diameter can be calculated as follows:

$$d = \frac{a_0}{\pi}\sqrt{n^2 + nm + m^2} \tag{2.2.4}$$

This equation is valid for nanotubes with a sufficiently large diameter. For small nanotubes ($\varnothing \lesssim 1nm$), strain-induced deviations from this rule occur [17]. The nomenclature of single-walled carbon nanotubes is as follows: The mirror-symmetric nanotubes are divided into the $n = m$ "armchair nanotubes" and the $m = 0$ "zigzag nanotubes". All other nanotubes exist as two enantiomers and are therefore called "chiral" nanotubes.
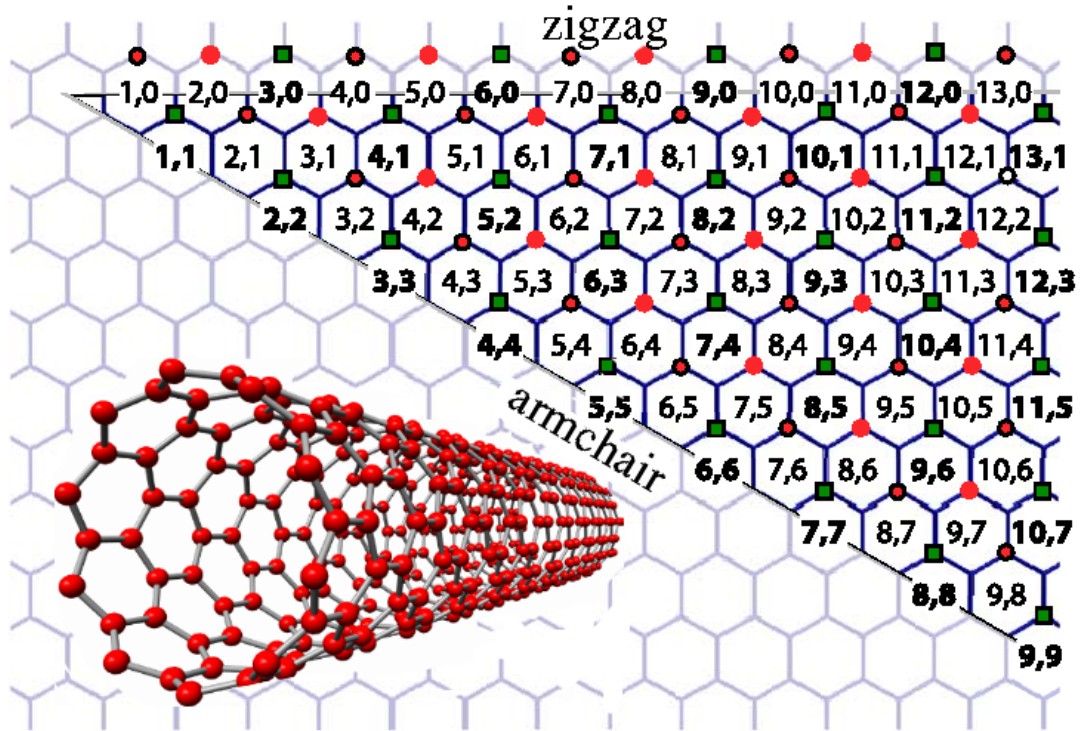
Figure 2.10: Depending on the roll-up direction, a nanotube can have different properties. In the figure, the roll-up direction $\vec{C}_h$ is given by the connection between (0,0) and the corresponding chiral index (n,m). In this manner, the most common chiral indices are mapped on a graphene sheet. Metallic nanotubes are labelled green, semiconducting tubes are libelled in red. The figure illustrates the distribution of semiconducting and metallic nanotubes. Whereas by following the zigzag roll-up direction semiconducting as well as metallic nanotubes can be found, all nanotubes in the armchair roll-up direction are metallic.

The number of carbon atoms per unit cell is given by

$$n_c = \frac{4(n^2 + nm + m^2)}{\nu R} \qquad (2.2.5)$$

$$\text{where } \nu = gcd(n,m) \text{ and } R = \begin{cases} 3 & \text{if } \frac{n-m}{3\nu} \in \mathbb{N} \\ 1 & \text{otherwise} \end{cases}$$

with gcd being the greatest common denominator. Using equation 2.2.5 it can be shown, that even seemingly similar tubes like (n,m) and (n,m-1) can have very different unit cells. For example, while the (10,10) nanotube has only 40 atoms in the unit cell, the (10,9) nanotube unit cell comprises 1084 atoms.

The electronic structure of carbon nanotubes can be determined from that of graphene (Fig. 2.12) by the zone-folding approach, which uses periodic boundary conditions on the energy dispersion relation of graphene [18, 19]. The boundary conditions account for the quasi-1D nature of the nanotubes, which allows continuous wave vectors only along the nanotube axis. Thus, the energy dispersion relation for the nanotube is a set of one-dimensional dispersion relations:

$$E_{CNT,\mu}(k) = E_{\text{graphene}}(k) \left(k\frac{\vec{K}_2}{|\vec{K}_2|} + \mu\vec{K}_1 \right) \qquad (2.2.6)$$

$$\text{with } \mu \in [1,N] \text{ and } k \in [-\pi/T, \pi/T]$$

Using the dispersion relation for graphene obtained from tight-binding calculations and a value of $\approx 3eV$ for the tight-binding exchange integral t, the energy dispersion relation can be expressed as [20]

$$E_{\text{graphene}}(k_x, k_y) = \pm t \sqrt{1 + 4\cos\left(\frac{\sqrt{3}}{2}k_x a\right) \cos\left(\frac{1}{2}k_y a\right) + 4\cos^2\left(\frac{1}{2}k_y a\right)} \quad (2.2.7)$$

This equation comprises the conduction band (π^*, $E > 0$) and the valence band (π, $E < 0$) of the graphene sheet. It is plotted in Fig. 2.13. For an armchair and a zig-zag

(a)

(b)

(c)
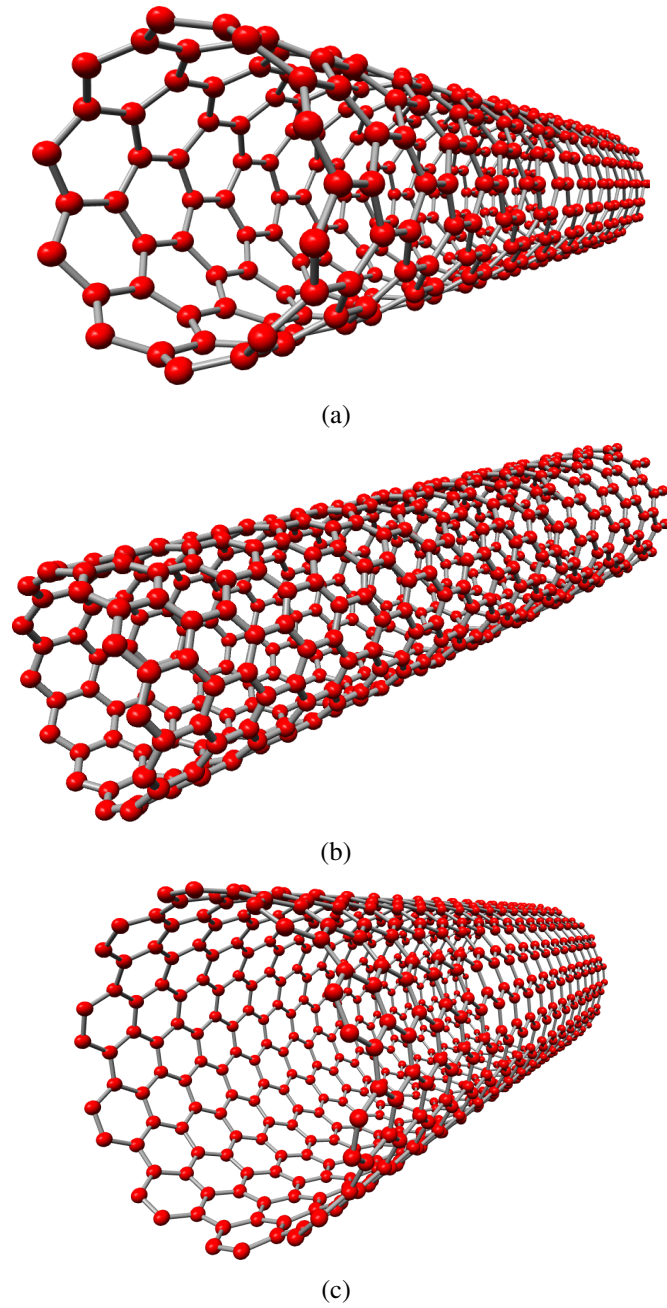
Figure 2.11: (a) The (10,0) semiconducting zigzag nanotube ($\varnothing \approx 0.8nm$). (b) The (12,0) metallic zigzag nanotube ($\varnothing \approx 0.9nm$). (c) The (10,10) metallic armchair nanotube ($\varnothing \approx 1.4nm$).

(a)

(b)

(c)
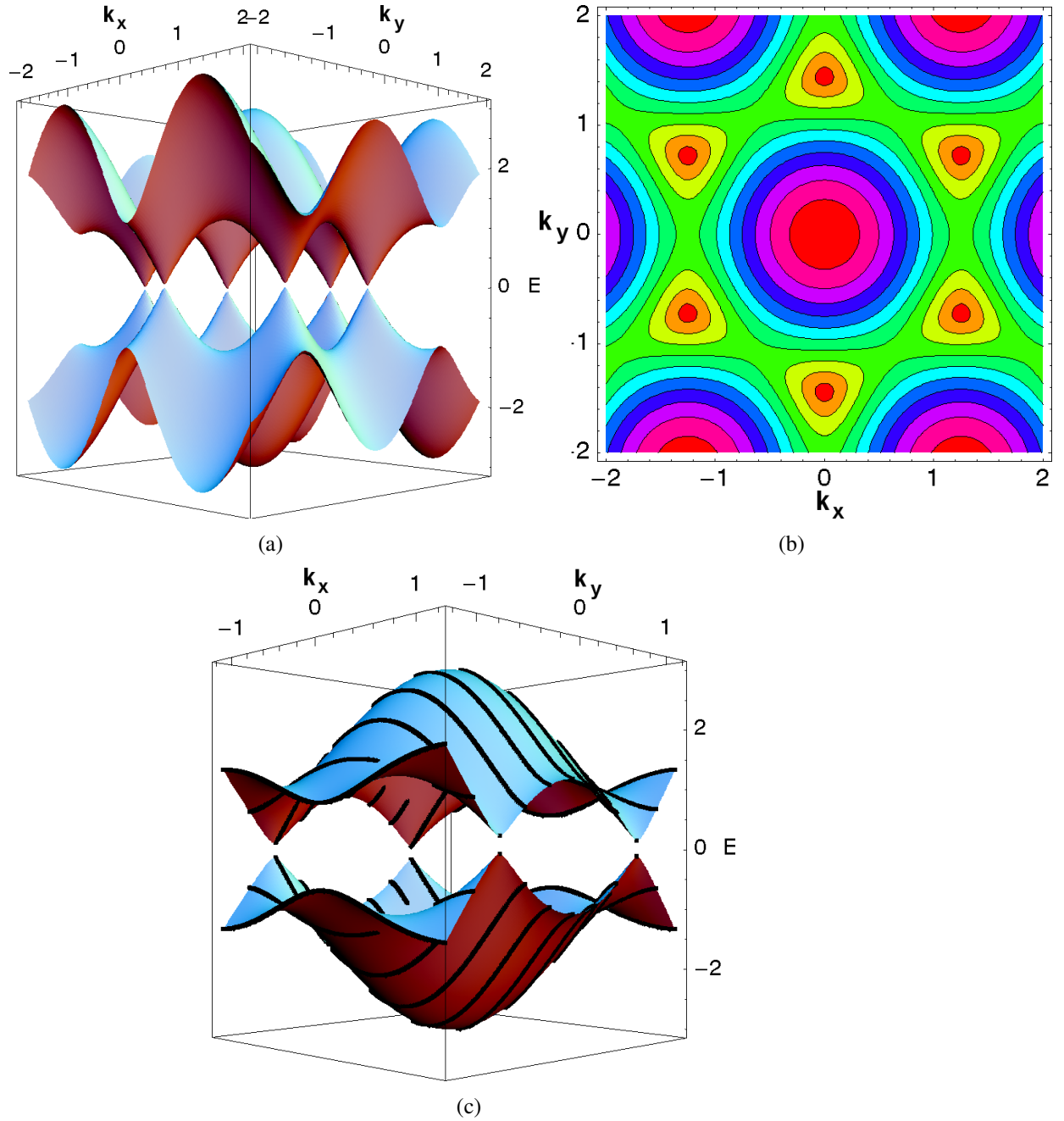
Figure 2.12: (a) The dispersion relation of graphene can be used to determine the dispersion relation of carbon nanotubes by a zone-folding approach. (b) Contour plot of the graphene dispersion relation. (c) Illustration of the slicing of the graphene dispersion relation to obtain the dispersion relations of a carbon nanotube.)

nanotube, the one-dimensional dispersion relation is given by [19]:

$$E_{\text{armchair CNT}}(k) = \pm t \sqrt{1 \pm 4 \cos\left(\frac{q\pi}{n}\right) \cos\left(\frac{ka}{2}\right) + 4 \cos^2\left(\frac{ka}{2}\right)} \quad (2.2.8)$$

$$\text{with } k \in [-\pi/a, \pi/a] \text{ and } q \in [1, 2n]$$

$$E_{\text{zig-zag CNT}}(k) = \pm t \sqrt{1 \pm 4 \cos\left(\frac{q\pi}{n}\right) \cos\left(\frac{\sqrt{3}ka}{2}\right) + 4 \cos^2\left(\frac{q\pi}{n}\right)} \quad (2.2.9)$$

$$\text{with } k \in [-\pi/\sqrt{3}a, \pi/\sqrt{3}a] \text{ and } q \in [1, 2n]$$

From the energy dispersion relations the electronic density of states (EDOS) can be calculated according to [21] as

$$n(\varepsilon) \propto \sum_i \int dk \delta(k - k_i) \left| \frac{\partial E_{\text{CNT}}(k)}{\partial k} \right|^{-1} \quad (2.2.10)$$

where the k_i are the roots of $\varepsilon - E(k) = 0$. Figure 2.14 summarizes the results of this calculation. The EDOS of carbon nanotubes shows the following interesting features:

- The EDOS displays singularities, known as the *van Hove* singularities [22]. The spacing between the van Hove singularities determines the optical absorption and emission properties: Whenever the wavelength of the excitation light matches the energy difference of two mirror-like van Hove singularities, it can be resonantly absorbed. By plotting the energy difference of two corresponding van Hove singularities $E_{ii}^{m,s}$ versus the nanotube diameter according to [23] one obtains the so-called *Kataura* plot 2.16. Based on this plot it can be shown, that the $E_{ii}^{m,s}$ exhibit a linear dependence on the inverse nanotube diameter (see section 2.3.2 on page 22).

- Whereas some nanotubes have a vanishing EDOS around the Fermi energy, others retain a finite EDOS. The first group of nanotubes is called semiconducting nanotubes. Nanotubes with finite EDOS at the Fermi energy are metallic. The different EDOS at the Fermi level reflects the different dispersion relations: If one of the 1D dispersion relation curves crosses the K-point, where π and π^* band
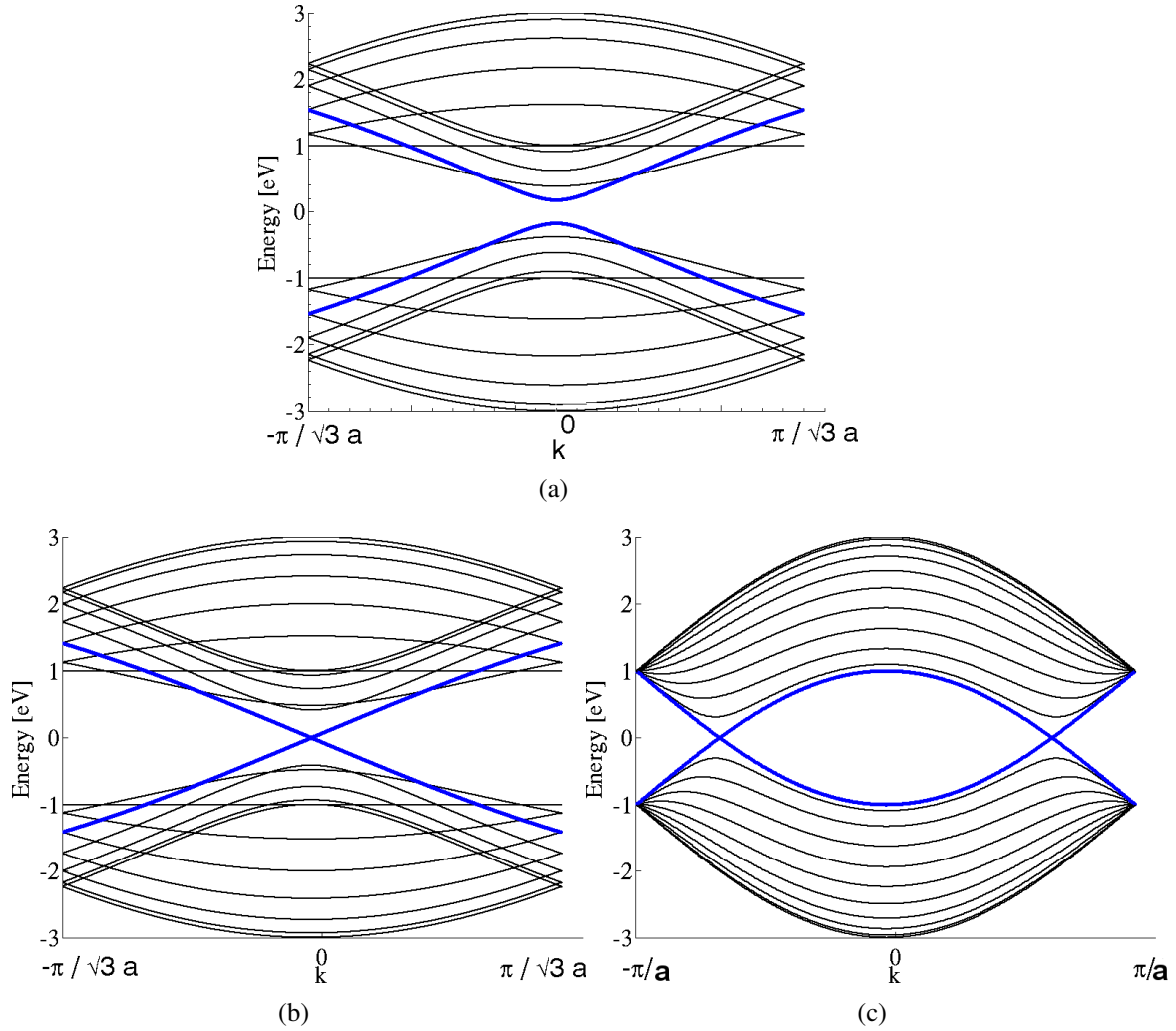
Figure 2.13: (a) Dispersion relation of a (10,0) semiconducting zigzag nanotube. The energy gap between the dispersion relations is responsible for the semiconducting behaviour. (b) Dispersion relation of a (12,0) metallic zigzag nanotube. No band gap is observed. (c) Dispersion relation of a (10,10) metallic armchair nanotube. The dispersion bands cross at different points compared to a metallic zigzag nanotube.
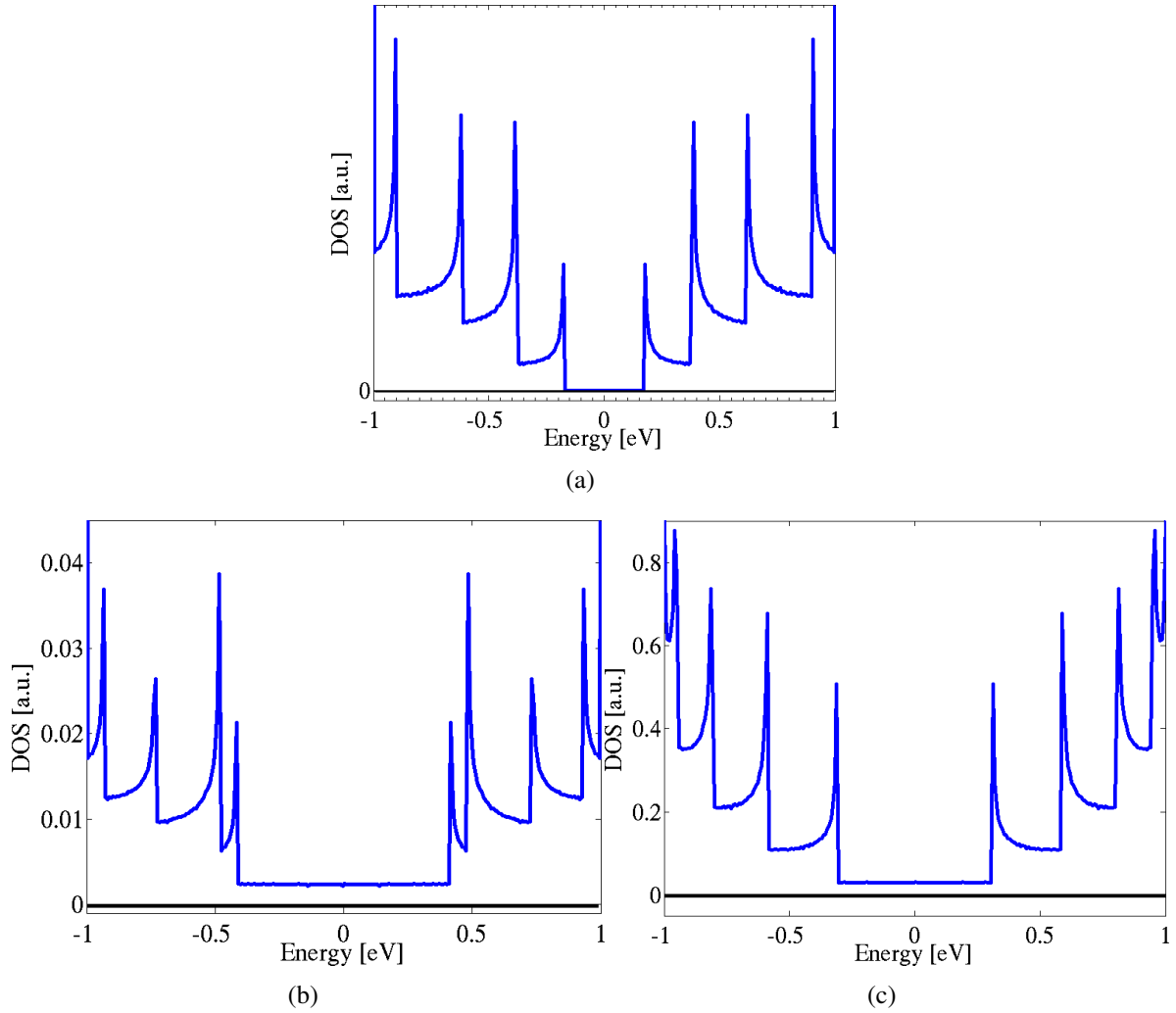
Figure 2.14: (a) EDOS of a (10,0) semiconducting zigzag nanotube. The EDOS is 0 around the Fermi energy, which gives rise to a bandgap. (b) EDOS of a (12,0) metallic zigzag nanotube. The EDOS retains a finite value around the Fermi level. (c) EDOS of a (10,10) metallic armchair nanotube. The metallic behaviour is evident from the absence of a bandgap around the Fermi energy.

are degenerate, then the EDOS at the Fermi energy is finite and the nanotube therefore metallic (Fig. 2.13). It can be shown that the following condition must be fulfilled in order for a tube to be metallic:

$$m - n = 3i \ (i \in \mathbb{N}^0) \tag{2.2.11}$$

with $\mathbb{N}^0$ being the natural numbers including zero. Otherwise ($m - n \neq 3i$), the nanotube is semiconducting. From the above equation it is evident, that all armchair nanotubes (n,n) are metallic, whereas zig-zag (n,0) and chiral (n,m) nanotubes can be metallic or semiconducting depending on equation 2.2.11 [24, 25].

2.2.2 Phonon modes

Phonon modes are quantized vibrational modes in condensed matter systems. They affect many material processes including transport and mechanical properties. Similar to the electronic structure the phonon structure of carbon nanotubes can be derived from that of graphene via zone-folding. With N being the number of carbon hexagons in the unit cell, there are 2N atoms in a unit cell, each of them with three degrees of freedom, accounting for 6N phonon branches in the phonon dispersion relations. However, due to mode degeneracies, the actual number of distinct phonon modes is often lower: For example, the (10,10) nanotube possesses 120 vibrational degrees of freedom, but only 66 phonon modes [26].

While zone-folding of the graphene phonon dispersion relation gives good results for many phonon modes, the method does not reproduce all possible vibrational modes of the carbon nanotubes. The most prominent example is the *radial breathing mode* (RBM) of carbon nanotubes, which originates from a tangential out-of plane acoustic mode in graphene. Furthermore, for flat graphene sheets the in-plane and out-of-plane phonon modes do not couple, whereas coupling readily occurs for rolled-up graphene sheets (nanotubes).

(a) Rayleigh scattering   (b) Stokes scattering   (c) Anti-Stokes scattering
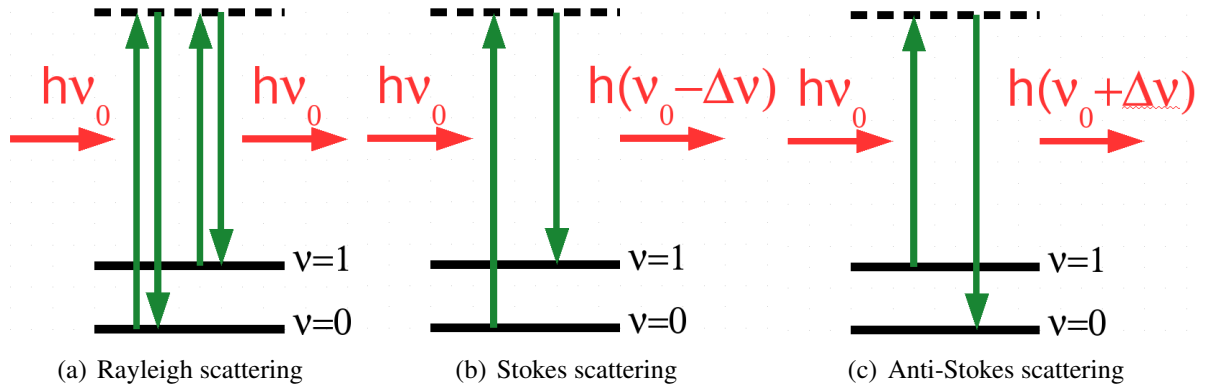
Figure 2.15: Illustration of the different terms in Eq. (2.3.3). The diagram comprises the vibronic ground state ($v = 0$), an excited vibronic state ($v = 1$) and an excited virtual state. For Rayleigh scattering (a) there is no change in energy for the reflected light, while for Stokes (b) and Anti-Stokes (c) scattering there is an energy decrease and increase, respectively.

2.3 Raman Spectroscopy of Carbon Nanotubes

2.3.1 The Raman effect

Sir Chandrasekhara Venkata Raman was awarded with the Nobel Prize in Physics in 1930 for the discovery of the Raman effect in light scattered from molecules: Unlike for Rayleigh scattering, where most photons are scattered elastically, i.e. with the same energy as the excitation photon in Raman scattering one in $\sim 10^7$ photons is scattered at a different energy, which is referred to as inelastic scattering [27, 28]. The difference in energy is due to an interaction with excitations of the molecules. In the case of vibrational Raman spectroscopy theses excitations are phonons. During the Raman scattering process the molecule is excited into a virtual state (Fig. 2.15).

Even though a detailed understanding of the Raman effect requires a quantum mechanical treatment, the classical description already gives a number of useful insights: When a molecule is placed inside an electric field $\vec{E}$, a dipole moment is induced according to

$$\vec{\mu} = \alpha \vec{E} \tag{2.3.1}$$

with α being the polarizability of the molecule. Since $\vec{E}$ is time-dependent according to

$\vec{E} = \vec{E}_0 \cos(2\pi\nu_0 t)$ the induced dipole moment becomes

$$\vec{\mu} = \alpha\vec{E}_0 \cos(2\pi\nu_0 t) \tag{2.3.2}$$

So far, internal motions (oscillations, rotations) of the molecule were not considered. If these exist, the polarizability α is modulated periodically ($\alpha = \alpha(q)$ $q = q_0 \cos(2\pi\nu_M t)$). In order to determine the predominant effects in the modulation of α, a Taylor expansion depending on the oscillation coordinate q is performed:

$$\vec{\mu} = \underbrace{\alpha_{q=0}\vec{E}_0 \cos(2\pi\nu_0 t)}_{\text{Rayleigh}} + \tag{2.3.3}$$

$$\underbrace{\frac{1}{2}\frac{\partial\alpha}{\partial q}\vec{E}_0 \left(\cos(2\pi(\nu_0 - \nu_M)t)\right)}_{\text{Stokes}} +$$

$$\underbrace{\frac{1}{2}\frac{\partial\alpha}{\partial q}\vec{E}_0 \left(\cos(2\pi(\nu_0 + \nu_M)t)\right)}_{\text{Anti-Stokes}} + \ldots$$

The first term of this equation is responsible for Rayleigh scattering, whereas the second term describes Stokes Raman scattering and the third the Anti-Stokes Raman scattering. While classical theory predicts the occurrence of these terms correctly, it fails to describe their intensity appropriately: According to the classical picture, Stokes Raman and Anti-Stokes Raman lines should have the same intensity. However, experiments show, that Anti-Stokes lines are usually much weaker than the corresponding Stokes lines, except for elevated temperatures.

To account for the different intensities, quantum-mechanical effects have to be considered. Depending on the initial state in the molecule, either a phonon is absorbed (molecule in excited vibronic state, Anti-Stokes scattering) or created (molecule in vibronic ground state, Stokes scattering) by the photon. If one assumes the molecule to be in thermal equilibrium the probability to find a molecule in a certain state follows the Boltzmann law $\left(\propto \exp\left(-\frac{E}{kT}\right)\right)$ and therefore the population of the higher level vibronic states, which is required for Anti-Stokes scattering, is much lower than the population of the ground state, which is required for Stokes scattering. At room temperature
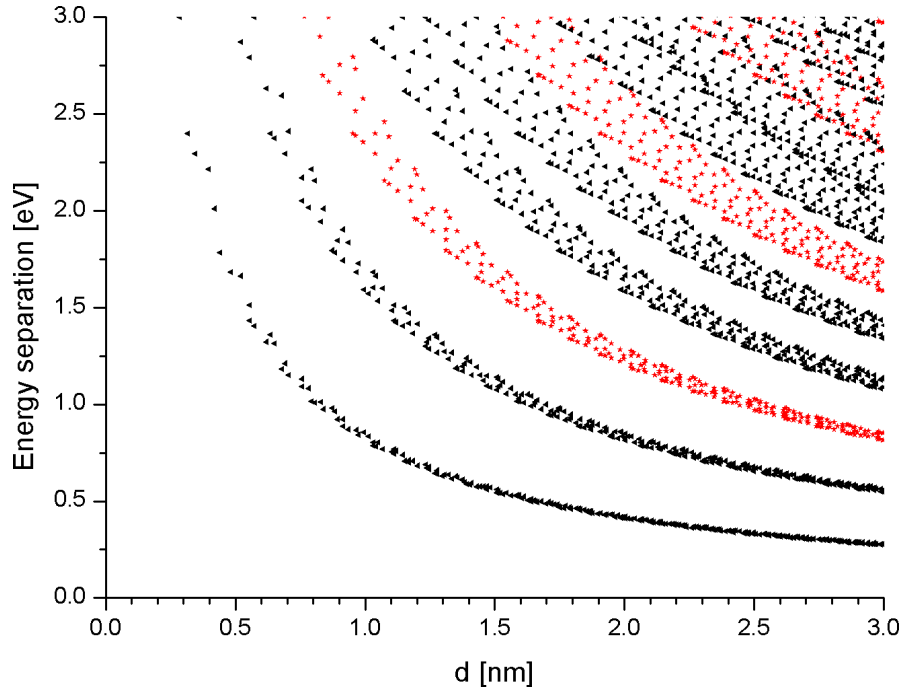
Figure 2.16: Kataura plot (optical transition energies versus nanotube diameter). The black symbols belong to semiconducting nanotubes, whereas the red symbols indicate metallic nanotubes [23].

this effect gives rise to a strongly reduced Anti-Stokes Raman line compared to the Stokes line. In fact, for non-resonant processes the temperature of a molecule can be determined from the ratio between Stokes and Anti-Stokes Raman intensity.

2.3.2 Resonance Raman Scattering (RRS)

In RRS the energy of the incoming photon is chosen in such a way that it matches an electronic transition in the molecule. In this case, the molecule is not excited into a virtual state, but into a real state. This effect leads to a pronounced enhancement of the observed Raman modes. Depending on whether the resonance occurs for the incoming or the scattered photons, resonance Raman scattering is classified as *"incoming resonance"* or *"outgoing resonance"*. If both resonance conditions are fulfilled simultaneously, a further enhancement of the Raman signal is observed: *"Double Resonance Raman scattering"* [29].

The *"Kataura"* plot is widely used to illustrate RRS for carbon nanotubes [23]. The plot relates the optical transition energies $E_{ii}^{s,m}$ to the nanotube diameter. The transition

energies depend on the energy differences of the van Hove singularities (Fig. 2.14). In a Kataura plot, transition energies for metallic or semiconducting nanotubes fall approximately on hyperbolas (Fig. 2.16).

With the help of a Kataura plot, it is possible to identify the chirality of a carbon nanotube, while the RBM frequency allows to extract the diameter of the nanotube. The diameter and the laser excitation wavelength (optical transition energy) uniquely define a point in the Kataura plot. The nanotube, which is closest to this point in the Kataura plot is the most likely type of the nanotube. However, in order for this method to work properly, deviations from the standard Kataura plot due to curvature, and many-particle interactions have to be taken into account. A modified Kataura plot, which shows good agreement between theory and experiment, is depicted in Fig. 2.17 [30, 31]. While this plot has a significantly narrowed diameter and excitation energy range, it enables a much more reliable chiral assignment of nanotubes in this window.

2.3.3 Classification of Raman modes

The Raman modes of carbon nanotubes can be classified according to the number of scattering events. If the incoming photon undergoes exactly one inelastic scattering the process is referred to as a *"first order process"*. Second order processes can either consist of two inelastic scatterings or one inelastic and one elastic scattering. A major difference between first order and higher order Raman scattering is, that for first order scattering only Γ-point phonons from the centre of the Brillouin zone $(q = 0)$ contribute, whereas for higher order scattering also non-centre phonons $(q \neq 0)$ contribute to the Raman signal.

2.3.4 Surface-Enhanced Raman Scattering (SERS)

Surface-Enhanced Raman Scattering was first observed in 1974 by Fleischman [32]: When adsorbed on a roughened silver surface pyridine molecules show strongly enhanced Raman spectra. Shortly after the discovery of the effect two different models were proposed in order to explain the effect: Jeanmarie and Van Dyne in 1977 proposed a model based on electromagnetic interactions [33], whereas Albrecht and Creighton [34] ascribed SERS to charge transfer. Interestingly, it has been experimentally found that both enhancement mechanisms can play a simultaneous role in experiments [35, 36].
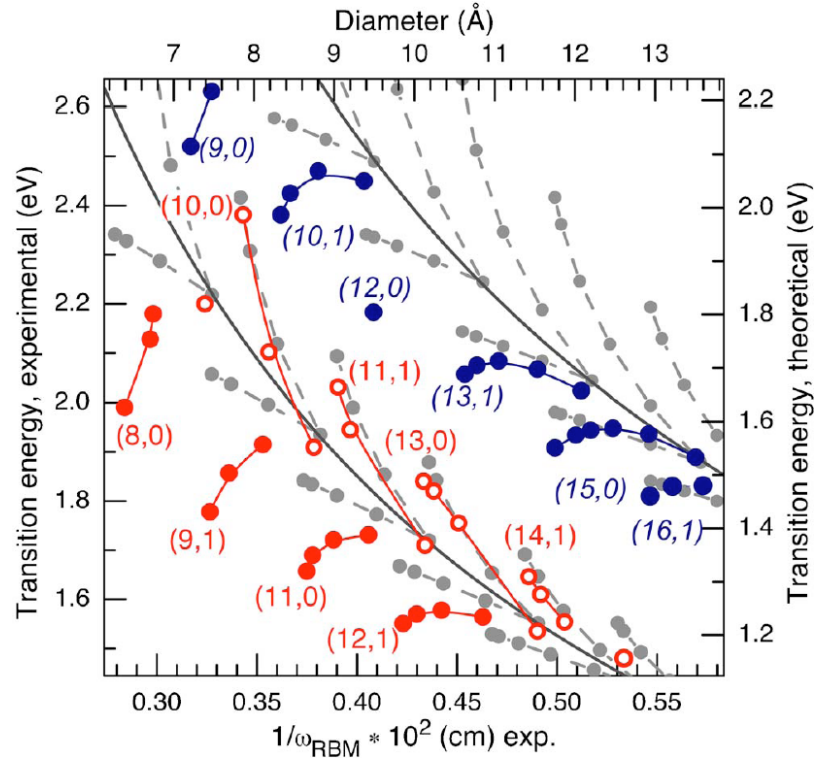
Figure 2.17: Modified Kataura plot which accounts for energy shifts due to curvature effects, electron-electron and electron-hole interactions. While the latter two are responsible for the periodic "branching" of the Kataura plot, curvature effects become significant only for small diameter nanotubes. The figure shows experimental values for the first semiconducting resonance E_{11}^s (open and closed red circles) and the second metallic resonance E_{22}^m. The corresponding theoretical values (calculated with DFT) are shown in grey [30].
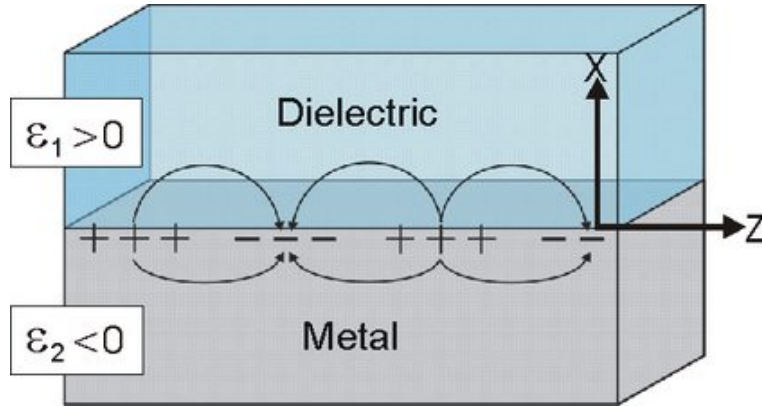
Figure 2.18: Surface plasmon resonances can exist at the metal air interface, if the prerequisites of Eq. (2.3.4) are fulfilled [38].

2.3.4.1 Electromagnetic Enhancement

The electromagnetic enhancement, which is agreed to be the dominant contribution to surface-enhanced Raman scattering, relies on the excitation of a surface plasmon on a metal surface [37]. Surface plasmons are collective excitations of the electron gas in the metal that are induced by an external electromagnetic field. For coinage metals like silver, gold and copper, the excitation wavelength must be in the visible light range (450-650nm). Surface plasmons can only be excited, if

$$\varepsilon_{\text{material 1}} \cdot \varepsilon_{\text{material 2}} \quad < \quad 0 \tag{2.3.4}$$

$$\varepsilon_{\text{material 1}} + \varepsilon_{\text{material 2}} \quad < \quad 0 \tag{2.3.5}$$

These relations hold true especially for air - metal interfaces, since $\varepsilon_{\text{air}} = 1$ and $\varepsilon_{\text{metal}} < 0$. Additionally, in order to fulfil energy and momentum conservation, one either has to make use of a prism configuration (e.g. Kretschmann type in Fig. 2.19a), or use a corrugated, roughened or nanostructured surface (2.19b). Experimentally, mainly gold and silver structures are used to study surface-enhanced Raman scattering, since for these metals the surface plasmon resonance lies in the visible range and because they are reasonably stable against oxidation under ambient conditions.

The surface plasmon is associated with an electromagnetic nearfield around the metal structure, which can interact with both the excitation photons and the Raman scattered

(a) Surface plasmon generation in a Kretschmann-type setup

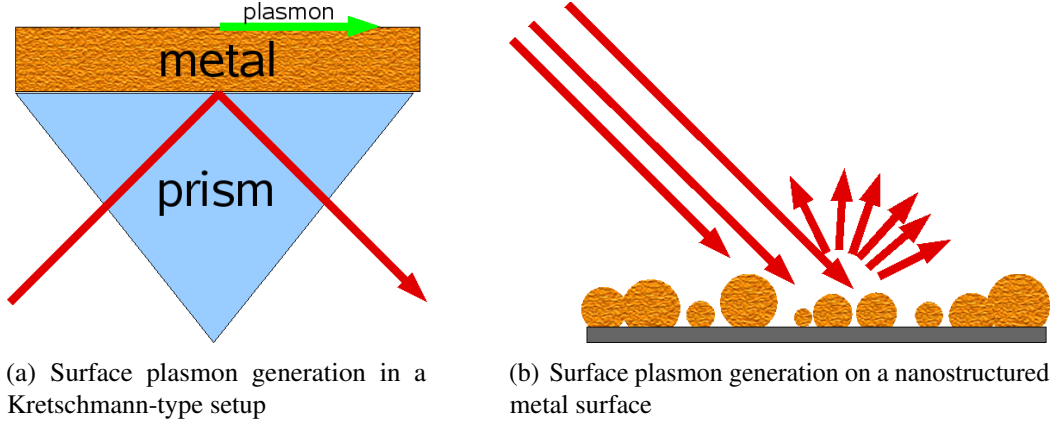(b) Surface plasmon generation on a nanostructured metal surface

Figure 2.19: Surface plasmons can be created by using a Kretschmann configuration (a) or by using a nanostructured metal surface (b).

photons. The total Raman enhancement is the product of the enhancement factor for the incoming photons ($f(\omega_0)$) and the enhancement factor for the Raman scattered photons ($f(\omega_0 \pm \omega_{\text{vib}})$).

$$I \sim |f(\omega_0)|^2 |f(\omega_0 \pm \omega_{\text{vib}})|^2 \sim |E|^4 \qquad (2.3.6)$$

Since $\omega_{\text{vib}} \ll \omega_0$ and therefore $|f(\omega_0)|^2 \approx |f(\omega_0 \pm \omega_{\text{vib}})|^2$ the surface-enhanced Raman intensity approximately scales with the fourth power of the electric field. The electric field strongly depends on the morphology of the sample. For individual nanoparticles, kinks and corners can give rise to a locally enhanced electric field (Fig. 2.20a,b). For more complex morphologies cavity effects can lead to a significant field enhancement, as depicted in Fig. 2.20c. In order to achieve maximum enhancement, agglomerations of nanoparticles are often used in experiments (Fig. 2.20d). It is likely, that cavity effects occur between some of the nanoparticles, giving rise to so-called *"hot-spots"*, where a pronounced Raman enhancement can be observed.

2.3.4.2 Chemical Enhancement

While it is widely agreed that the previously described electromagnetic enhancement is the predominant enhancement mechanism there are a number of experiments that point to a significant chemical enhancement contribution. For example, *CO* and N_2
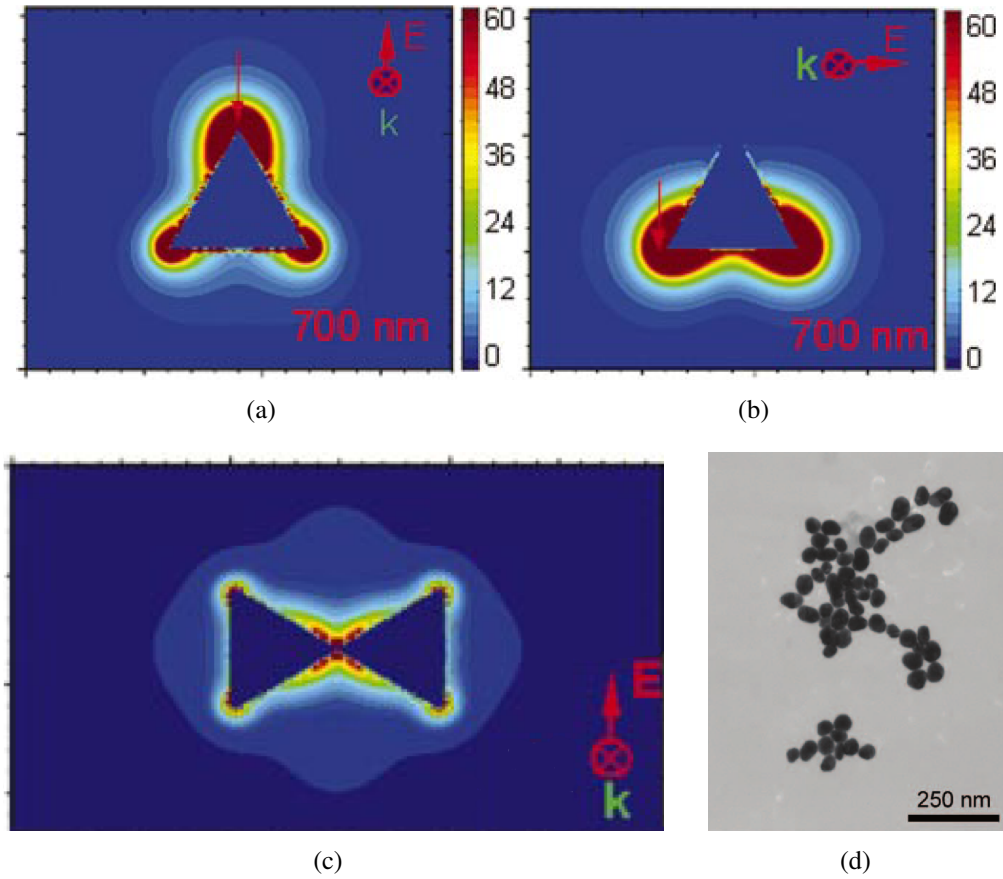
Figure 2.20: (a)(b) The figures are the simulated result of illuminating a nanosized gold triangle from different positions, as denoted in the figures. (c) The surface plasmons are strongly enhanced, if two triangles are at a distance of a few nm from each other [39]. (d) Colloidal gold nanoparticles are frequently used to study SERS [40].

molecules differ by a factor of 200 in their SERS intensities, even though they possess almost identical polarizabilities. A number of theories has been developed to explain this difference. Most widely used is the "charge-transfer" theory [41, 42], according to which chemisorption of the analyte on the metal structure leads to the formation of new electronic states, which can be resonantly excited and lead to a charge transfer between analyte and metal. For many metal-adsorbate combinations the Fermi level of the metal is located between the HOMO and the LUMO of the molecule. In these cases, charge transfer excitations can be induced by visible light. Once an electron has been transferred to the adsorbate, it can scatter inelastically with a phonon, and either gain or lose energy (Anti-Stokes or Stokes process). The scattered electron is transferred back
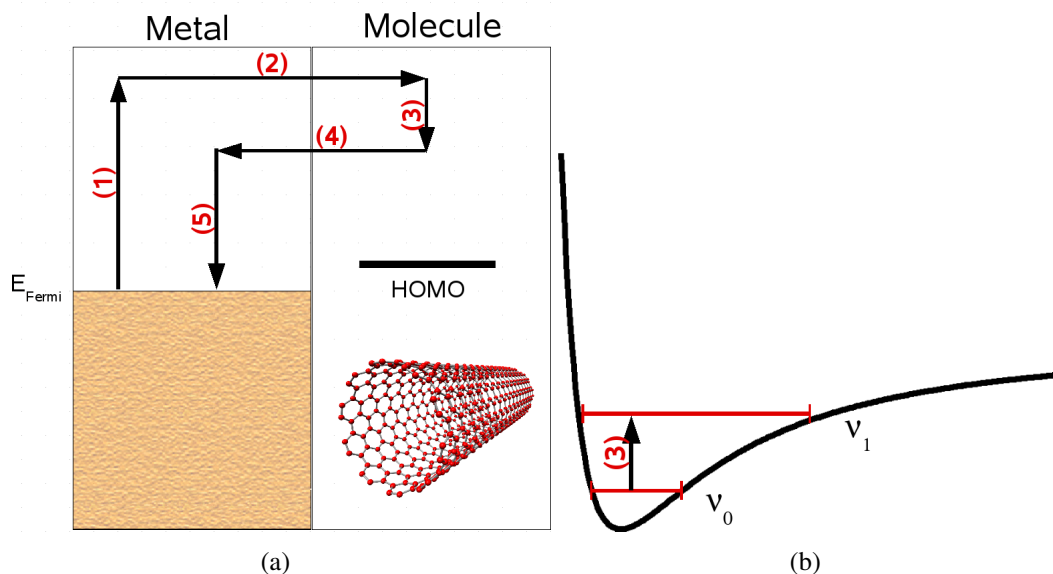
Figure 2.21: Schematic description of a Stokes process enhanced by the charge transfer mechanism (chemical SERS effect): (1) An electron in the metal is excited and (2) transferred to the molecule. There it (3) scatters inelastically with a phonon and (4) is transferred back to the metal where it (5) relaxes radiatively into the ground state.

to the metal, where it relaxes to its ground state by emitting a photon (Fig. 2.21).

SERS enhancement offers enhancement factors of up to 10^{14}, thus enabling the spectroscopy of single molecules [43, 44, 45, 46]. The first Raman spectra of individual carbon nanotubes were acquired by making use of the SERS effect. Currently, SERS is the only technique which can detect a single molecule *and simultaneously* identify its chemical structure. However, it has also been shown that SERS does not only enhance the Raman features of a molecule, but it can also significantly alter them, e.g. the polarization properties (i.e. the response to polarized excitation illumination)[47] and the intensity ratio of the G-band components [48]. These effects will be further addressed in the following chapters.

2.3.5 Raman modes of carbon nanotubes

Despite the great number of phonon modes (e.g. 66 for the (10,10) nanotube), conventional Raman spectra exhibit only a small number of peaks. This can be explained

by group theory, which imposes selection rules on the phonons. As a result, only a small number of phonon modes are Raman active. A typical Raman spectrum of a single-walled nanotube is depicted in Fig. 2.22 [26].

A noteworthy side-remark is the mutual exclusion of Raman and Infrared spectroscopy. From group theory it is straightforward to derive, that phonons, which are Raman-active, must be Infrared inactive and vice versa. This is, because a phonon is Raman active, if the corresponding phonon induces a change of polarizability of the involved bonds, whereas it is Infrared active if the phonon induces changes in the dipole moment.

2.3.5.1 The G-band

Whereas in graphite the G-band is a single Lorentzian peak at $1582 cm^{-1}$, in carbon nanotubes the G-band consists of several peaks which occur due to phonon wave vector confinement in circumferential direction. The G-band consists of two main peaks, the G^+ mode involving carbon vibrations along the nanotube axis at $1590 cm^{-1}$ and the G^- mode comprising nanotube vibrations along the circumferential direction at $1570 cm^{-1}$. For metallic nanotubes, the G^- mode is broadened and has a Breit-Wigner-Fano (BWF) line shape. Using polarization-dependent Raman spectroscopy it has been shown, that both G-band components are composed of three modes with A_1, E_1 and E_2 symmetries (see Fig. 2.23) [49]. When recording the G-band using SERS, interesting phenomena like line widths changes, scattering power exchange between G^- and G^+ and non-uniform enhancement characteristics have been reported [50].

2.3.5.2 The Radial Breathing Mode (RBM)

The RBM, occurring between $120 cm^{-1}$ and $300 cm^{-1}$, is the most characteristic of the carbon nanotube Raman bands, since it exists only in nanotubes and not in graphitic materials. As a totally symmetric mode, the RBM has A_1 symmetry. The RBM frequency can be used to determine the diameter of the nanotube and eventually chirally identify a nanotube. The relationship between diameter (d) and resonance frequency (ω) can be expressed as

$$\omega = c_1 + \frac{c_2}{d} \tag{2.3.7}$$

with the c_i being empirical fitting parameters ($c_1 = 234 cm^{-1}$ and $c_2 = 10$ [31]).
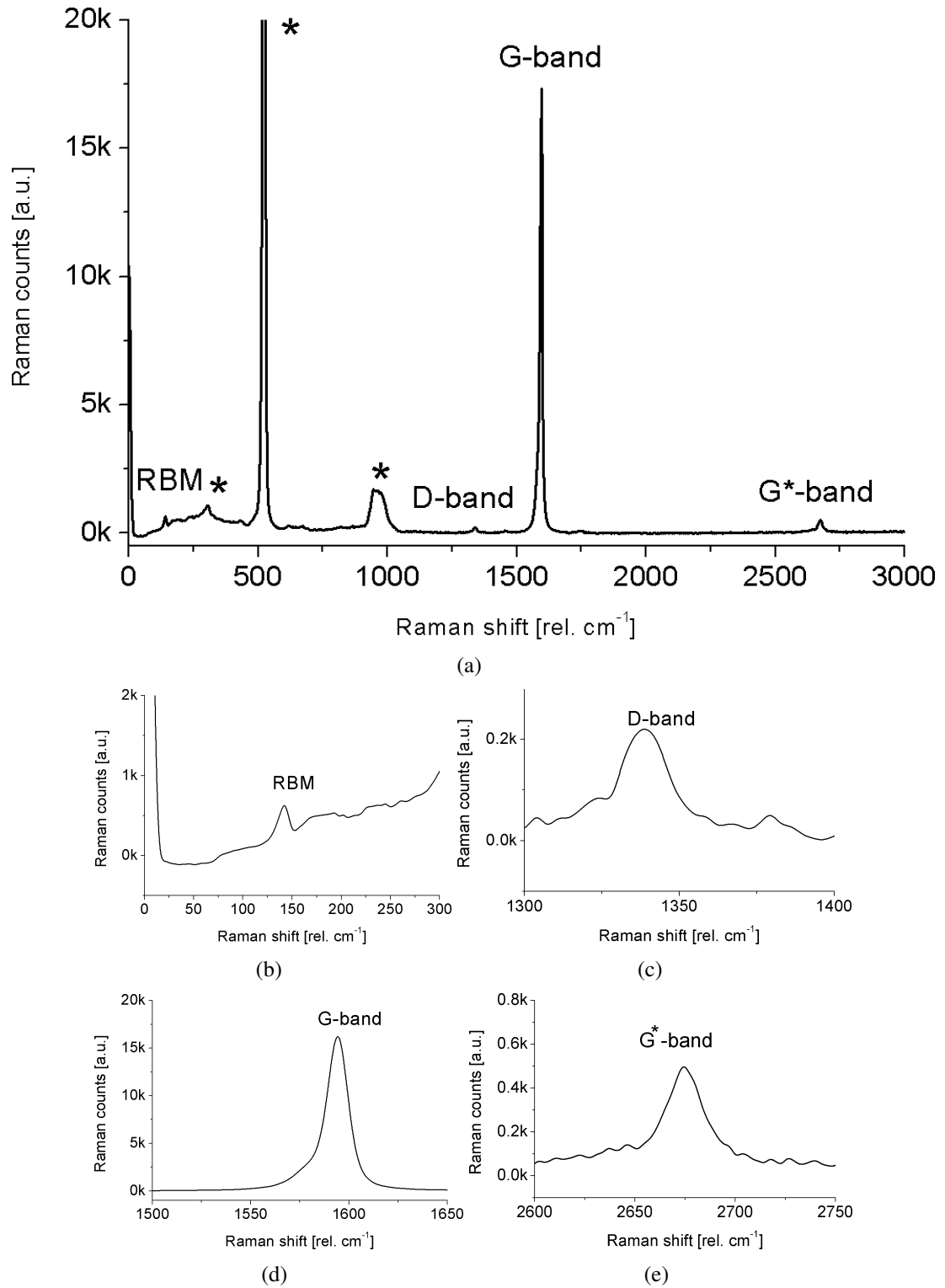
Figure 2.22: Typical resonant Raman spectrum of a carbon nanotube. (a) Overview spectrum. An asterisk marks the Raman modes of the SiO_2 background. (b)-(e) show zoom-in of the Raman features ((b): Radial Breathing Mode (c) D-band, (d) G-band (e) G^*-band).
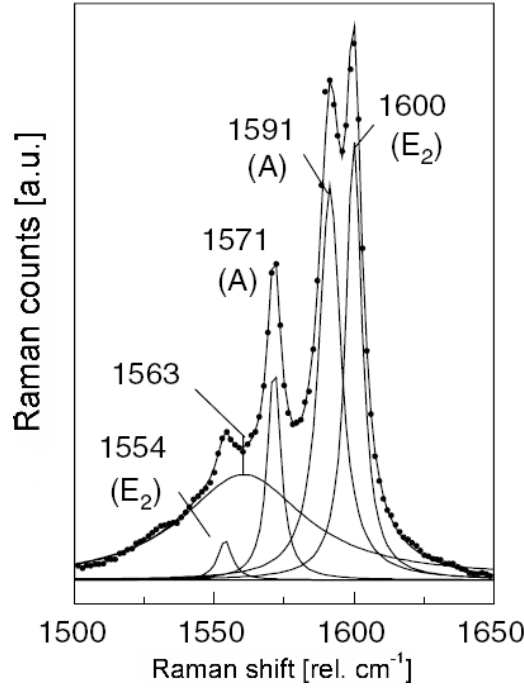
Figure 2.23: A high-resolution Raman spectrum showing the main components of the G-band [49].

With the aid of Kataura's plot it is possible to identify the chirality of a nanotube once its diameter has been determined (see section 2.3.2)[23].

2.3.5.3 D-band and G*-band

The D-band is located between $1240cm^{-1}$ and $1450cm^{-1}$ and its overtone, the G*-band, at the double frequency. Both bands are disorder-induced; their frequency depends on the excitation laser wavelength $\left(\frac{d\omega}{dE} = 53cm^{-1}\right)$. Since the G*-band is symmetry-allowed it is usually more intense than the symmetry-forbidden D-band, despite being an overtone vibration. Both vibrations are $q \neq 0$ modes and can therefore be used to probe the off-centre Brillouin zone.
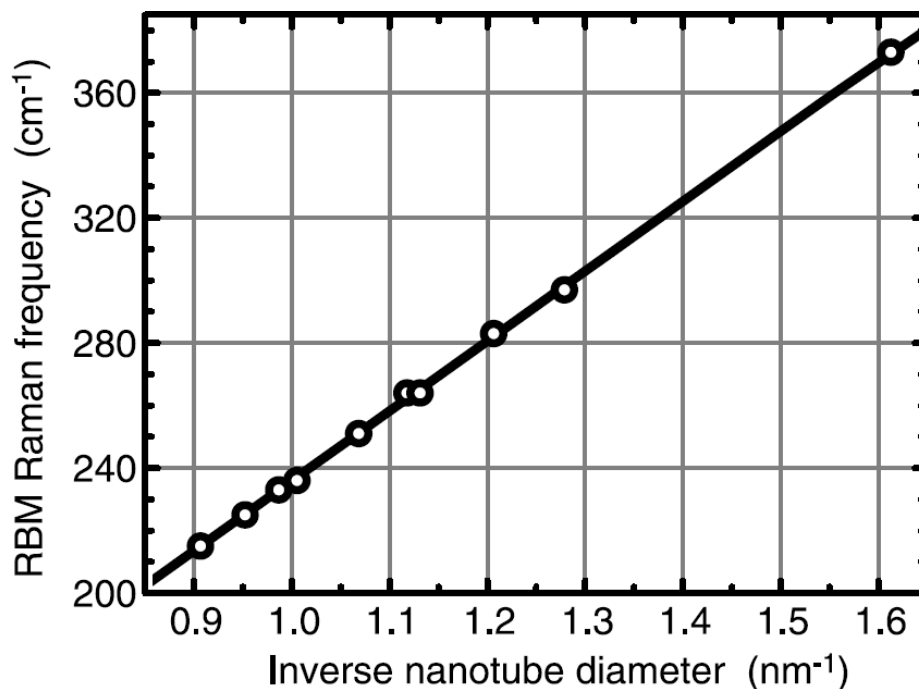
Figure 2.24: Measured RBM resonance frequency versus nanotube diameter, revealing the expected $1/d$ behaviour [51].

2.4 Chemical functionalization of carbon nanotubes

Carbon nanotubes possess unique properties already in their pristine form. Numerous attempts have been made to functionalize carbon nanotubes with different chemical species in order to tailor the carbon nanotube properties to individual needs. In the following sections, the plethora of modification approaches is summarized with special focus on functionalizations that target changes in the optical properties of the nanotubes. Furthermore, only sidewall functionalizations are considered.

2.4.1 Covalent schemes

The reactivity of the sp^2 bonds increases with the curvature of the structure. Therefore, the nanotube caps are the easiest part to modify, whereas the sidewall is more inert. Still, even the sidewalls are more reactive than the flat graphene sheet.

- **Sidewall halogenation** of carbon nanotubes has been reported for fluorine [52], chlorine and bromine [53]. Whereas for chlorine and bromine electrochemistry was used, fluorine could be attached by simply heating the nanotubes to 150-400°C under a fluorine atmosphere. Fluorinated nanotubes are soluble in ethanol, the fluorination destroys the sp^2 hybridization and renders both semiconducting and metallic nanotubes insulating.

- **Hydrogenation** of carbon nanotubes has been attributed both to physisorption and chemisorption mechanisms. However, recent experiments have shown a high uptake of hydrogen of up to 10 wt%, which cannot be explained by mere physisorption. The hydrogenation of carbon nanotubes can be achieved via a dissolved metal reduction method, or by exposing the nanotubes to an ion (i.e. proton) beam [54].

- A number of **cycloadditions** have been reported. For example dichlorocarbene was found to attach to carbon nanotubes via $[2 + 1]$ cycloaddition. Furthermore, the band structure of both metallic and semiconducting nanotubes was significantly modified [55].

- **Ozonolysis** of single-walled carbon nanotubes has been shown to occur between -78°C and room temperature, forming nanotube-ozonides. Ozonolysis was found to work best for small-diameter nanotubes, whereas the less reactive large-diameter nanotubes showed much less intense signs of functionalization [56].

- **Polymer grafting** is used with two different approaches: The *grafting to* method [57] attaches entire polymer structures to carbon nanotubes, whereas the *grafting from* method [58] starts by attaching a polymer precursor on the nanotube and subsequent polymerization. For example, organometallic compounds like butyl-lithium can be mixed with poly-(butadiene) and the hereby obtained polymeric anions can be grafted on the nanotube surface.

- **Electrochemical functionalization** has been performed on bulk samples as well as on individual nanotubes. Electrochemical modification has been demonstrated, for instance via reductive coupling of diazonium salts. The degree of functionalization could be adjusted between 0 and 5% [59]. The functionalization takes
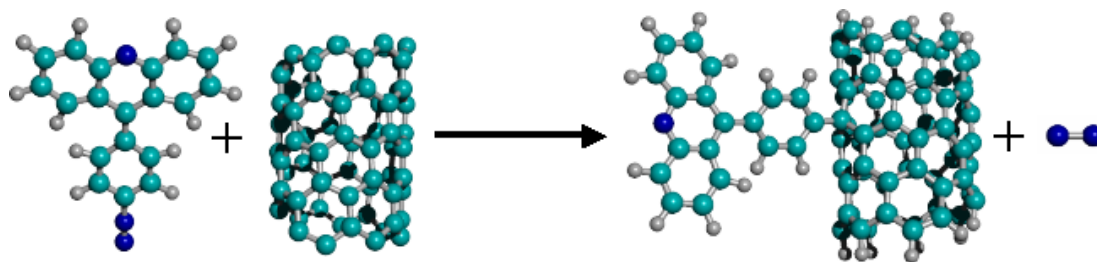
Figure 2.25: Reduction scheme. Color Coding: Carbon: cyan, Hydrogen: grey, Nitrogen: blue

place via an electron transfer from the nanotube, which creates a phenyl radical which is able to break the sp^2 bonds of the nanotube sidewalls and to create a covalent link (see Fig. 2.25).

The covalent attachment could be verified by the observation of an increased D-band in Raman spectroscopy. Since the reactivity of a nanotube decreases with increasing diameter, electrochemical functionalization was first observed for small diameter nanotubes (e.g. HiPco tubes)[60], but meanwhile also nanotubes with larger diameters have been functionalized.

Another aspect that needs to be taken into account is the imperfection of carbon nanotubes. It is widely accepted that in conventional nanotubes 1-3% of the constituting atoms belong to defect sites [61]. In most cases these defects are of the Stone-Wales type (pentagon-heptagon defects, see Fig. 2.26), atom vacancies or substitutional defects. Stone-Wales defects also occur during chirality changes within a nanotube. Due to their lower symmetry defect sites have a higher reactivity than the intact nanotube sidewall. Therefore, if the nanotube's functionalization degree does not exceed its defect density, the functionalization of the nanotube may be restricted to the defect sites.

2.4.2 Noncovalent schemes

In contrast to covalent modifications noncovalent modifications do not break the sp^2 bonds of nanotube sidewalls and therefore do not reduce the electric conductivity of the nanotube, nor do they appreciably change the Raman response. The interaction is based on $\pi - \pi$ stacking between nanotube and adsorbate. The noncovalently attached moieties may interact with the nanotube via a charge transfer process.
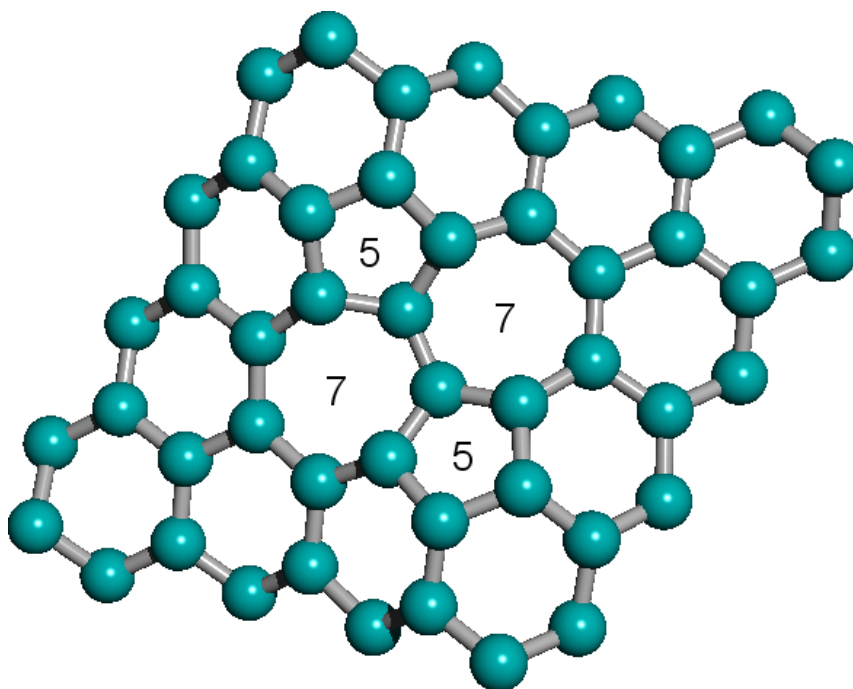
Figure 2.26: A Stone-Wales defect (pentagon-heptagon-pentagon) in a graphene sheet.

- Various **gas molecules** are known to adsorb on nanotubes with binding energies between 0.06eV (H_2) and 0.28eV (Xe) [62, 63]. Oxygen molecules are known to induce a strong p-doping in carbon nanotubes [64]. While the experimentally determined binding energies are in good agreement with theoretical predictions, the adsorption sites on the nanotube sidewalls is still under discussion for many gases. For example for oxygen, positions on top of the C-C bond or in the centre of each honeycomb are discussed.

- **Polymer composites** have been extensively studied. Here, the main goal is to use the nanotubes' exceptional mechanical properties to reinforce the polymer matrix. To this end a good contact between polymer and nanotube is crucial. This can be achieved by chemical functionalization of the nanotubes. The main polymers used in this context are epoxy [65] and acrylates like PMMA [66].

- **Charge transfer complexes** like tetrathiafulvalene (TTF) have been used to induce conductivity changes in contacted nanotubes [67]. This approach will be further elucidated in the next chapters.

2.5 Photoinduced electrical switching in carbon nanotubes

2.5.1 Optical properties of pristine carbon nanotubes

Owing to their one-dimensional structure, carbon nanotubes have unique photon absorption and emission properties. Light can be absorbed if the excitation wavelength coincides with the energy separation between two van Hove singularities and if the transition is allowed by symmetry rules. The absorption depends on the polarization of the excitation light. For simplicity reasons, only linear polarized light is considered here: If the polarization axis of the linear polarized light coincides with the nanotube's main axis, only $E_{\mu,\mu}$ transitions are dipole-allowed, whereas in the cross-polarized configuration, where the polarization axis lies perpendicular to the nanotube's main axis, only the $E_{\mu,\mu\pm1}$ transitions are dipole allowed. However, the $E_{\mu,\mu\pm1}$ are much weaker than the corresponding $E_{\mu,\mu}$ transitions.

Optical emission studies have been hampered by quenching effects, which can be overcome e.g. in a PMMA matrix. From these experiments it is apparent, that carbon nanotube are photoluminescent in the infrared regime (1000-1500nm) [68].

2.5.2 Noncovalent approaches

2.5.2.1 Spiropyranes

Spiropyranes are well-known photochromic molecules. They can switch between a neutral, colourless and a zwitterionic, coloured form (see Fig. 2.27). The formation of the coloured species is triggered by UV irradiation, whereas the reverse reaction can be stimulated by visible light. By linking them to a pyrene molecule, which can π-stack on the nanotube, they are noncovalently attached to the sidewalls of carbon nanotubes. For semiconducting nanotubes, a subsequent UV illumination lowers the nanotube's conductivity. The effect is reversible [69].
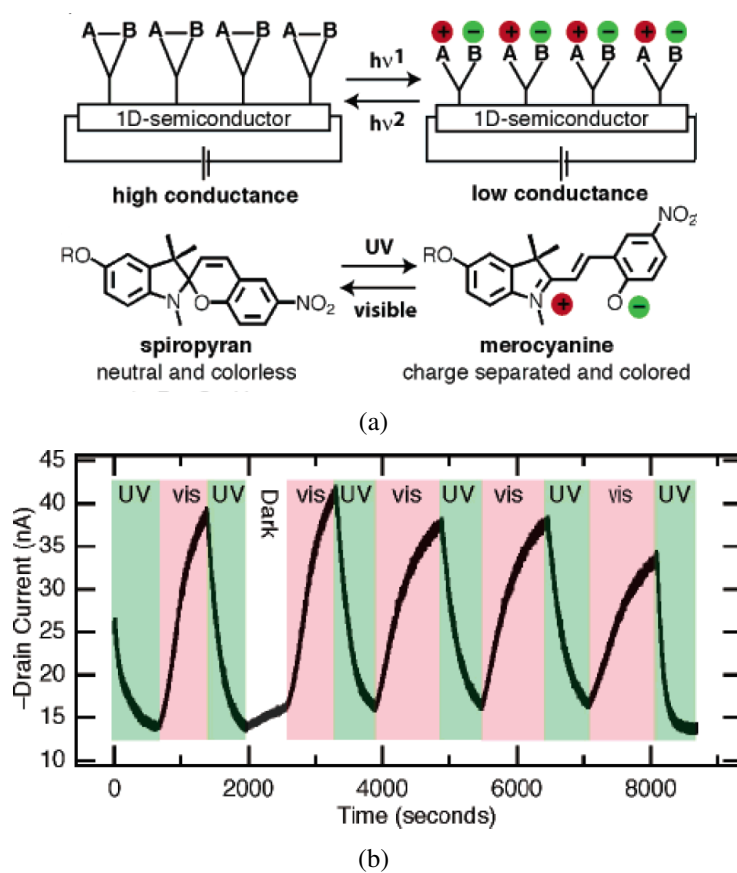
(a)

(b)

Figure 2.27: (a) The spiropyrane can undergo a conformational change induced by light. (b) The conformational change of the spiropyrane is used to switch between a high and a low conductance state of the nanotube [69].
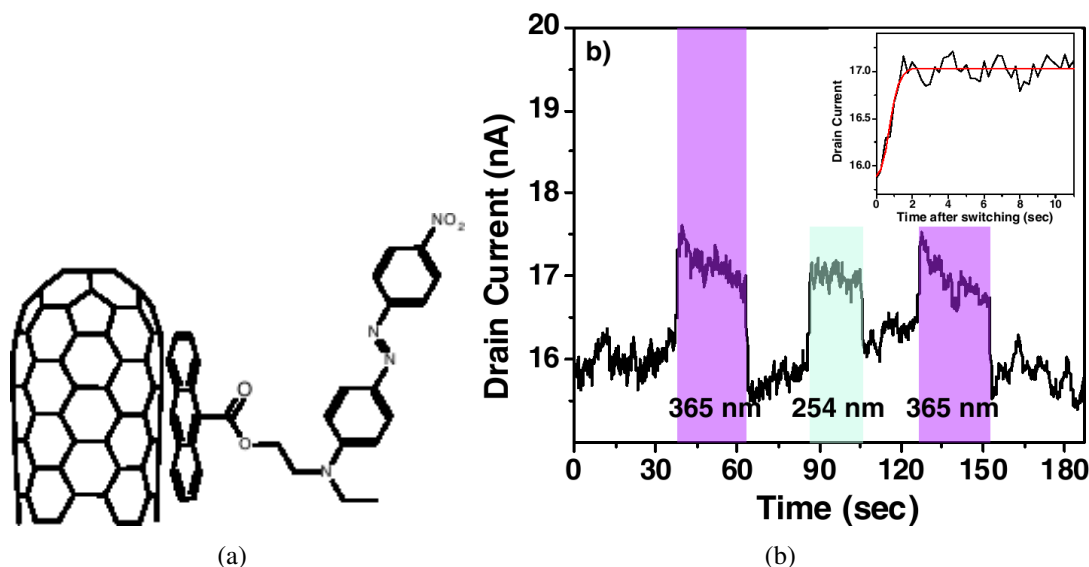
Figure 2.28: (a) The molecule is tethered to the nanotube via an anthracene group. (b) Light-induced changes in the drain current [70].

2.5.2.2 Azo dyes

Very recently, electrical conductivity switching in nanotubes based upon attached azo dyes has been reported [70]. An azo dye with an anthracene tether was used to induce a sizable conductivity switching upon illumination with UV light. Since similar experiments have been carried out in the course of this thesis (prior to [70]), a more detailed description of the experiments can be found in the next chapters (section 4.1.2 on 63).

2.5.3 Covalent approaches

2.5.3.1 Osmium tetroxide

Sidewall osmylation of carbon nanotubes occurs upon illuminating adsorbed osmium tetroxide molecules with UV light. This photo-induced cycloaddition results in a strong conductivity decrease. Upon photo-illumination the photoadduct is cleaved and the original conductivity of the nanotube is restored (see Fig. 2.29)[71].

(a)   (b)
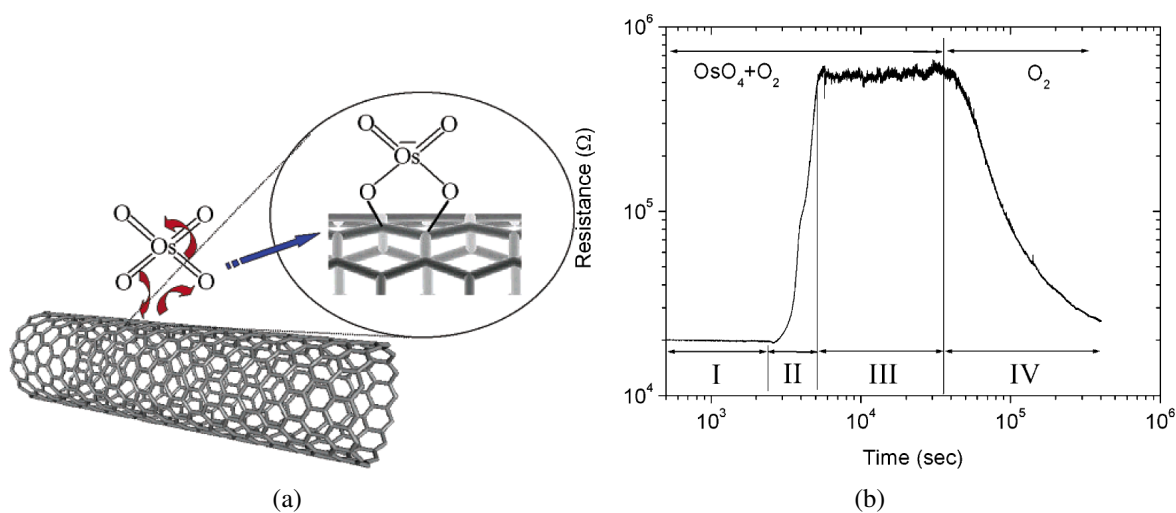
Figure 2.29: Fig.(a) illustrates how osmium tetroxide attaches to the nanotube sidewalls. Figure (b) exemplifies the details of the conductivity switching: Exposure to OsO_4 reduces the conductivity, if the sample is parallelly illuminated with UV light (regions I-III), whereas UV illumination under an oxygen atmosphere restores the original conductivity (region IV).

3 Experimental

3.1 Sample preparation

3.1.1 Deposition of HiPco nanotubes

Commercially available HiPco nanotubes are fabricated in a **hi**gh **p**ressure **co**nversion process, which is a gas phase chemical vapour deposition (CVD) process using CO as carbon feedstock and Fe(CO)$_5$ as catalyst precursor at a temperature of $600°C$ and a pressure between 1 and 10 bar. While the nanotubes produced with this process have very small diameters down to 0.7nm, they usually appear as bundled nanotubes, which need to be separated in order to characterize individual nanotubes in further investigations.

For a microscopic analysis as well as for electrical transport measurements the nanotubes have to be placed on a flat and insulating Si/SiO$_2$ surface. However, in order to debundle and purify the as-delivered nanotubes, they first have to be suspended in an aqueous solution. An efficient surfactant to suspend carbon nanotubes in an aqueous environment is sodium-dodecyl sulfate (SDS, see Fig. 3.1). The amphiphilic SDS forms a micellar structure around the nanotube, which allows for an efficient nanotube suspension. An efficient disintegration of the nanotube bundles can be achieved by inserting a tip sonicator into the nanotube/SDS suspension. However, the nanotubes also break during the sonication process and therefore, only a few tip sonication pulses are applied if the nanotubes are to be contacted by e-beam lithography (minimum length: $\approx 1\mu m$). Combining the harsh tip sonication process with a mild bath sonication leads to a high percentage of thin bundles or individual tubes in the suspension. After this treatment, the small bundles and individual nanotubes have to be separated from the remaining
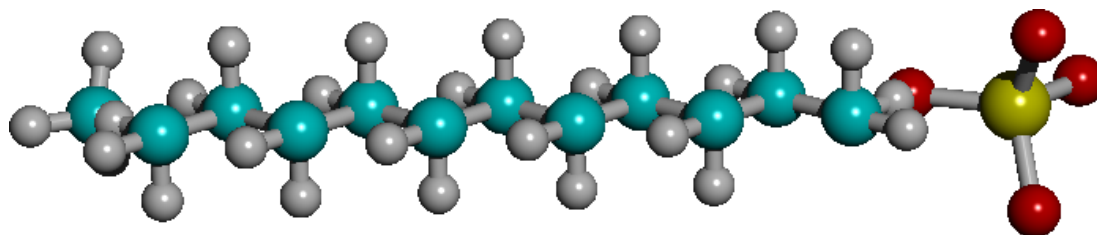
Figure 3.1: Chemical structure of SDS. Using SDS nanotubes can be suspended in aqueous solution. SDS comprises a hydrophilic head and a hydrophobic tail. Colour coding: Carbon: cyan, Oxygen: red, Hydrogen: grey, Sulfur: yellow

large bundles and other carbonaceous material. This can be achieved by centrifugation, where carbonaceous material and big nanotube bundles are sedimented out at the bottom of the centrifugation tube. After a centrifugation of 1 hour at 14000rpm ($\approx 3800g$) the supernatant contains mostly individual nanotubes and small bundles.

In order to immobilize the nanotubes on a SiO_2 surface, the surface is treated with 3- (aminopropyl)triethoxysilane to increase the adhesion forces between nanotube and SiO_2 surface. The silane-coated Si/SiO_2 wafer piece is then immersed in the nanotube suspension and the nanotubes are deposited randomly on the surface. The entire deposition process depends critically on the applied parameters and has to be optimized for each desired tube length and density. Fig. 3.2 shows an AFM image of deposited HiPco nanotubes.

3.1.2 CVD growth from Fe catalyst particles

Even after careful optimization, the HiPco deposition process yields a high percentage of small nanotube bundles, as it can be shown by AFM and Raman spectroscopy. In order to obtain better quality samples a CVD growth system has been set up and optimized together with our cooperation partners (Alf Mews, Nan Fu) at Siegen University. For this approach, nanoscale metallic nanoparticles are deposited onto the SiO_2 substrate. However, the particles are not deposited directly, but instead a precursor material, namely $FeCl_3$ particles are spin-coated onto the substrate. Upon heating at 700°C under ambient conditions organic contaminants (mainly residues from the organic solvents)
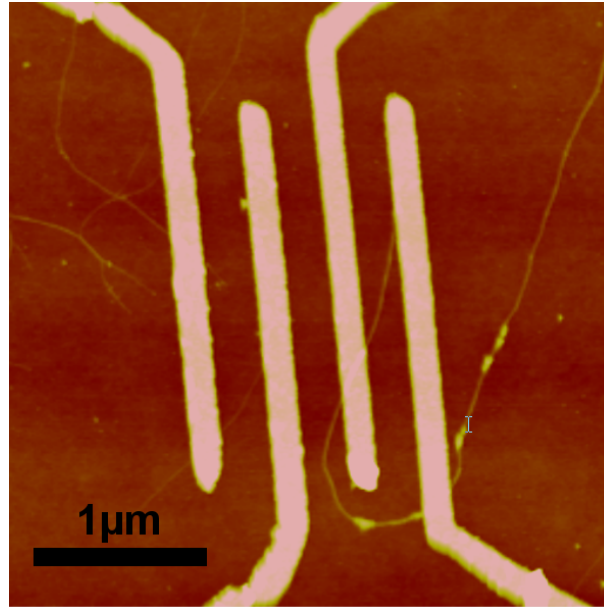
Figure 3.2: AFM image of HiPco nanotubes contacted by Au/Pd electrodes. The non-uniform diameter of the nanotube is due to SDS residues around the nanotube.
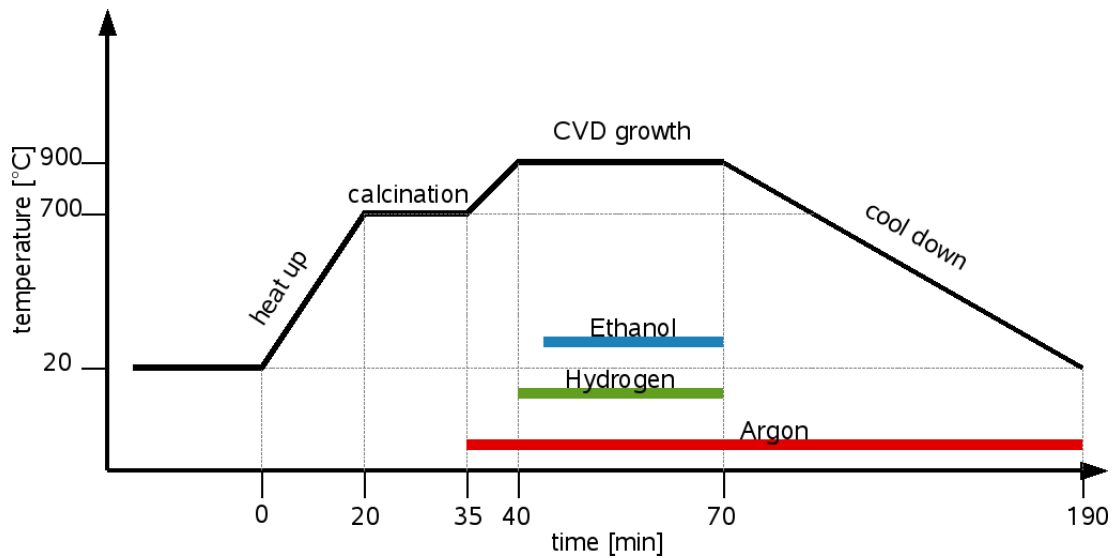

Figure 3.3: This sketch comprises the main parameters of the CVD growth process as a timeline.
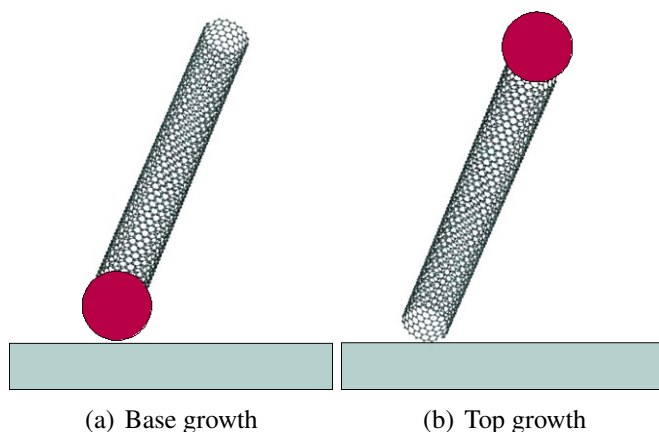
(a) Base growth   (b) Top growth

Figure 3.4: Illustration of possible CVD growth modes: (a) bottom growth and (b) top growth

decompose and leave clean Fe_2O_3 particles (calcination). The sample is then heated to $900°C$ under argon atmosphere. Keeping the temperature constant, ethanol vapour as carbon feedstock and hydrogen are inserted into the system, leading to the growth of individual single-walled carbon nanotubes with a narrow size distribution (Fig.3.3). The supply of elemental carbon for the growth process can be controlled by adjusting the hydrogen concentration. The iron nanoparticles serve as a catalyst for the nanotube formation. The details of the nanotube growth at the metallic nanoparticles are still a subject of active research. Possible growth mechanisms include base growth, where the catalyst particle remains fixed on the samples and top growth, where the catalyst particle is lifted up by the growing nanotube (see Fig. 3.4). After 30 minutes, the sample is cooled under argon atmosphere. Through optimization of the process it became possible to routinely grow nanotubes in a controlled density on the SiO_2 surface.

An example for an individual CVD-grown nanotube with a length of over $100\mu m$ length is depicted in Fig. 3.5. The picture was taken by using the Raman imaging mode at its RBM frequency $\left(247cm^{-1}\right)$. It is noteworthy, that the nanotube in Fig. 3.5 shows the same RBM over the complete nanotube length, ruling out defect-associated chirality changes which would result in a modified RBM frequency. Additionally, since the Raman spectra recorded along the nanotube do not show a significant D-band signal, a low defect density throughout the nanotube can be inferred.
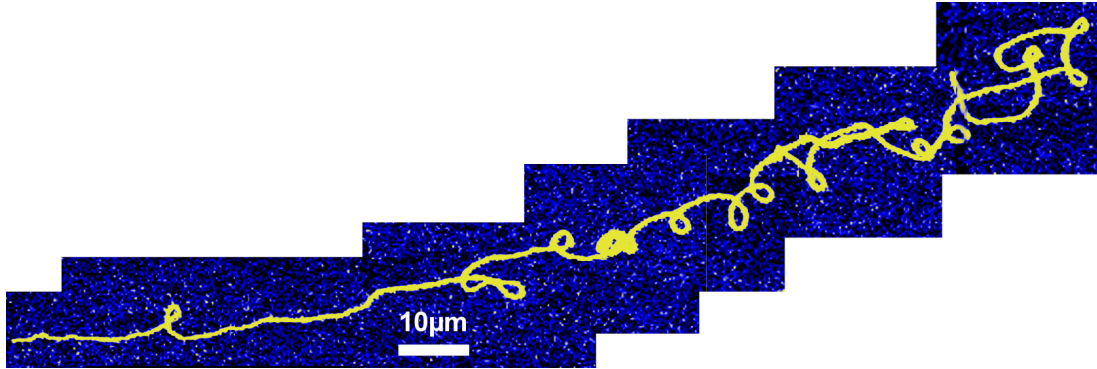
Figure 3.5: With the optimized CVD setup nanotubes of over $100\mu m$ length could be obtained.

3.2 Electrical transport measurements

After the HiPco deposition or CVD process, the nanotubes lie flat on the SiO_2 surface. The oxide has a thickness of 100-200nm and is a very good insulator, allowing for a detection of currents in the pA range through the nanotube. Measuring electrical currents in carbon nanotubes is interesting for a number of reasons:

- It can be checked very easily, if a nanotube is semiconducting or metallic (see Fig. 3.9). Whereas metallic nanotubes are promising candidates for **interconnects** in electronic circuits, semiconducting nanotubes can be used as nanoscale **transistors**.

- Nanotubes are close-to-ideal **sensor components**, since all constituting atoms are located at its surface. They are sensitive to the presence of chemical species like liquids and gases as well as to electromagnetic fields (e.g. light). The sensitivity of nanotubes can be improved via chemical functionalization for improved light sensitivity or noble metal nanoparticle deposition for improved gas sensitivity.

- A covalent modification of a carbon nanotubes significantly lowers the electrical conductivity, since the electrons are scattered from the newly introduced defects in the nanotube sidewalls. Thus, by measuring changes in conductivity it is possible to **estimate the degree of functionalization** of a nanotube.

Electric contact to the nanotubes on the Si/SiO_2 surface is achieved via e-beam lithography. For this purpose the nanotubes are covered with a thin layer (100nm) of
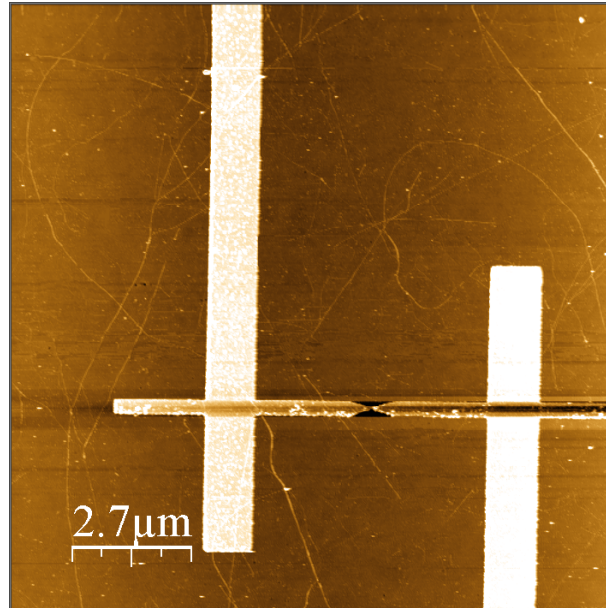
Figure 3.6: AFM image of contacted, CVD-grown nanotubes.

electron beam resist (PMMA, polymethylmethacrylate). Then, the resist is exposed to an electron beam in the areas, where the electrodes are to be located. Afterwards, the Au/Pd electrodes (60/40) are deposited on the sample. Finally, the remaining PMMA is removed with a lift-off procedure involving immersion in N-Methyl-2-Pyrrolidone (NMP) and isopropanol. Depending on the desired application very different shapes of the electrodes can be appropriate. Commonly used is the 4-finger structure (Fig. 3.2), which allows for four-probe measurements. For other measurements, the gap-electrode structure (Fig. 3.7) is better suited.

Figure 3.7: A gap structure suitable for samples comprising a low density of nanotubes. The wide electrode structure increases the chance of having a nanotube within the two electrodes.

Contact between the Au/Pd electrodes and the measurement devices can be achieved in two ways: Either, the sample is glued into a chip carrier, where connectio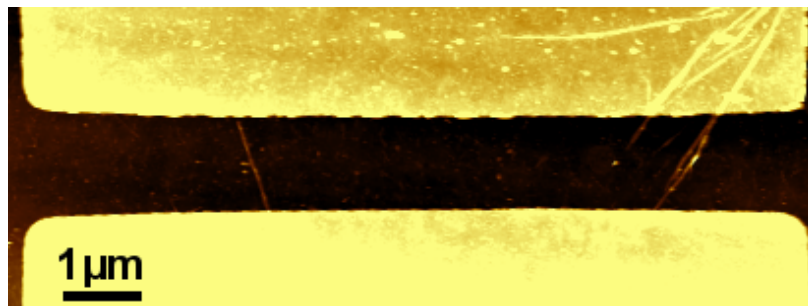ns between the chip carrier contacts and the gold electrodes are made with a bonding device using thin gold wires. While this technique is required for some studies and results in the most reliable contacts, it is also a time-consuming method and furthermore not easily applicable in the case of electrochemical modifications. Thus, a second contacting procedure is also frequently used: It involves one or several tungsten tips, which are attached to micromanipulators (Süss MicroTec PT100), enabling direct contacting of the bond pads.

The measurement setup for the contacted nanotube consists of two Keithley 2400 voltage sources, two Keithley 2000 voltmeters, a current-to-voltage converter (I/V converter) and a measurement software, which controls the devices mentioned above and records the acquired data. All measurement components are wired with coaxial cables in order to minimize the influence of noise. One Keithley 2400 supplies the voltage between the nanotube contacts (source and drain), the other Keithley 2400 supplies the voltage for the gating electrode, while also monitoring the gate leakage currents though the oxide layer ($I_{Gate} < 1nA$; $V_{Gate,max} = 40V$). In order to determine the voltage drop of connecting cables, one Keithley 2000 measures the source-drain voltage that the first Keithley 2400 applies. The source-drain current is fed into an I/V converter, the amplified output voltage of the I/V converter is recorded by the second Keithley 2000 voltmeter (an overview of the setup is shown in Fig.3.8).

The conductance of a nanotube is extracted from a linear fit of the current through the nanotube (drain current) versus the applied voltage (drain-source voltage). This plot is often referred to as *IV curve*. By measuring IV curves at different gate voltages, semiconducting nanotubes can be distinguished from metallic nanotubes. For semiconducting tubes, the band gap renders the nanotubes insulating, until the applied gate voltage shifts the nanotube's conduction band to the conduction band level of the metal contacts. Since nanotubes are p-type semiconductors with holes as major charge carriers when investigated under ambient conditions, the high conductance state (*"On-state"*) is reached for a negative bias and the low conductance state (*"Off-state"*) for a positive bias. The ratio between the high and low conductance states can be as high as 10^6. For metallic nanotubes, the conductivity remains almost unchanged upon sweeping the gate voltage. An example measurement is depicted in Fig. 3.9.
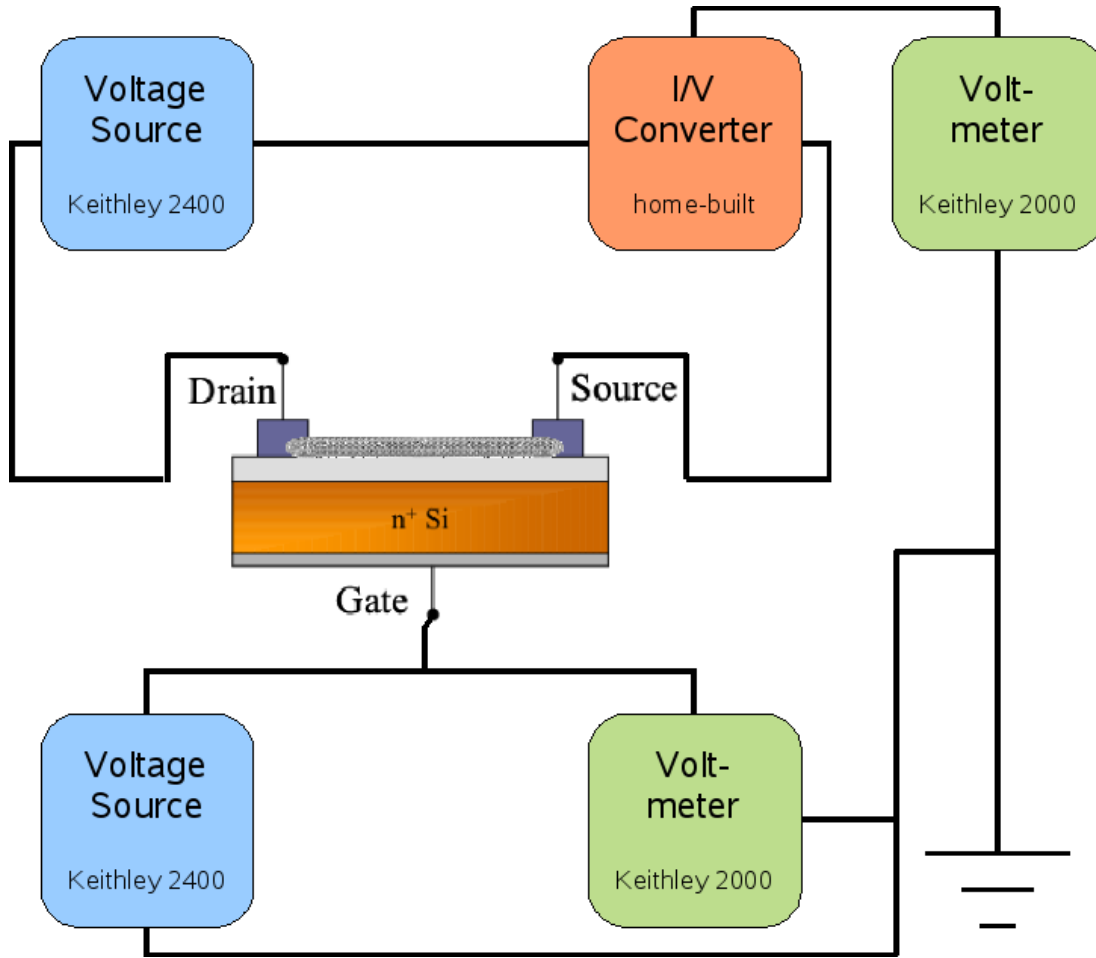
Figure 3.8: Transport measurement setup. All measurement devices are controlled via a computer software.

The conductance of a semiconducting nanotube (Fig. 3.9) displays a hysteretic behaviour. This behaviour is most likely induced by a thin layer of water molecules, which act as charge traps. Under ambient conditions, a water film is inevitable due to the atmospheric moisture. However, the water layer can be removed by performing measurements under UHV conditions. In fact, only a negligible hysteresis due to interactions with the SiO_2 substrate is observed under such conditions.

Figure 3.9: Comparison of the conductance between a semiconducting (black curve) and a metallic (red curve) nanotube: While the semiconducting tube shows a very pronounced gate dependence, the metallic tube's conductance remains almost constant over the whole gate range. The arrows denote the way the gate voltage has been changed.

3.3 Atomic Force Microscopy

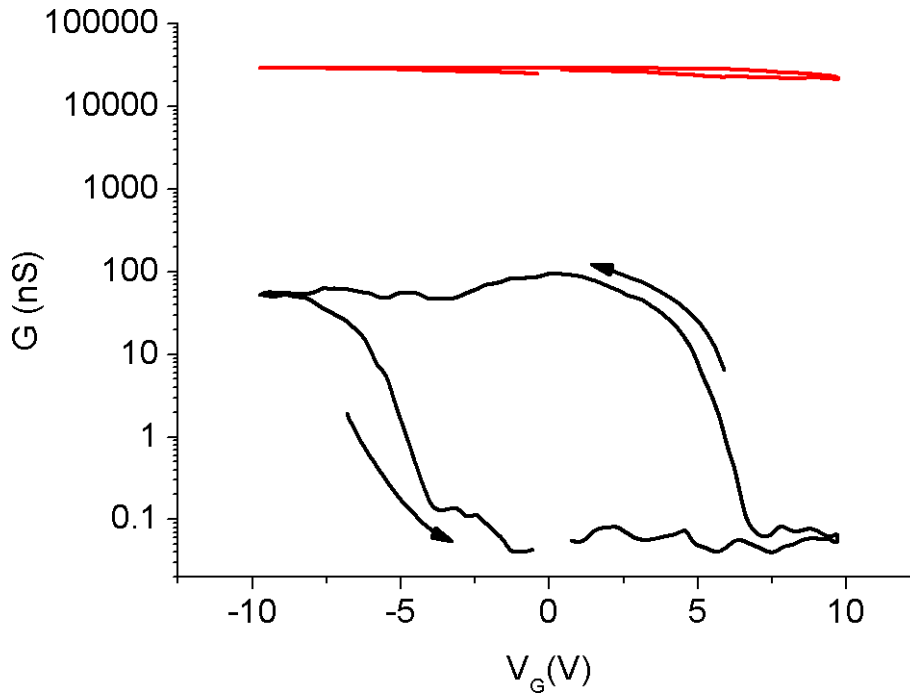A commercially available atomic force microscope (AFM, Digital Instruments Nano-scope III) has been used to investigate carbon nanotubes on the SiO_2 surface. The AFM, invented by Binnig and Rohrer (Nobel Prize in Physics in 1986 for the development of the STM) [72] utilizes a sharp probe tip to raster scan a surface. The probe tip is located at the end of a cantilever, which bends in response to the force between tip and sample. The bending can be detected by measuring the deflection of a laser beam, which is focused on the AFM cantilever. A standard force-distance curve is depicted in Fig. 3.11. AFM images can be acquired by keeping the AFM tip at a constant distance from the surface (*height mode*) or by using a feedback loop to keep the tip-surface force constant. While the first mode can be suitable for atomically flat surfaces, a feedback control proved to give the most reliable results for nanotubes on a SiO_2 surface. For the acquisition of AFM images with feedback control three scanning modes have to be
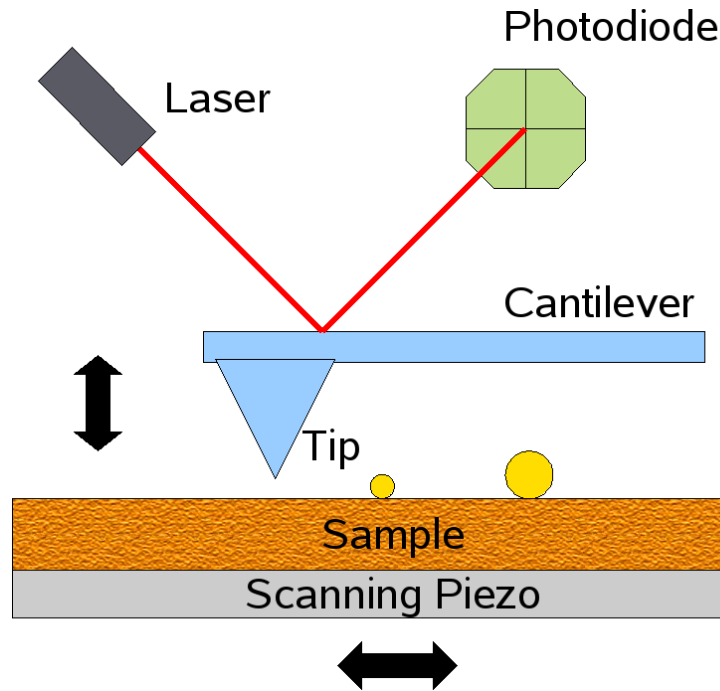
Figure 3.10: Working principle of an AFM: The scanning piezo moves the sample in x and y direction, while the tip moves in the z direction.

distinguished:

- In **contact mode** tip and surface remain in a close contact during the full acquisition time. The tip detects a repulsive force from the surface (Fig. 3.10, red region).

- By oscillating the tip at its resonance frequency (usually in the kHz regime) in such a way that it touches ("taps") the surface only for the maximum oscillation amplitude, the so-called **tapping mode** or intermittent contact mode is realized. Compared to the contact mode, tapping mode is often advantageous, since it minimizes the lateral forces between tip and surface and thereby allows to scan soft surfaces and poorly immobilized samples.

- For a true **non-contact mode** the tip must be operated in the attractive regime of the force-distance plot (Fig. 3.10, green region). Under ambient conditions this mode is very difficult to realize due to the thin water layer on top of all samples, which causes a "jump to contact" in many cases.
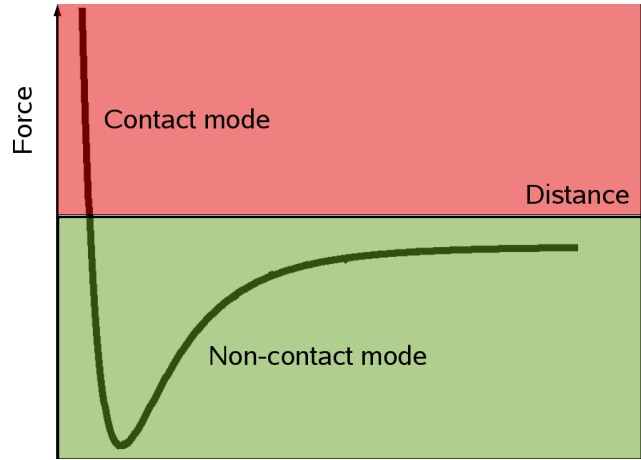
Figure 3.11: The force distance relation between tip and surface can be described by a Yukawa potential $(V(r) \propto c_1/d^{12} - c_2/d^6)$.

Using the Nanoscope III instrument in tapping mode, nanotube diameter and length could be determined routinely. For single HiPco nanotubes an average diameter of $\varnothing \approx 1nm$ was estimated, while for HiPco bundles diameters in the range of $\varnothing \approx 2-3nm$ were often found, corresponding to small ensembles of < 5 nanotubes. The HiPco nanotubes were rather uniform in length with an average length of $2\mu m$. For the CVD-grown nanotubes, the average diameter was significantly larger ($\approx 1.3nm$), while the nanotube length was strongly dependent on the growth conditions, ranging from 100nm to over 200μm. Over 90% of the investigated CVD-grown tubes were single-walled nanotubes. Bundling of CVD nanotubes was observed only in very few cases.

3.4 Confocal Laser Microscopy

In a conventional optical microscope the image is defined as a superposition of the in-focus region and the out-of-focus region of a specimen. In 1957, Marvin Minsky patented the idea of the confocal laser scanning microscope. With this type of microscopy, the out-of-focus image is suppressed, resulting in an image containing information only from the focal area. The principle setup of a confocal microscope is depicted in Fig. 3.12. A parallel laser beam is focused through a pinhole to a diffraction-limited spot; away from the focal plane the laser intensity falls off rapidly. The reflected signal is collected by the same objective and directed to a detector via a second pinhole
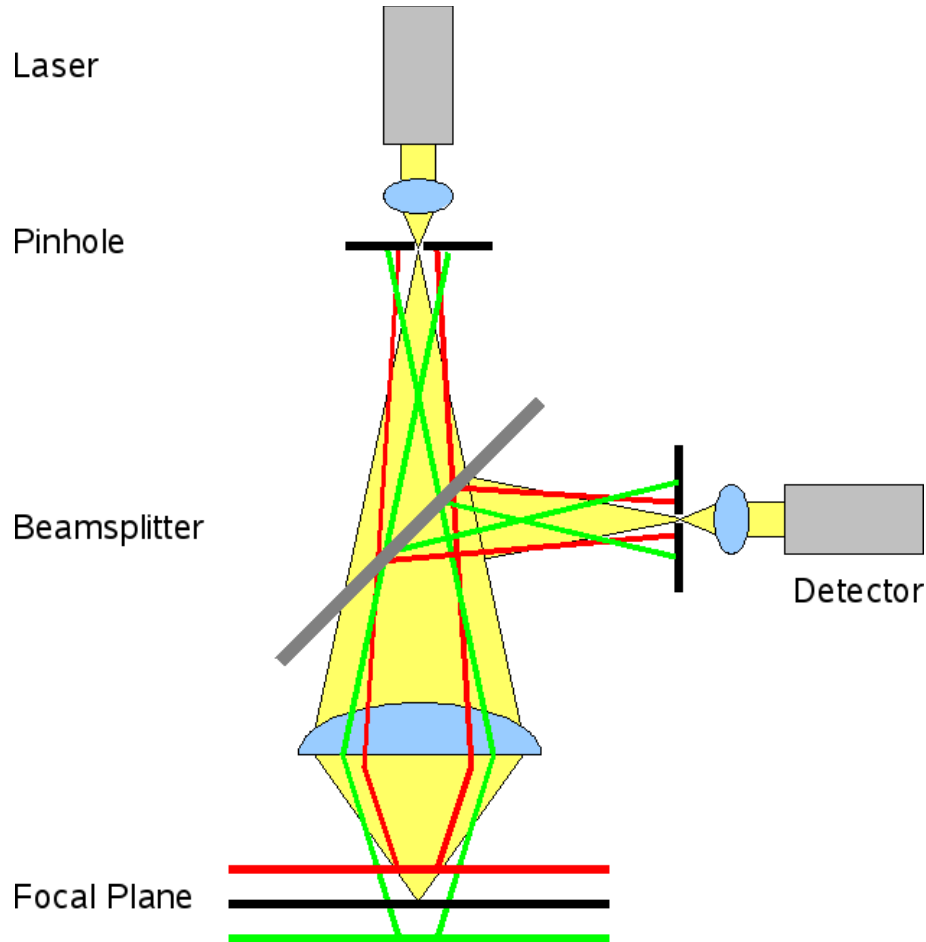
Figure 3.12: Principle of a confocal microscope. The reflected light from out-of-plane objects is blocked by the pinholes.

in the conjugated focal plane of the specimen. The second pinhole blocks all light that is not coming from the focal plane.

Thus, light not coming from the focal plane is two-fold suppressed, allowing for an increased contrast in the image. The downside of a confocal laser scanning microscope is, that only one spot at a time can be acquired; either the laser (via scanning mirrors) or the sample (via a scanning piezo) have to be scanned in order to obtain a complete image of the specimen. To avoid polarization-dependent effects, circularly polarized light is often used for standard measurements.

3.5 Confocal Raman Spectroscopy

A confocal laser scanning microscope can easily be extended into a confocal Raman microscope by filtering the original wavelength in the detection setup with an appropriate filter (e.g. SuperNotch Plus) and sending the filtered laser light to a spectrograph. The spectrograph transforms the incoming signal $\vec{E}(t)$ into a frequency domain spectrum $E'(\omega)$. The frequency domain spectrum essentially is a histogram of the energy of the detected photons.

3.5.1 Raman imaging

By plotting the number of photons at a distinct energy E_1 as a function of the acquisition area on the sample, one obtains an emission map of the sample. By adjusting E_1 to the energy of a nanotube Raman mode (e.g. the G-band), one can detect the location and spatial extension of nanotubes that are in resonance with the excitation laser wavelength (see Fig. 3.14).

3.5.2 Polarized Confocal Raman Spectroscopy

Using polarized Raman spectroscopy it is possible to determine the symmetry of the underlying phonon mode in the nanotube. Fig 3.15 depicts the principle of the setup. It deviates from the standard confocal Raman setup by the introduction of two polarizers, one in the excitation path and one in the detection path. In the (V-) experiments, only the polarizer in the excitation path is used. The polarizer serves to create linearly polarized light whose polarization direction can be varied between $0°$ and $180°$. (VV) experiments are performed with the second polarizer in the detection path, which has a polarization axis parallel to the excitation polarizer, while (VV) are spectra recorded by simultaneously rotating both polarizers. In the (VH) experiments, the two polarizers are simultaneously rotated while keeping a relative angle of $90°$ between them. In all cases, the polarization angle α is defined as the angle between the first polarizer's polarization axis and the nanotube.

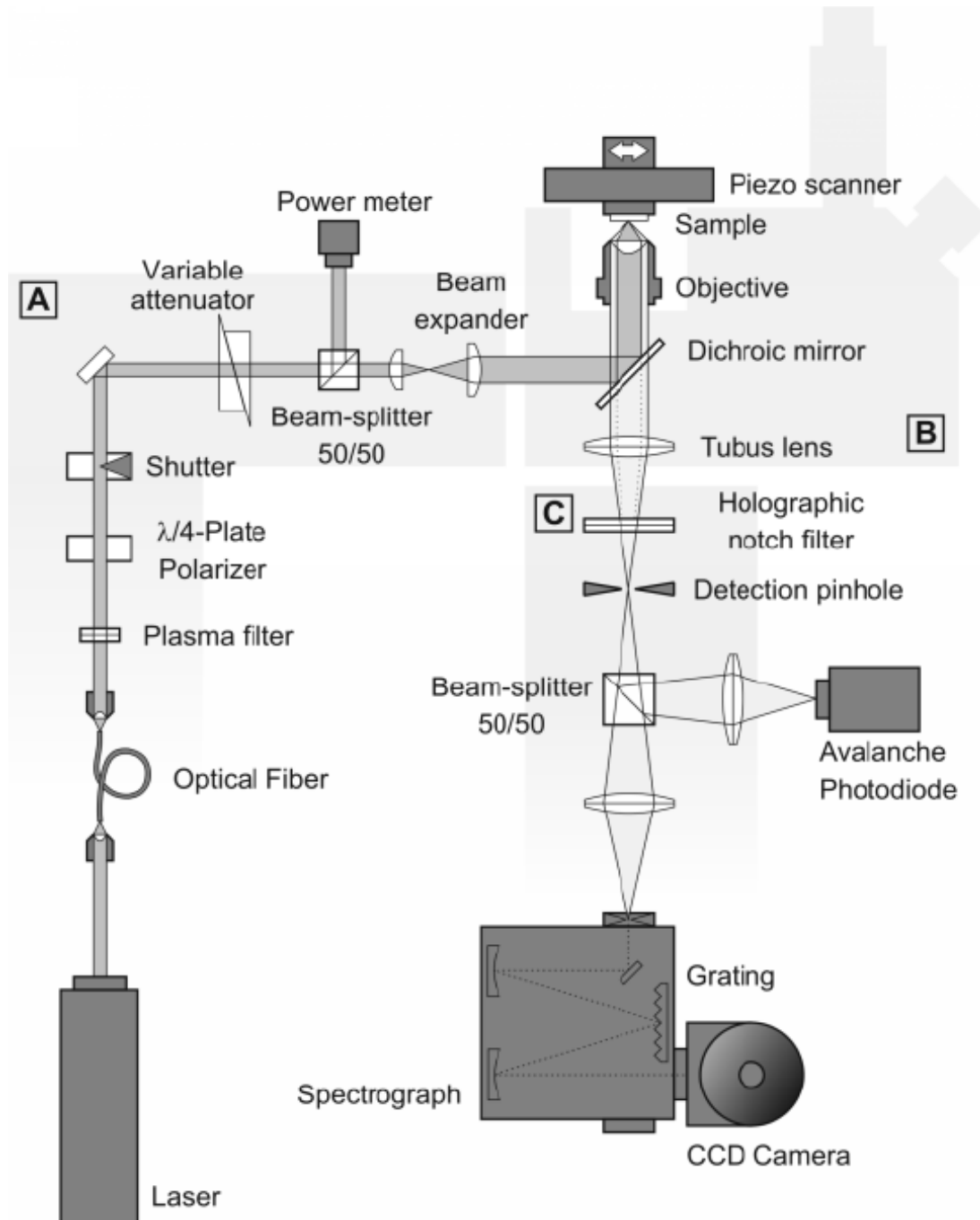Figure 3.13: Block diagram of a confocal laser scanning microscope with attached spectrograph ([73])
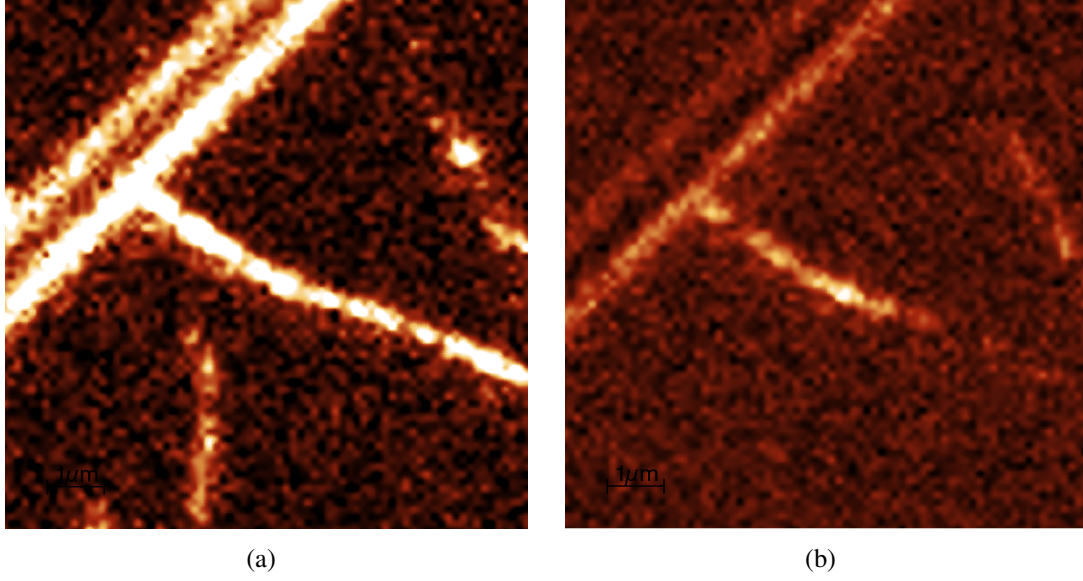
(a)   (b)

Figure 3.14: (a) A G-band Raman image ($\lambda_{\mathrm{exc}} = 568nm$) of carbon nanotubes close
          an Au/Pd electrode. (b) A Raman image of the same area recorded at
          the RBM frequency of the nanotube in the image centre gives additional
          insight in the nanotube's structure: The nanotube in the bottom left of the
          Raman G-band image is not visible in this Raman RBM image and can
          therefore be assigned to a different diameter. Additionally, the nanotube in
          the centre of the image is only partially visible in the Raman RBM image,
          which might be explained by a spontaneous chirality change.

With this setup, a polarization analysis of the Raman signal from the nanotubes can be
performed. The symmetry of the different phonon modes is represented by their Raman
tensor $\overleftrightarrow{R}$:

$$\overleftrightarrow{R}_{A_1} = \begin{pmatrix} 0 & 0 & 0 \\ 0 & 0 & 0 \\ 0 & 0 & c \end{pmatrix} \quad \overleftrightarrow{R}_{E_1} = \begin{pmatrix} 0 & 0 & e \\ 0 & 0 & 0 \\ e & 0 & 0 \end{pmatrix} \quad \overleftrightarrow{R}_{E_2} = \begin{pmatrix} e & 0 & 0 \\ 0 & -e & 0 \\ 0 & 0 & 0 \end{pmatrix} \qquad (3.5.1)$$
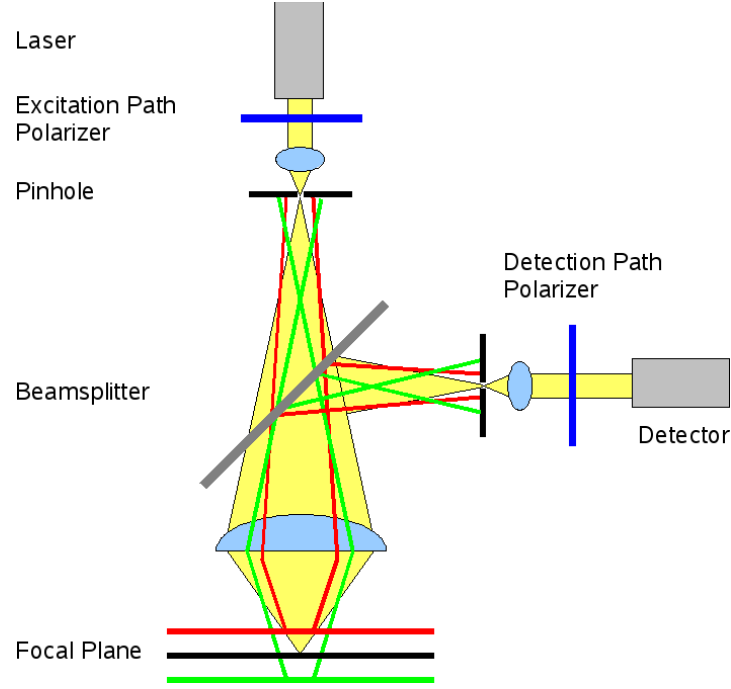
Figure 3.15: The introduction of two polarizers allows for an acquisition of polarized Raman spectra.

For circularly polarized light propagating in z-direction and the nanotube's main axis pointing in x-direction the polarizers can be represented as

$$\vec{V} = \begin{pmatrix} \sin(\psi) \\ 0 \\ \cos(\psi) \end{pmatrix} \qquad \text{and} \qquad \vec{H} = \begin{pmatrix} \sin(\psi + 90°) \\ 0 \\ \cos(\psi + 90°) \end{pmatrix}. \qquad (3.5.2)$$

The angular dependence $I(\psi)$ of the VV/VH experiments is then given by

$$I(\psi) \propto \begin{cases} |\vec{V} \overleftrightarrow{R} \vec{V}|^2 & \text{for VV experiments} \\ |\vec{H} \overleftrightarrow{R} \vec{V}|^2 & \text{for VH experiments} \end{cases} \qquad (3.5.3)$$

Polar plots showing the calculated angular dependence of different phonon modes are shown in Fig. 3.16. By comparing these curves with experimentally determined angular dependencies for different Raman bands, the symmetry of the underlying phonon modes can be determined.

(a)

(b)

(c)
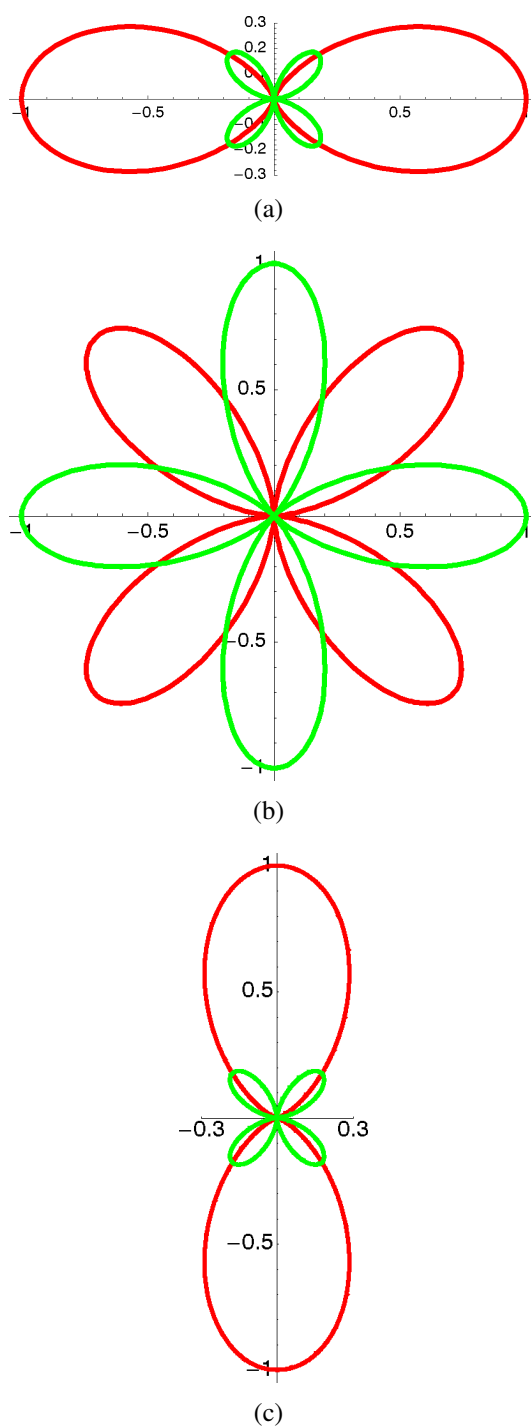
Figure 3.16: Polar plot of the calculated angular intensity dependence (VV-red, VH-green) for (a) A_1 symmetry, (b) E_1 symmetry, and (c) E_2 symmetry.

3.6 Electrochemical modification of individual nanotubes

In order to transfer the principle of bulk electrochemistry to the single nanotube level, a home-built electrochemical cell made of Teflon (Fig. 3.17) has been used. It can be filled with up to 500μl of solution and comprises a platinum counter electrode and a platinum pseudoreference electrode.

A micromanipulator with a tungsten tip (Süss PT 100) is used to contact the Au/Pd electrodes on the sample. Therefore, a contacted nanotube can be used as a working electrode in the cell. All electrodes are connected to a Potentiostat (*Solartron 1285*), which is controlled via a computer interface. After the electrochemical process the sample is removed from the electrochemical cell, rinsed with the solvent and blown dry.

Figure 3.17: An electrochemical cell made of Teflon

4 Dye functionalization of Carbon Nanotubes
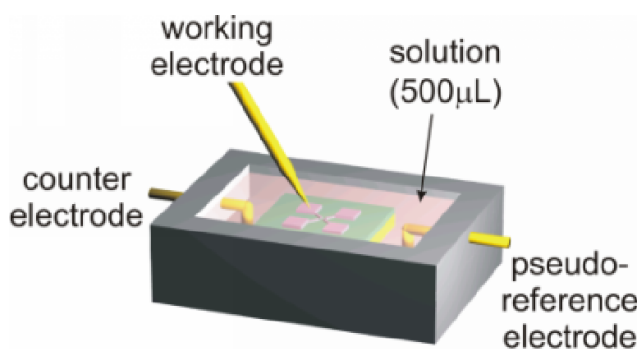
4.1 Noncovalent approaches

4.1.1 Strong organic donor and acceptor molecules

In order to explore the possibility of detecting charge transfer reactions by monitoring the conductivity of a single contacted nanotube, the well-documented strong electron donor tetrathiafulvalene (TTF) and the strong electron acceptor 7,7,8,8-tetracyanocyano-p-quinodimethane (TCNQ) depicted in Fig. 4.1 were used.

TTF is a nonaromatic molecule, which can be easily oxidized to its radical cation and dication species. Thus, TTF is an excellent electron donor. TTF has been used as a building block for a huge number of charge transfer salts that show very interesting properties in diverse fields ranging from superconductivity to organic metals, molecular shuttles and nonlinear optical media.

TCNQ on the other hand, is well known to be a good electron acceptor. Also for this molecule, a wide range of potential applications like high conductivity materials and TCNQ complexes with ferromagnetic behaviour have been demonstrated.

However, for the experiments described below, only the electron donor and acceptor properties of TTF and TCNQ are relevant. For contacted nanotube networks it has been shown [67], that after immersing the nanotubes in a solution containing TTF or TCNQ and putting them into a vacuum chamber at $\approx 10^{-10}$ bar the conductivity of the system is lower (TTF) or higher (TCNQ) than in the unmodified case. This observation can be
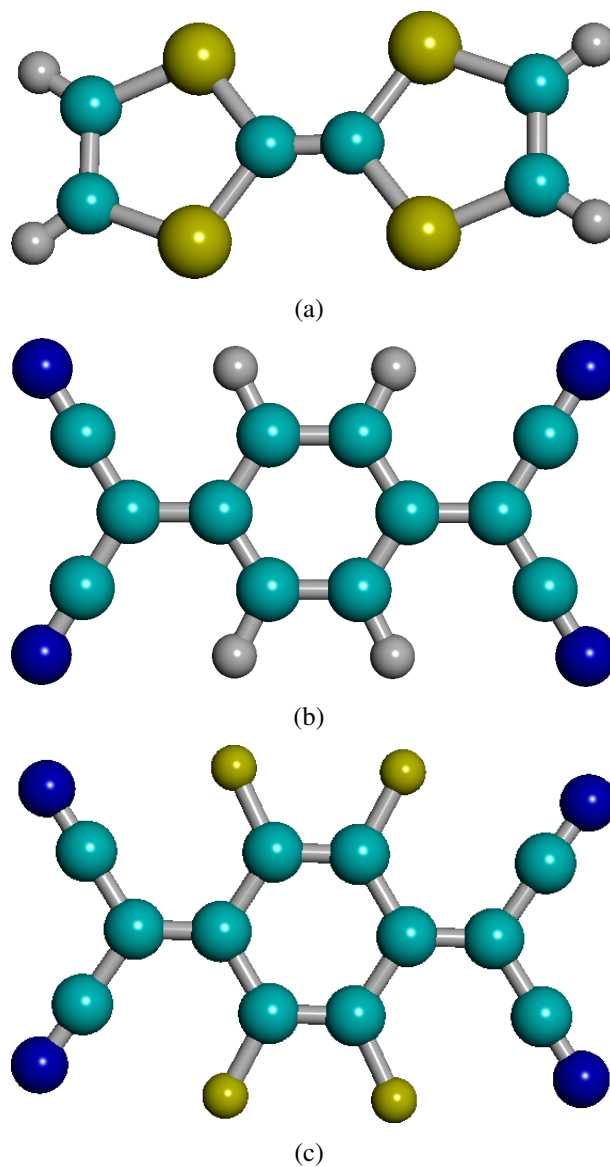
(a)

(b)

(c)

Figure 4.1: Molecular structure of (a) the electron donor TTF. Color coding: Carbon: cyan, Hydrogen: grey, Sulfur: yellow. (b) The electron acceptor TCNQ. Color coding: Carbon: cyan, Hydrogen: grey, Nitrogen: blue. (c) The fluorinated TCNQ. Color coding: Carbon: cyan, Nitrogen: blue, Fluorine: yellow.
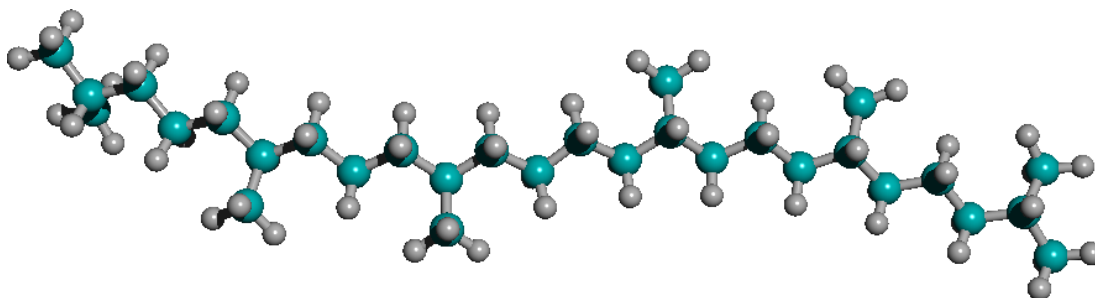
Figure 4.2: The branched alkane squalane is a non-polar molecule with a high boiling point. Color Coding: Carbon: cyan, Hydrogen: grey.

explained by the well-known p-type characteristic of carbon nanotubes due to adsorbed oxygen molecules: While TTF donates electrons and therefore less holes are available for the charge transport, the number of holes is increased in the case of TCNQ.

In order to test if this behaviour can also be observed for contacted individual nanotubes in a solution, a number of conditions have to be fulfilled:

- The solvent has to be non-conducting, since one would measure the current through the solution otherwise.

- The solvent should have a high boiling point. A high evaporation rate would lead to changes of the TTF/TCNQ concentration in the solution and thereby obscure the results.

- The solvent must be rather unpolar, since polar solvents like water interact with the nanotubes and strongly reduce the conductivity.

It is a difficult task to find a solvent that fulfils the requirements and additionally dissolves the charge transfer molecules. After a protracted testing phase squalane (2,6,10,15,19,23-Hexamethyltetracosane Fig. 4.2) was found to match most of our requirements. The branched alkane molecule has an extremely low conductivity, its boiling point is $176°$C and the molecule is very unpolar. However, whereas the solubility of TTF is acceptable, TCNQ is only slightly soluble in squalane. Therefore, TCNQ was substituted by a fluorinated form, F4-TCNQ (see Fig. 4.1), which is also a good electron acceptor and dissolves much better in squalane. The experimental setup was as follows: A source-drain voltage of 10mV was applied to semiconducting nanotubes. Subsequently, the sample was immersed in pure squalane solution. While the addition

of another drop of squalane did not lead to any sizable change in the nanotube's conductivity, the addition of a drop of TTF/squalane or F4-TCNQ/squalane solution resulted in a conductivity decrease or increase, respectively (see Fig. 4.3). This is a clear indication that charge transfer can indeed be measured in solution on a single nanotube.
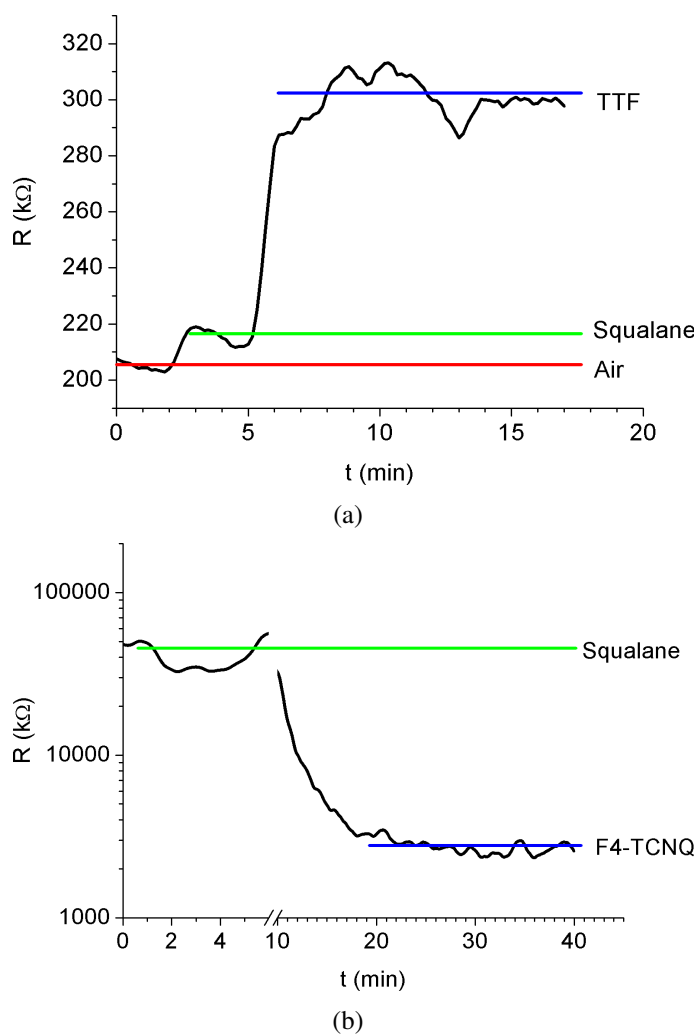

Figure 4.3: (a) Adding a TTF/squalane droplet to a squalane droplet on top of a contacted nanotube gives rise to a resistance increase, while (b) a F4-TCNQ droplet leads to a resistance decrease.
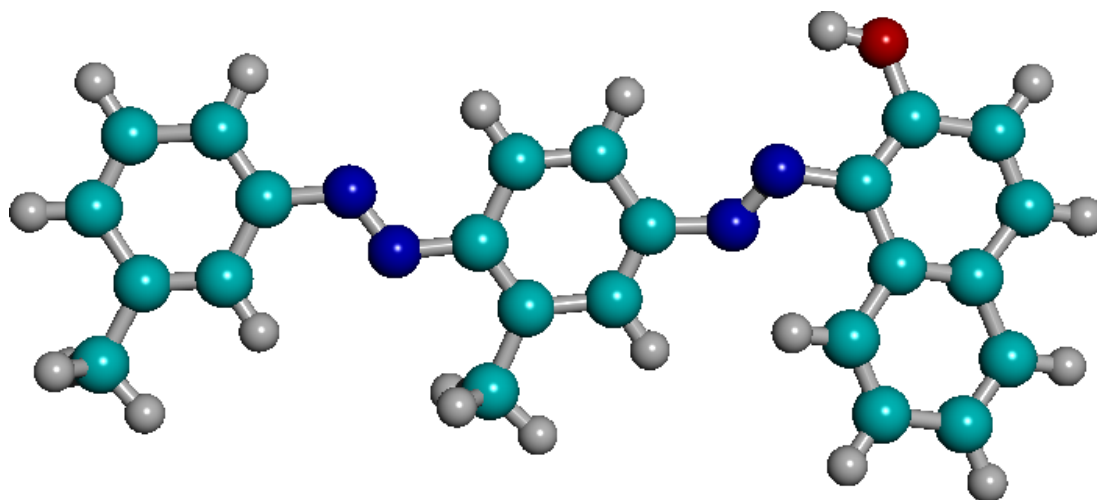
Figure 4.4: Chemical structure of Sudan Red B. Colour Coding: Carbon: cyan, Hydrogen: grey, Oxygen: red, Nitrogen: blue.

4.1.2 Sudan Red

Having shown that a noncovalent adsorption of molecules can indeed affect the nanotube's conductivity, it was investigated if a similar effect might be achieved by using a photoisomerizable molecule. Sudan Red B (Fig. 4.4) belongs to the azo dye family. This azo dye is commercially available and is used to colorize fats, oils and waxes. The dye mainly consists of two phenyl rings and one naphtalenic ring that are linked with N=N bridges. The molecule strongly absorbs light in the visible range below 600nm and exists in trans-trans, cis-trans, trans-cis and a cis-cis conformation. However, since the trans-trans state is energetically favourable the molecule is usually found in this conformation. Under light illumination the trans Sudan Red B can photoisomerize into one of the cis states. Relaxation back to the trans-trans state occurs thermally induced. The detailed mechanism of the trans-cis isomerization of the azo dyes is still under debate. Possible explanations are rotation of the N=N bond or inversion via a hybridized transition state. There appear to be two possible mechanisms for conductance switching induced by the Sudan Red B molecule, namely photoinduced charge transfer or a change in the orientation of the dipole moment of the dye caused by photoisomerization. While the first case would have a similar effect as the TTF/TCNQ experiments described before, in the latter case a conformational change of the molecule would result in an increase of the molecule's dipole moment. For the nanotube, this would have an effect similar to an additional gate.
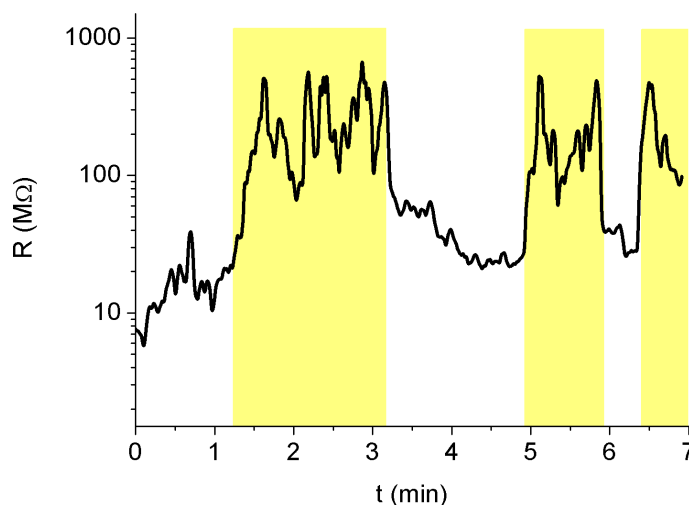
Figure 4.5: Photoinduced electric switching in a semiconducting carbon nanotube functionalized with Sudan Red B. Upon excitation with a laser ($\lambda_{exc} = 514nm$) the nanotube's resistance is increased by 1-2 orders of magnitude (yellow areas: light on).

A range of experiments were performed in order to distinguish between the two proposed photosensitive mechanisms: By adding a base to the solution, the OH group of the dye was deprotonated and a larger dipole moment of the dye was created. However, experiments have shown that even the mere addition of the base to a squalane solution without Sudan dyes significantly lowers the conductance and thus it was not possible to draw conclusions from the deprotonation experiments.

Alternatively, the switching mechanisms should be clarified by studying different commercially available Sudan dyes (Fig. 4.6). Indeed, there are some hints, that Sudan dyes with larger dipole moment lead to stronger resistance changes than those with smaller dipole moments. However, the commercially available dyes usually differ in more than just one functional group and thus it is not straightforward to compare the results of the different dyes. A general problem of the experiments was the low reproducibility between different samples. Using seemingly identical configurations one would end up with considerably different results ranging from no effect on the conductivity to a strong conductivity decrease by several orders of magnitude.
Summarizing the Sudan dye experiments, photo-induced conductance switching can be observed for Sudan-functionalized semiconducting carbon nanotubes. However, due to the small reproducibility an unambiguous clarification of the switching mechanism
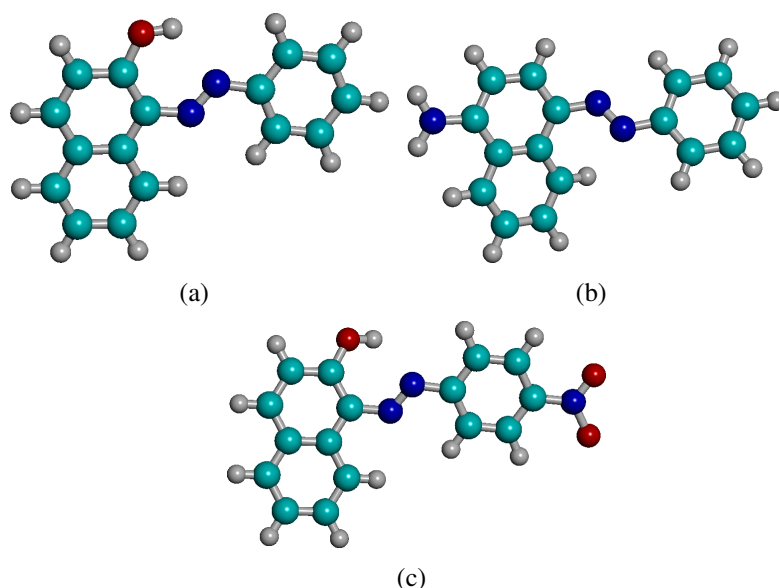
Figure 4.6: Some of the other *Sudan* molecules tested are (a) Sudan I, (b) 1 naphtyl hydrochloride, and (c) Para Red. Color coding: Carbon: cyan, Oxygen: red, Hydrogen: grey, Nitrogen: blue.

could not be achieved, even though there are some hints that the mechanism is driven by a photoisomerization process.

4.1.3 Nanoswitch based on Zn-porphyrin

A porphyrin molecule consists of four pyrrole subunits linked through 4 methine bridges. Porphyrines are known to be dye molecules due to their extended conjugated system. They show an intense absorption around 400nm (extinction coefficient $> 2 \cdot 10^5$) and a second group of absorption peaks between 450nm and 700nm. Furthermore, porphyrines are known to coordinate with metal ions such as Zn or Fe in the the molecule centre(Fig. 4.7 a). While the free porphyrin can π-stack on a carbon nanotube, the metal complexed form is known to be unable to bind to carbon nanotubes [74].

It is well known from the literature that a phenylazopyridine molecule can undergo a photoisomerization from its trans to its cis conformation (Fig. 4.7 b, c), essentially like the previously described Sudan Red dye molecule. In its trans-form, the phenylazopyridine should coordinate to the Zn cation via chelation, allowing the complexed porphyrin to mimic "free" porphyrin and adsorb onto the nanotube surface. By contrast,

(a)

(b)   (c)
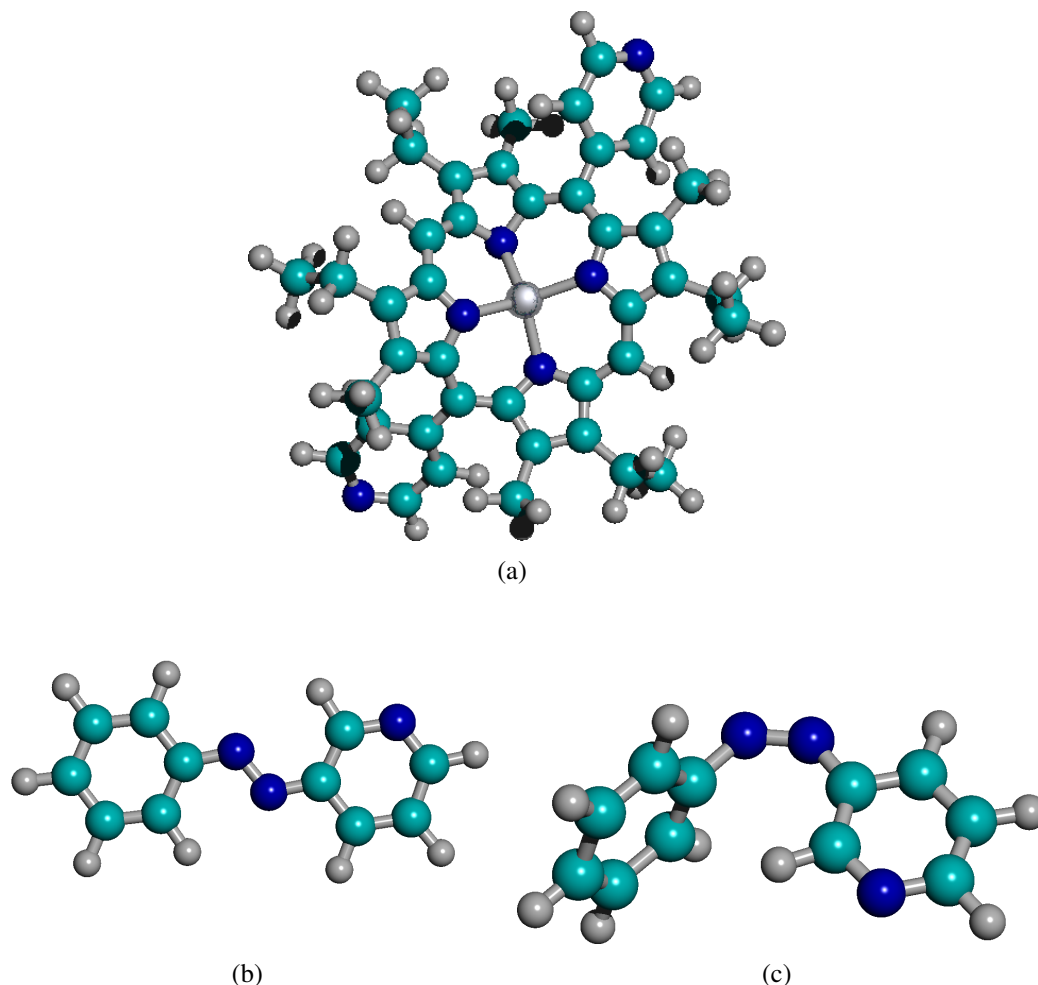
Figure 4.7: The constituents of the "nanoswitch": (a) Zn-complexed porphyrin, (b) azopyridine in trans and (c) Azopyridine in cis conformation. Colour coding: Carbon: cyan, Nitrogen: blue, Hydrogen: grey, Zinc: grey

in the cis-form of the phenylazopyridine, the coordination to the Zn should be much weaker because of steric hindrance and thus the chelation of the Zn to the porphyrin should remain unaffected [75, 76]. Therefore, in this case also the resistance of the nanotubes should not change. The principle of a nanoswitch based on this concept is presented in Fig. 4.8.

Experimentally, it could be verified that free porphyrin induces a conductivity decrease in semiconducting nanotubes, whereas Zn-complexed porphyrin does not affect the conductivity (Fig. 4.9). However, when testing the azopyridine molecules it was noticed that they gave a much stronger change of conductivity than the porphyrin itself. In fact,

Figure 4.8: Working principle of the nanoswitch: Depending on whether the azopyridine is in trans or cis conformation, the Zn-porphyrin can or cannot interact electronically with the nanotube.
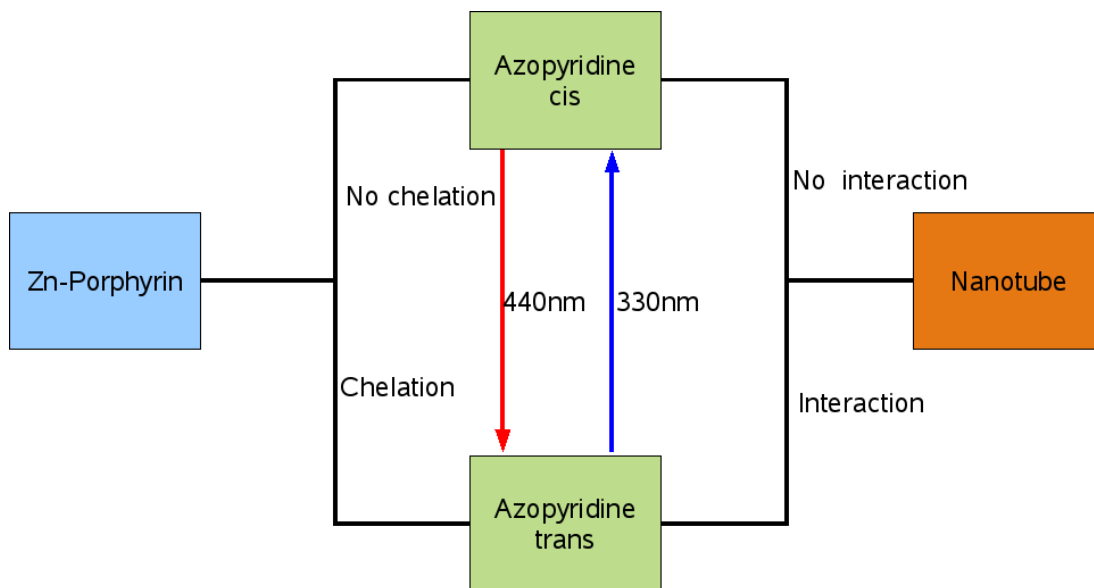
the addition of pyridine obscures the conductivity changes induced by the complexed or uncomplexed porphyrin, making the originally devised switch impossible to realize in the current form.

4.1.4 Bis-anthracene compound

The molecule bis-anthracene (Fig. 4.10) was synthesized by our cooperation partners, the lab of C. Mioskowski at CEA/Saclay in Paris (France). The molecule exists in two conformations. One conformation consists of two stacked anthracene rings, one of which should be able to bind to the nanotube surface noncovalently (π-π stacking). By contrast, when the molecule is switched into its second conformation, the resulting photodimer should not be able to bind to the nanotube due to steric hindrance. Switching between the two conformations should be possible by light with a wavelength $\lambda_1 < 300nm$ (planar $\longrightarrow$ photodimer) and $\lambda_2 > 300nm$ (photodimer $\longrightarrow$ planar). Experimentally, the molecules's solubility was problematic, since the molecule proved to be almost completely insoluble in squalane, our favourite solvent for many reasons (section 4.1.1 on page 59). After a detailed solubility testing tetrahydrofuran (THF) was
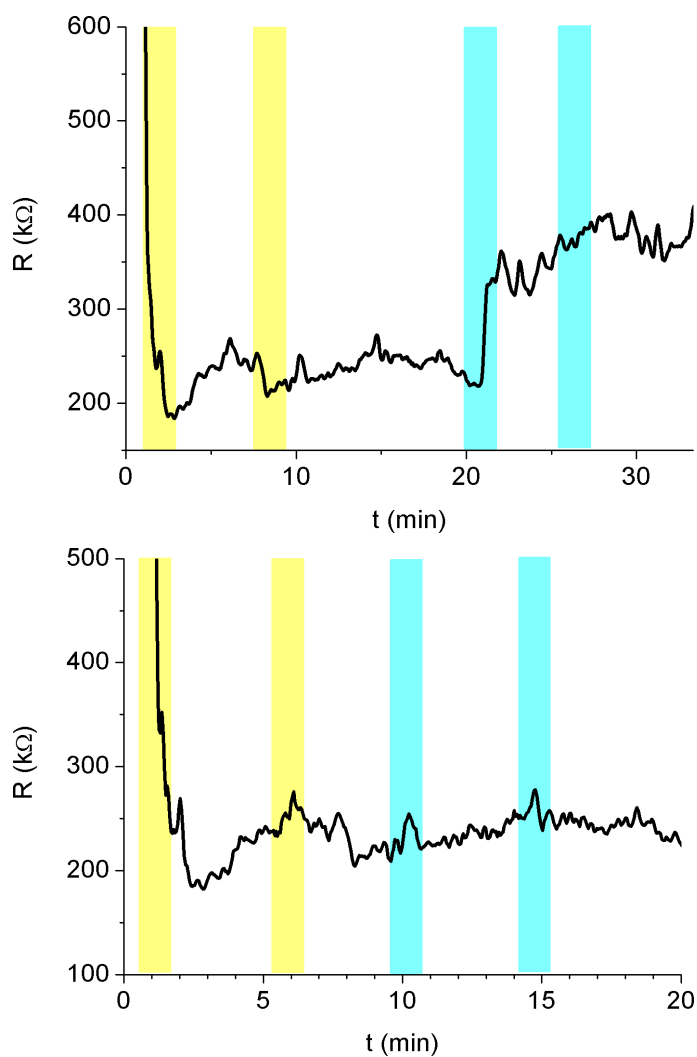
Figure 4.9: (a) (b) The nanotube's resistance changes, when it is immersed into the solvent (dichloroethane, DCE) (1st yellow bar). Adding DCE a second time does not further increase the resistance (2nd yellow bar). Whereas (a) adding a free porphyrin/DCE solution leads to a sizable resistance change, a (b) Zn-complexed porphyrin/DCE solution does not alter the nanotube's resistance (1st cyan bar). Adding any of the porphyrin/DCE solutions a second time leaves the resistance largely unaffected (2nd cyan bar).

(a)

(b)   (c)

Figure 4.10: (a) In its planar form the bis-anthracene should be able to π-stack on the nanotube. For clarity (b) shows the planar form without sidegroups. (c) In its photodimerized form (simplified form shown for clarity) π-stacking should not be possible due to steric hindrance. Colour coding: Carbon: cyan, Oxygen: red, Nitrogen: blue, Hydrogen: grey, Sulfur: yellow

selected, since it dissolved the bis-anthracene reasonably well. However, due to is its low boiling point of only 65°C it proofed to be a challenging task to work with small droplets of $\approx 100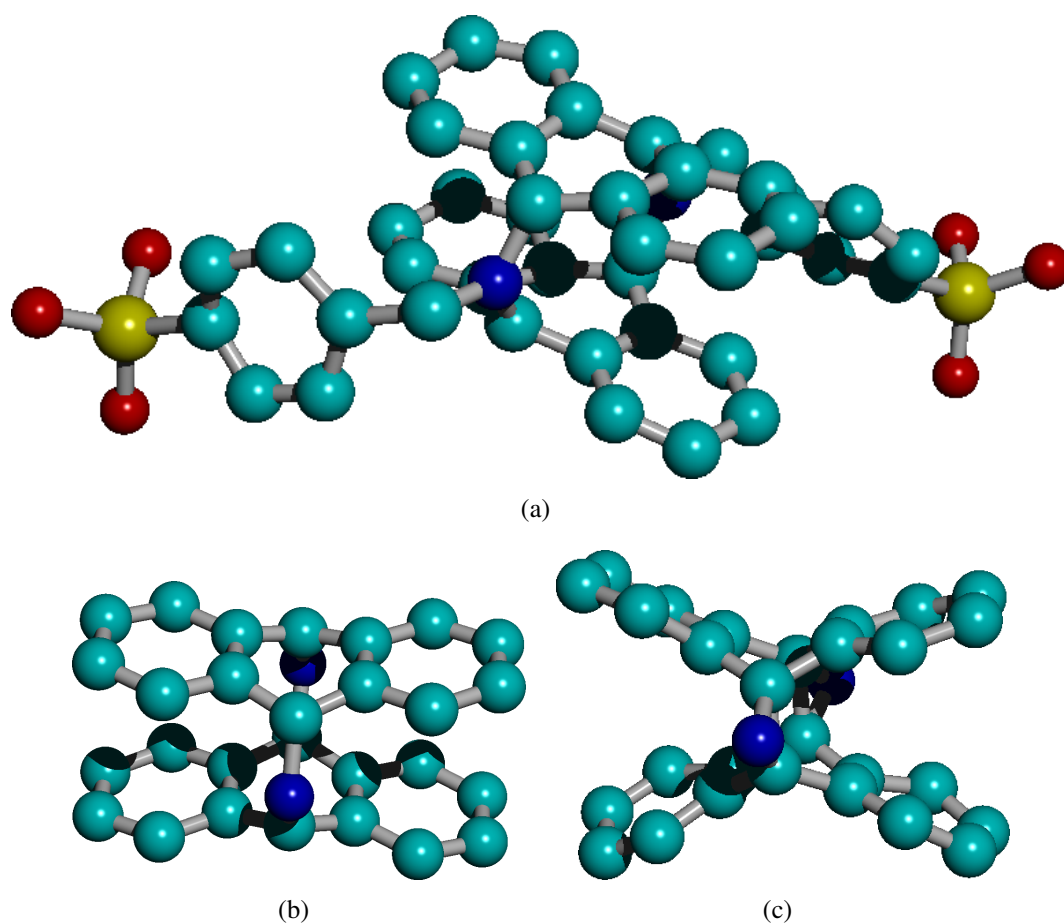nl$. A specific configuration which allowed for a substantially bigger amount of solution had to be constructed, since the standard sample configuration only allowed for measurement time of $\approx 15s$, until the solvent had been evaporated completely. While with the improved setup conductance measurements were possible over several minutes, the new cell made it much more difficult to illuminate the sample due to the working distance of the confocal laser microscopy objectives (typically 1-2mm). However, since the switching from the 2D bis-anthracene to the 3D photodimer occurs only at wavelengths $< 300nm$, no suitable laser line was available in the confocal laser scanning microscope ($\lambda_{\min} = 458nm$) and therefore, a UV hand lamp ($\lambda_{\mathrm{exc}} = 258nm$) had to be used.

A detectable conductivity change upon adsorption of the planar could never be observed and therefore, also the UV-induced photoisomerization did not have a discernible effect on the nanotubes' conductivity. It can be inferred, that the π-stacking probability of the anthracene molecule in both conformations is very low. Furthermore, most of the investigations were performed with HiPco nanotubes and thus might be hampered by residual bundling effects: In a nanotube bundle, a significant part of the nanotubes' surface is not available for dye molecule π-stacking and therefore, the dye absorption and desorption would not affect the nanotube's conductivity to a sizable extent.

4.2 Covalent approaches

4.2.1 Pentacene derivative

Pentacene is an aromatic hydrocarbon molecule that comprises 5 fused benzene rings. Pentacene appears as a dark-blue powder which is unstable under oxygen exposure. The pentacene derivative (Fig. 4.11) was synthesized by the group of C. Mioskowski at the University of Illkirch in Strasbourg, France. It exhibits amphiphilic characteristics due to the hydrophobic pentacene molecule and the hydrophilic end groups, which render the molecule water-soluble.
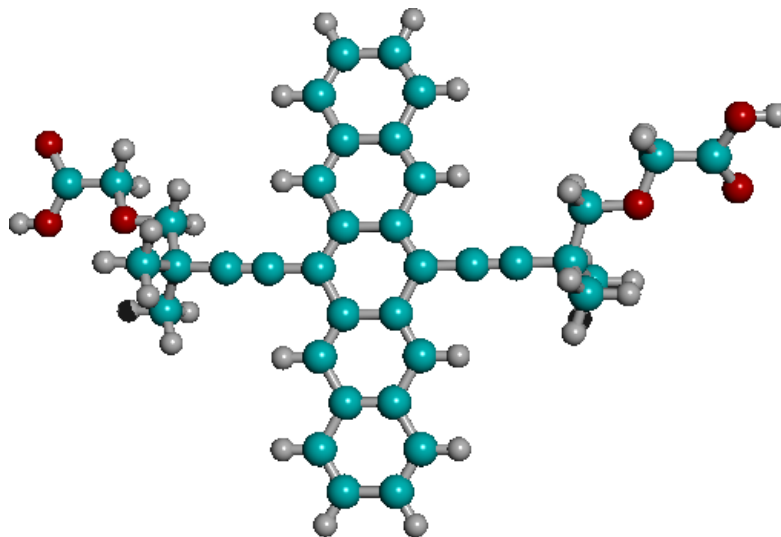
Figure 4.11: Molecular structure of the pentacene derivative. Color coding: Carbon: cyan, Hydrogen: grey, Oxygen: red.
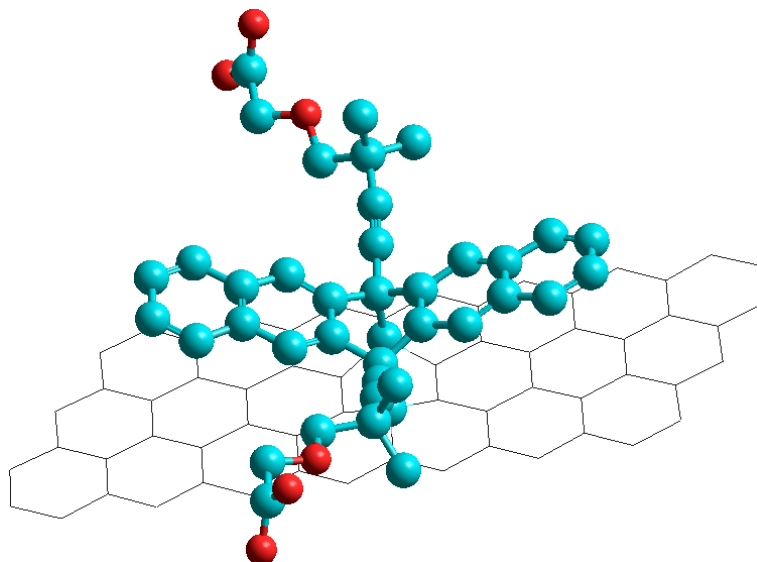

Figure 4.12: Illustration of a pentacene derivative attached to a nanotube.

The oxygen sensitivity and thermal instability of the molecule posed serious problems. All of the samples of pentacene powder that arrived from Strasbourg were already decomposed. Therefore, another sample was sent from the group in Strasbourg, this time a frozen aqueous solution containing the pentacene derivative and a tris buffer (tris hydroxymethylaminoethane). While this solution proved to be more stable against thermal decomposition, the tris buffer was found to remove the Au/Pd electrodes from the substrate. Therefore, reliable studies on changes in nanotube conductivity have not been possible with the pentacene derivative/tris buffer solution. However, using the pentacene/tris solution, it was at least possible to show, that π-stacking takes place by dispersing raw nanotube material in the pentacene/tris aqueous solution. After a thorough centrifugation of the suspension the supernatant was put on a SiO_2 sample. AFM images clearly show, that there are a number of nanotubes on the surface, which is only possible due to the amphiphilic pentacene derivative (Fig. 4.13 b).

After successful π-stacking to the nanotube the pentacene derivative should form covalent bonds with the nanotube, via photo-induced cycloaddition. The resulting disruption of the π-conjugated system was expected to lower the conductivity of the nanotubes. Upon illumination with a different wavelength the original state should be restored. An analysis several samples by confocal Raman spectroscopy was performed in cooperation with A. Mews group in Siegen. The photo-induced cycloaddition to the nanotube would create defects in the nanotube sidewalls, which would be manifested in an increase in the Raman D-band and in the $\frac{\text{G-band}}{\text{D-band}}$ ratio. However, the investigation of many samples did not reveal a sizable change of the $\frac{\text{G-band}}{\text{D-band}}$ ratio (Fig. 4.13 a).

4.2.2 Acridine diazonium salt

The attachment of diazonium salts to nanotubes by electrochemistry has been described in the introductory chapter already (see Fig. 2.25 on page 34). The main idea of this project was to use a diazonium salt containing a chromophore. Upon illumination, the attached diazonium molecule would inject charge carriers and thereby alter the tube's conductivity. The compound chosen for this purpose is an acridinediazonium salt (see Fig. 4.17 a). The synthesis of the molecule was carried out by the group of C. Mioskowski at the CEA/Saclay (France).

(a)

(b)
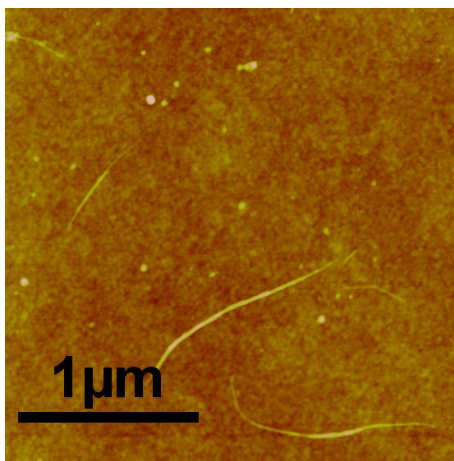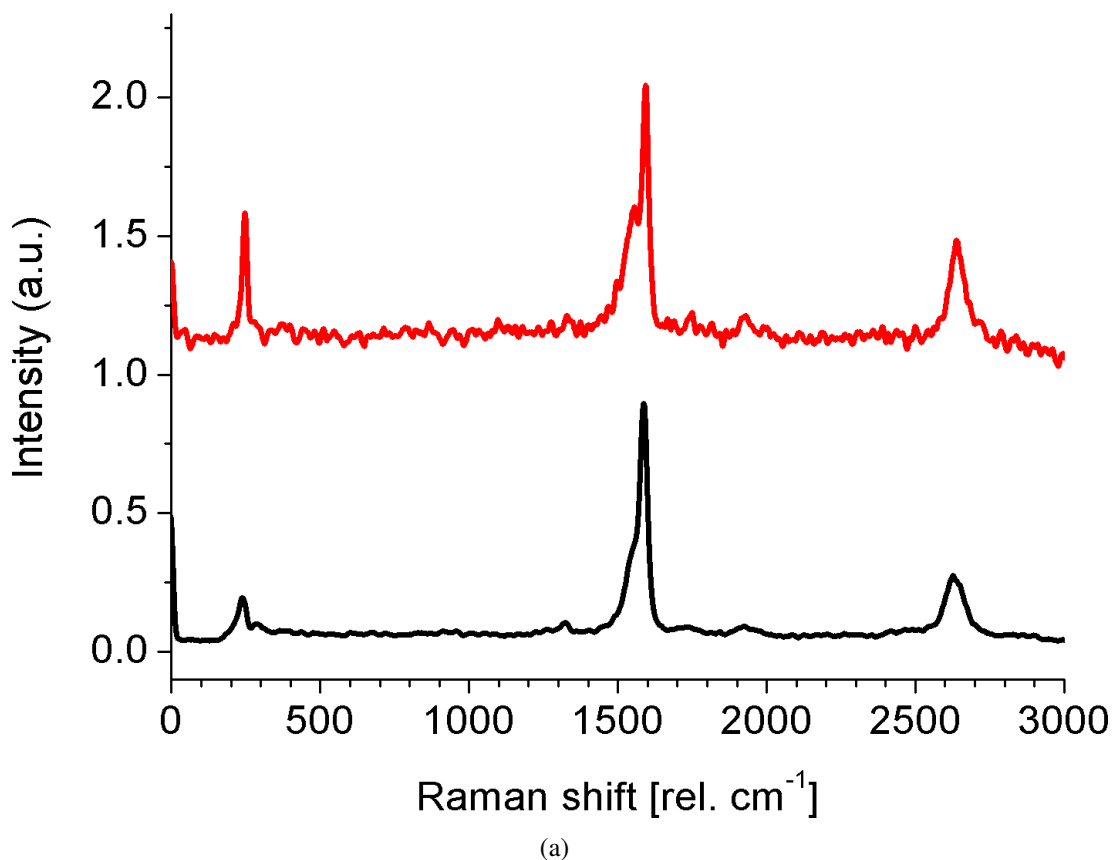
Figure 4.13: (a) Raman spectrum of a unmodified nanotube (black curve), and of the same nanotube after deposition of the pentacene derivative and illumination with $(\lambda_{\mathrm{exc}} = 633 nm)$ (red curve). The Raman D-band at $1330 \mathrm{cm}^{-1}$ has not increased significantly, and thus covalent bonds to the nanotube have not been formed. (b) The pentacene derivative can π-stack on the nanotube and acts as a surfactant in aqueous solutions. The AFM shows nanotubes which have been brought into suspension by the pentacene derivative.

(a)   (b)
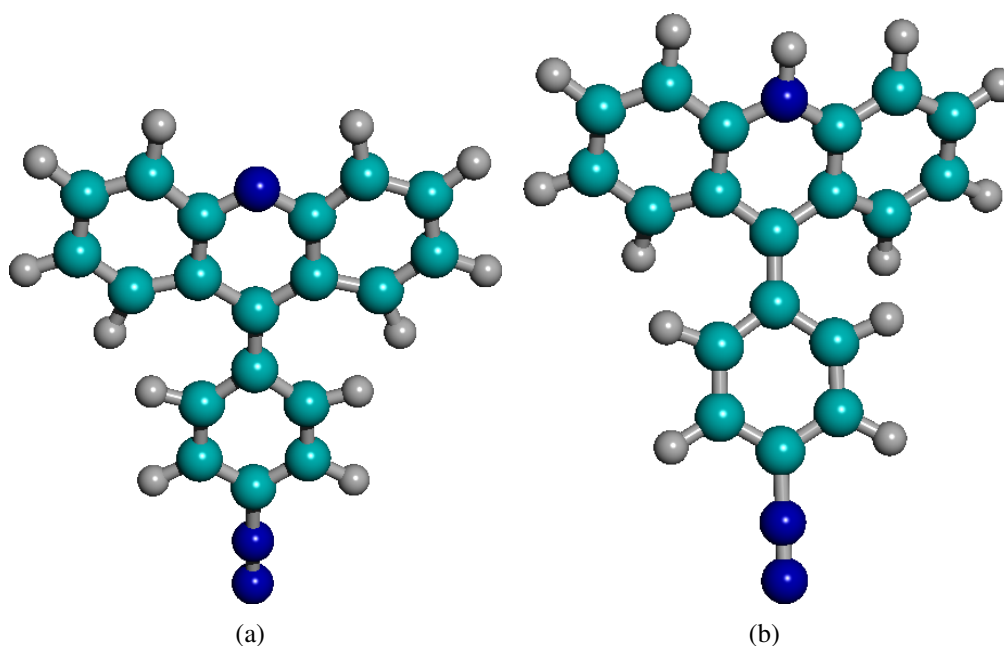
Figure 4.14: Chemical structure of the acridine diazonium salt. (a) displays the "normal" acridine diazonium, (b) The protonated form which should be less susceptible towards polymerization. Colour coding: Carbon: cyan, Hydrogen: grey, Nitrogen: blue.

By using electrochemistry, the acridine compound could be successfully attached to semiconducting and metallic nanotubes, as reflected by the height increase of the nanotubes in the AFM images (Fig. 4.15), an increase in the Raman D-band (Fig. 4.16), and a reduced electrical conductivity of the nanotubes (Fig. 4.17 a). Since the acridine has an optical absorption maximum at 360nm, the setup in our lab ($\lambda_{\min} = 458nm$) could not be used. Instead, the photoelectric transport measurements were carried out with a handheld UV lamp ($\lambda = 365nm$). However, the photoswitching effect for nanotubes with attached acridine could not be distinguished from that of the bare nanotube (see Fig. 4.17). The surprisingly strong photoresponse of the bare semiconducting nanotube most likely results from photodesorption of oxygen and water molecules, whereas the absence of an increased sensitivity may be explained by the formation of a multilayer of acridine around the nanotube (polymerization), whereupon the chromophore of the molecule might be destroyed. This assumption was tested with a protonated acridine molecule (Fig. 4.14 b). In its protonated form, the compound should be less susceptible towards polymerization and therefore enable the formation of a monolayer of acridine on the nanotube. However, a significant diameter increase was
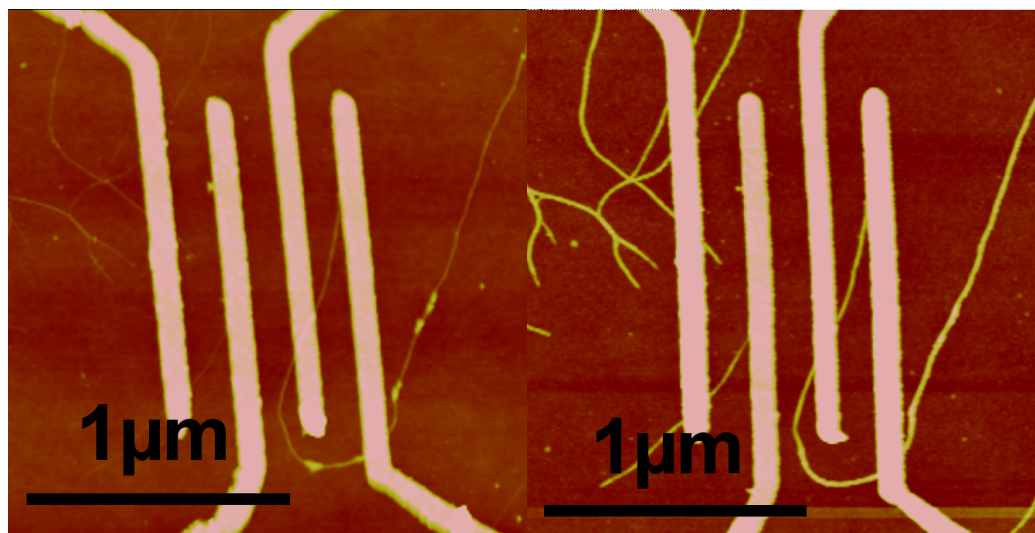
Figure 4.15: (a) comprises an AFM image of contacted HiPco nanotubes. (b) shows the same nanotubes after the electrochemical attachment of acridine diazonium salt.
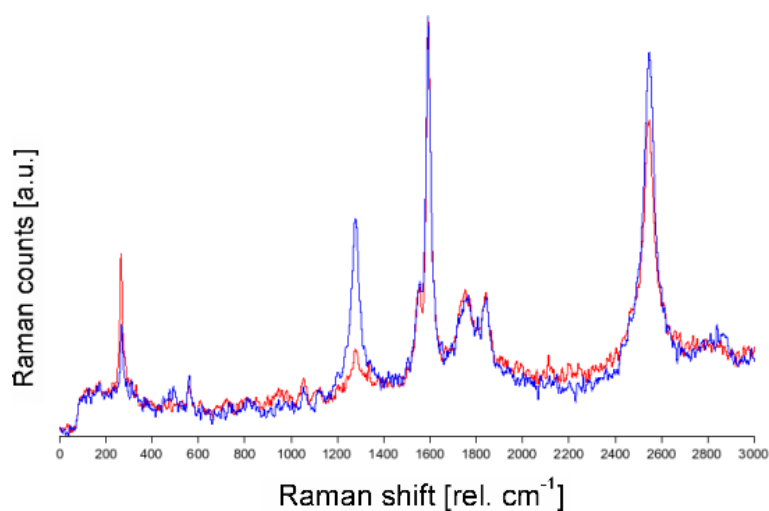
Figure 4.16: Bulk Raman spectrum of unmodified (red line) and acridine-modified nanotubes (blue line). An increase of the Raman D-band intensity is clearly observed.
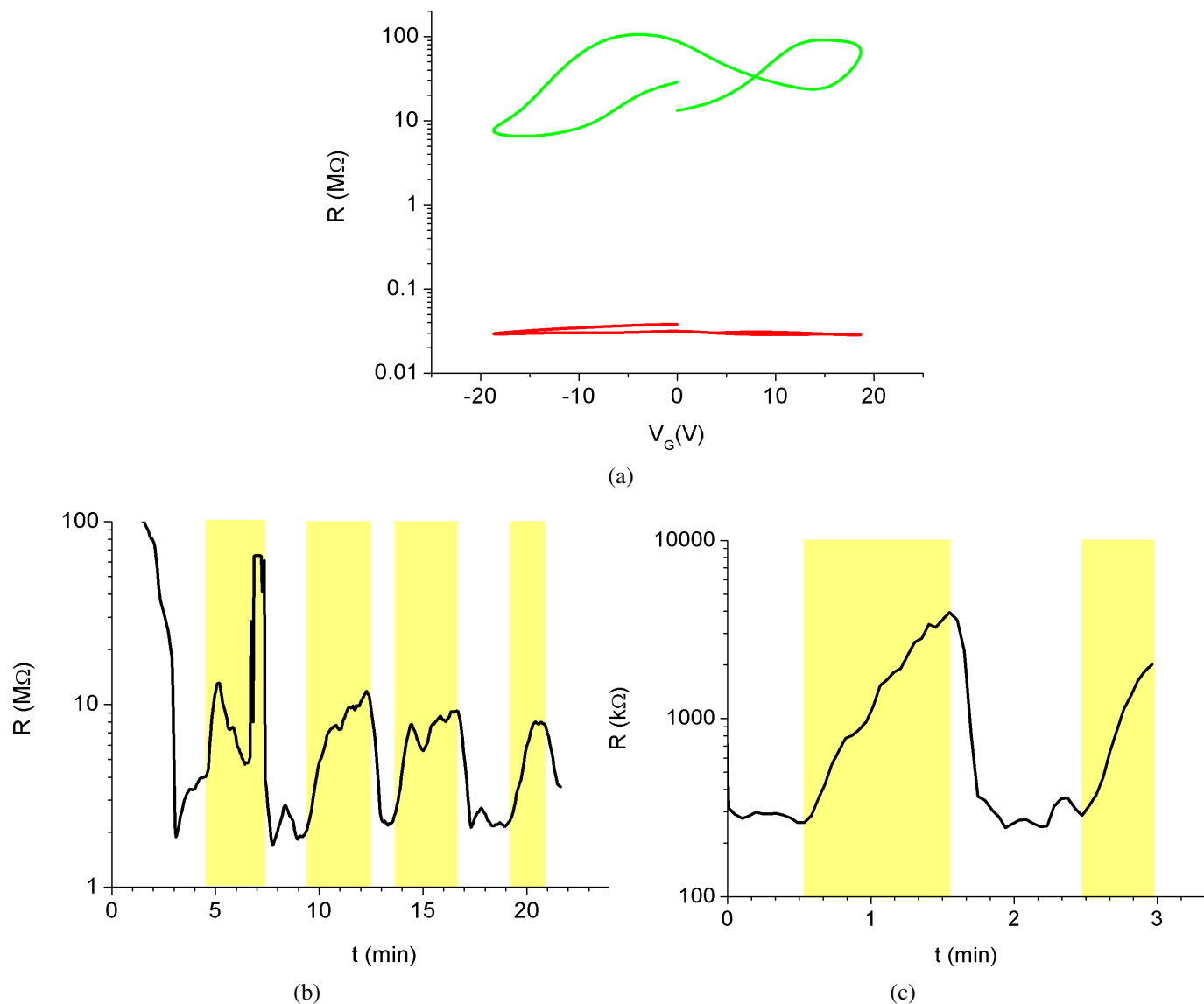
Figure 4.17: (a) In the process of the electrochemical attachment defects are formed in the nanotube. They lead to an increased charge carrier scattering in the nanotube and therefore to a resistance increase (red curve: unmodified nanotube, green curve: functionalized nanotube). (b) Using a UV lamp ($\lambda_{max} = 365nm$) (yellow areas), the resistance of a nanotube is increased by approx. one order of magnitude. (c) A similar switching effect already occurs for the unmodified nanotube, however.
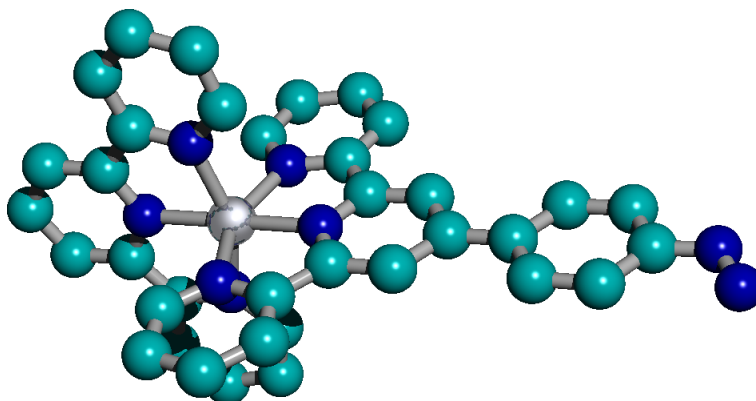
Figure 4.18: Chemical structure of the Ruthenium-based dye. Color coding: Carbon: cyan, Nitrogen: blue, Ruthenium: grey

still found after the electrochemical reduction step, which shows that polymerization is not suppressed for the protonated acridine. In agreement with this observation, no sizable photoconductivity effect was found. Besides the polymerization a possible explanation might be the low light intensity of the unfocused UV lamp. Therefore another diazonium molecule with a very similar coupling mechanism, but with a chromophore that absorbs in the visible range was investigated, as described in the following section.

4.2.3 Diazonium salt with Ruthenium-based chromophore

Another diazonium salt was synthesized by B. Joussselme at CEA/Grenoble (France). The dye has a broad absorption in the visible range and is therefore ideally suited as a light-harvesting molecule. Molecules with similar chromophores have been used e.g. in TiO_2 based solar cells. Using the electrochemical methodology described for acridine diazonium salt the ruthenium based diazonium salt was attached onto the sidewalls of semiconducting and metallic carbon nanotubes. Similar to the results of the acridinium an increase of the nanotube height by AFM and a reduced conductivity were observed.

The main difference of the Ru based dye is its ability to absorb light over the complete visible range. Therefore, our confocal laser scanning setup could be used to specifically illuminate the functionalized nanotube with a diffraction-limited laser spot ($\varnothing \approx 1 \mu m$),

thus providing a much higher intensity than the unfocused UV lamp for the acridinium dye. Nevertheless, a sizable photoconductivity effect could not be detected, which might again be due to polymerization of the diazonium component, as discussed in the previous section.

5 Carbon Nanotubes functionalized with metal nanoparticles

Electrodeposition of noble metal nanoparticles onto contacted carbon nanotubes has been demonstrated for palladium, platinum, silver and gold [77]. The principle of the deposition is surprisingly simple: Metal ions in an aqueous solution are reduced to metal nanoparticles on the nanotube by applying a voltage between the nanotube working electrode and a reference electrode. According to the literature an oxidative pretreatment of the nanotubes is essential for the successful deposition of the nanoparticles [78]. By contrast, the present study successful deposition was achieved by using as-grown nanotubes without oxidative pretreatment.

5.1 Electrodeposition of metal nanoparticles on carbon nanotubes

Since the aim of the present study was to investigate changes of the nanotube's Raman properties induced the nearfield of metal nanoparticles. Metals with an absorption band in the visible range were selected for the experiments. Additionally, noble metal clusters were preferentially considered in order to minimize problems with oxidation. Based on these criteria, silver, gold and palladium were selected for further investigations.
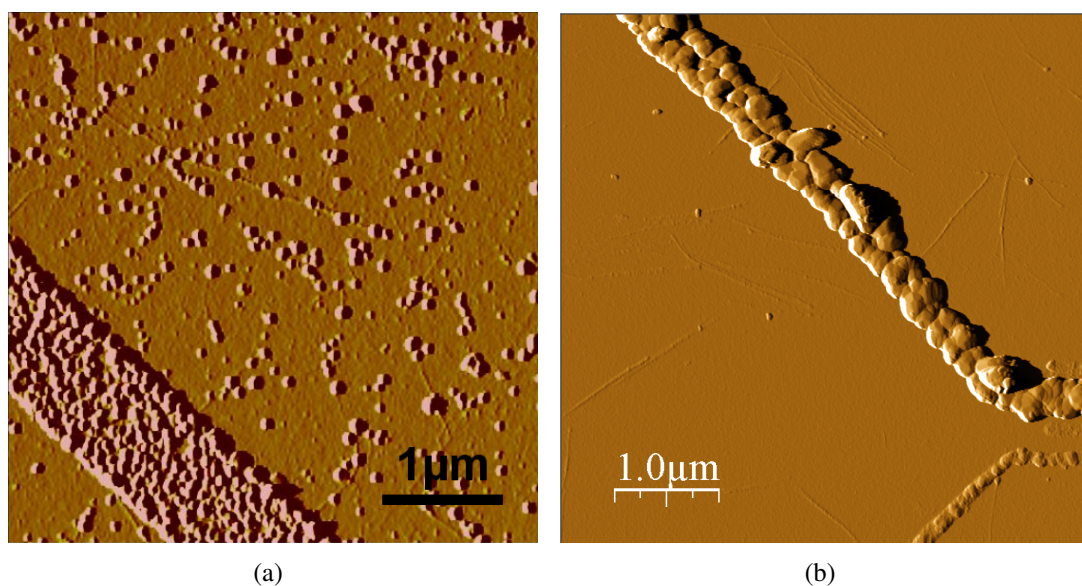
Figure 5.1: (a) AFM images of silver nanoparticles on top of carbon nanotubes, deposited from $AgNO_3$. (b) Silver-coated electrode, obtained from from $KAg(CN)_2$. No nanoparticles are formed on the nanotubes.

5.1.1 Electrodeposition of silver nanoparticles

For the electrochemical deposition of silver nanoparticles on carbon nanotubes two different approaches were followed:

- **$AgNO_3$** in aqueous solution, with KNO_3 serving as background electrolyte and poly-vinylpyrrolidone as surface stabilizing agent [79]. Electrochemical growth of silver nanoparticles was straightforward to achieve; the result of the electrodeposition is shown in Fig. 5.1 a. However, the approach suffered from two shortcomings: First, the particle density could not be sufficiently controlled, since a change in the deposition parameters mainly affected the particle size and not the density. Second, the silver nanoparticles did not give a sizable SERS signal. A possible explanation for this observation could be an oxidation of the silver nanoparticles. Indeed, oxidation could be observed on a silver-coated electrode, which turned black after a few minutes under ambient conditions. Also, it is known from the preparation of roughened silver substrates that great care needs to be exerted in order to avoid oxidation. Due to the oxidation problems during

electrodeposition from $AgNO_3$, an alternative route was investigated.

- Adapted from [80], **KAg(CN)$_2$** was used in aqueous solution, with KCN serving as background electrolyte and $K_4P_2O_7$ as surface stabilizer. However, while the silver could easily be deposited on the Au/Pd electrodes which contact the nanotubes, no silver nanoparticles were formed on the nanotubes regardless of the deposition parameters (Fig. 5.1 b).

5.1.2 Electrodeposition of palladium nanoparticles

For the deposition of palladium nanoparticles, $Na_2 [PdCl_4]$ was dissolved in ethanol, with $LiClO_4$ as a background electrolyte [81]. Electrochemical reduction readily occurred and nanoparticles could reproducibly be grown on nanotubes. An example is shown in Fig. 5.2. However, it was difficult to control the size and separation of the nanoparticles; in most cases, nanoparticles with a diameter of ($\varnothing \leq 20nm$) and an average distance of less than 100nm were formed. No sizable SERS enhancement was found, which might be due to the small particle size.
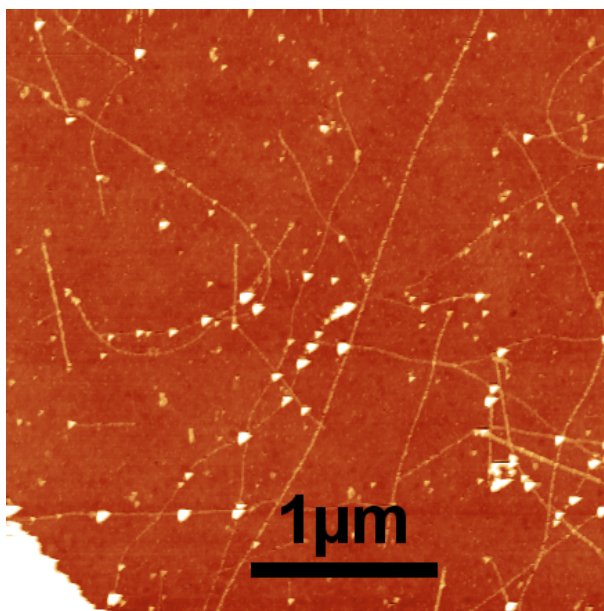

Figure 5.2: AFM image of palladium nanoparticles on contacted carbon nanotubes.

5.1.3 Electrodeposition of gold nanoparticles

In order to enable a better controlled gold nanoparticle deposition (nanoparticle size and spacing), the electrodeposition approach from [78, 82] was adapted. Changes in the modification approach were geared towards a maximum nanoparticle density of one nanoparticle per micron, since the individual nanoparticles were to be investigated by Raman spectroscopy with a diffraction limited laser spot ($\varnothing \approx 500nm$). In order to reach this level of control, a number of improvements had to be made on the previous approaches:

- By implementing a setup consisting of **three electrodes**, it was possible to compensate for voltage offsets that occurred up during the modification.

- The use of a **background electrolyte** increased the conductivity of the solution. Therefore, a more homogeneous deposition of nanoparticles on the nanotubes could be achieved.

- The addition of the **surface stabilizer** poly-vinylpyrrolidone has been shown to allow better control of the deposition rate for silver nanoparticles due to more homogeneous dispersion of the ions in the solution [79]. The surface stabilizer also allowed for a more controlled gold nanoparticle deposition.
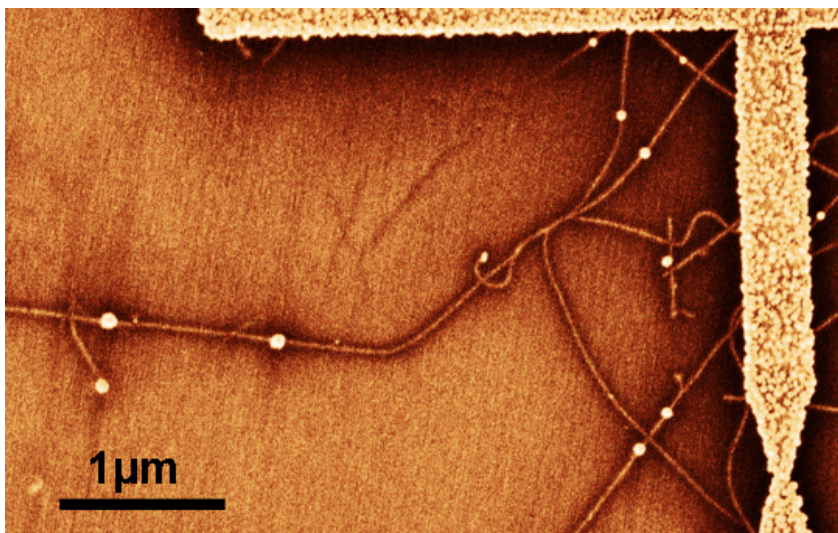

Figure 5.3: Electrochemical growth of individual gold nanoparticles on carbon nanotubes

Using the improved growth technique, well-separated nanoparticles between 10nm and 150nm diameter with a narrow size distribution could be grown. Moreover, several consecutive growths could be performed in order to increase the gold cluster size (Fig. 5.4 a). During a second growth, no new gold nanoparticles were formed, but instead the nanoparticles from the first growth increased in size. This can be interpreted by a defect nucleation model: The nanoparticles preferentially grow at defect sites, since charge transfer can more easily occur at these points. During the second growth, the defects are already covered with gold nanoparticles and thus no new particles are created. Instead, the existing nanoparticles act as seeds for the second growth. The nanoparticle size is proportional to the number of growth processes (Fig. 5.4 b).

The nanoparticle density was found to be identical on semiconducting and metallic nanotubes. In a recent paper this effect has been explained by an effective smearing out of the EDOS, which causes the reduction potential of semiconducting and metallic nanotubes to be very similar. Additionally, since semiconducting and metallic nanotubes have been shown to have comparable defect densities [83], similar nanoparticle densities can be expected.

5.2 Electrical transport studies

Contacted individual CVD-grown nanotubes were used to determine the influence of electrochemically attached gold nanoparticles on the transport properties. In agreement with the defect nucleation model the conductivity is largely unaffected by the nanoparticle decoration for low reduction voltages (Fig. 5.5a). A tiny resistance increase observed for most samples is attributed to changes of the contact resistance between electrode and nanotube. For a highly decorated nanotube more defects were created and a pronounced conductivity decrease could be observed (Fig. 5.5b).
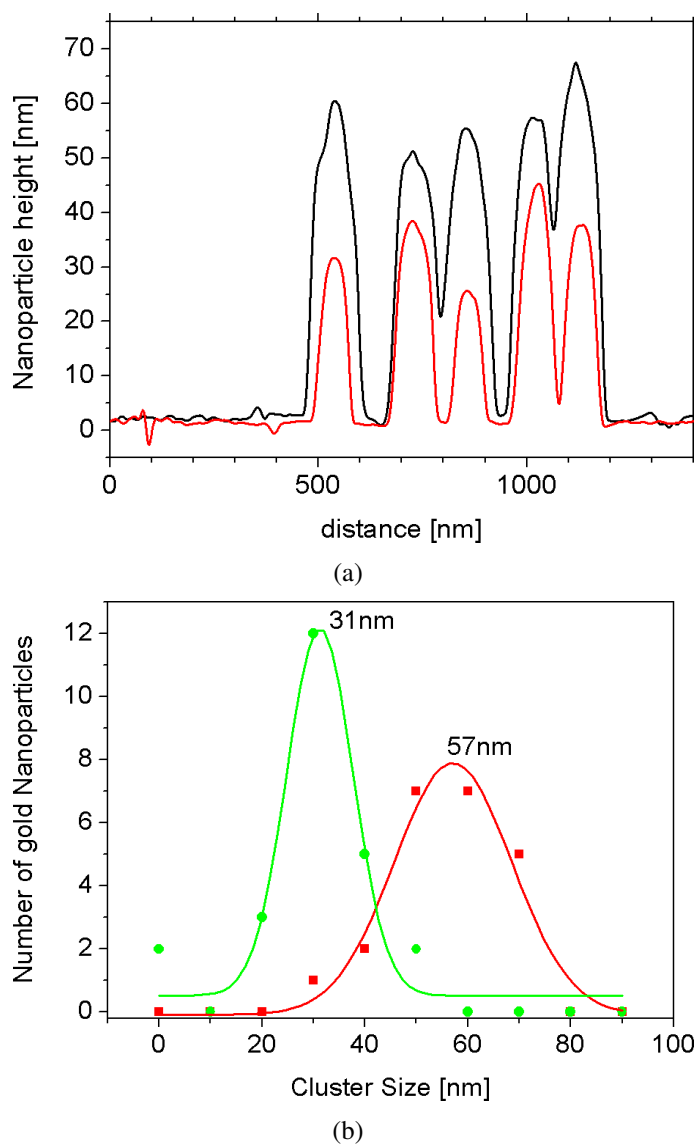
Figure 5.4: (a) AFM line profile of gold cluster on a nanotube after one (red) and two (black) identical growth steps. (b) The histogram shows the size distribution of gold nanoparticles after one growth step (growth time: 15s) (green) and two growth steps (growth time: 30s)(red).
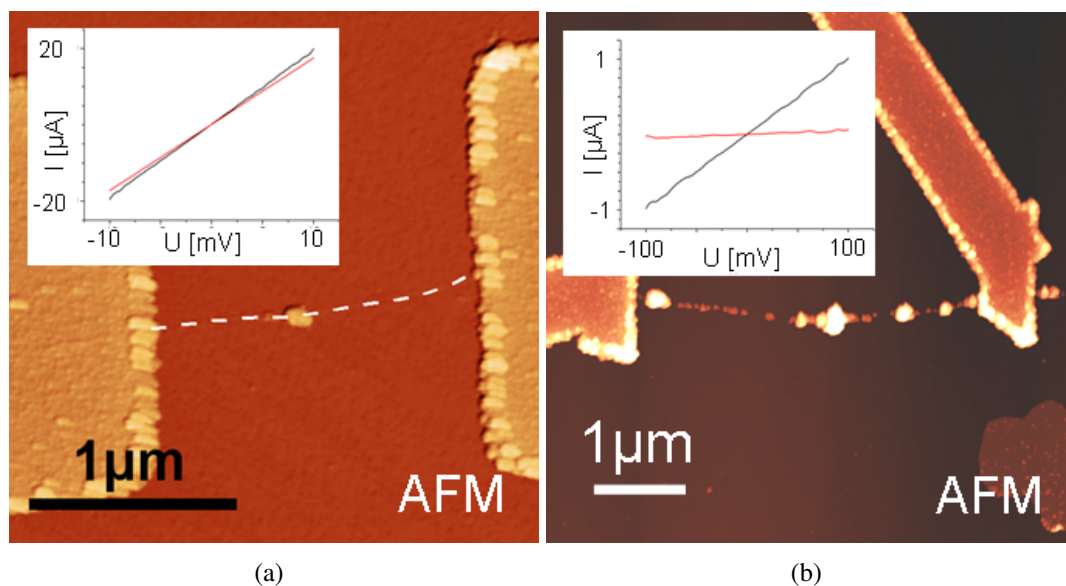
Figure 5.5: (a) AFM image of a gold nanoparticle located on an individual nanotube between two electrodes (reduction voltage: -0.8V). The position of the nanotube has been highlighted by a dashed line. The inset shows an almost unchanged IV-curve.(b)High density decoration (reduction voltage: -1.1V). The IV-curve inset shows a prounounced resistance increase

5.3 Photoluminescence studies

The general effect of gold nanoparticle decoration on the spectroscopic response of the SWNTs is apparent from Fig. 5.6, which displays a set of images acquired from a CVD-grown nanotube at the Raman G-band frequency for different wavelengths. The corresponding AFM image (Fig. 5.6a) shows well-separated (average distance: 100nm) gold particles. In the G-band Raman image bright features at the positions of the nanoparticles are observed. The intensity of these spots is strongly dependent on the excitation wavelength (Fig. 5.6 b-f): Whereas strong signals are detected for excitation wavelengths of 568nm and 633nm, much weaker intensities are observed for excitation wavelengths of 488nm, 514nm, and 647nm. In order to identify the origin of these bright features, a number of spectra were recorded on a specific nanoparticle ($\varnothing = 110nm$) using different wavelengths. Fig. 5.7 a shows the emission spectrum upon excitation with 488nm: A broad intensity distribution with 3 Lorentzians centered at 545, 609 and 696nm is observed. On top of this broad signal, two narrow Raman bands can be observed at 529nm (G-band, marked by an arrow) and 562.7nm (G*-band).

For larger excitation wavelengths (514, 568 and 633nm in spectrum b, c, and d), the respective Raman G-band is shifting towards higher wavelengths, while the broad Lorentzians do not change their positions. This is a clear indication that the background signal can be assigned to the fluorescence of the gold nanoparticles.
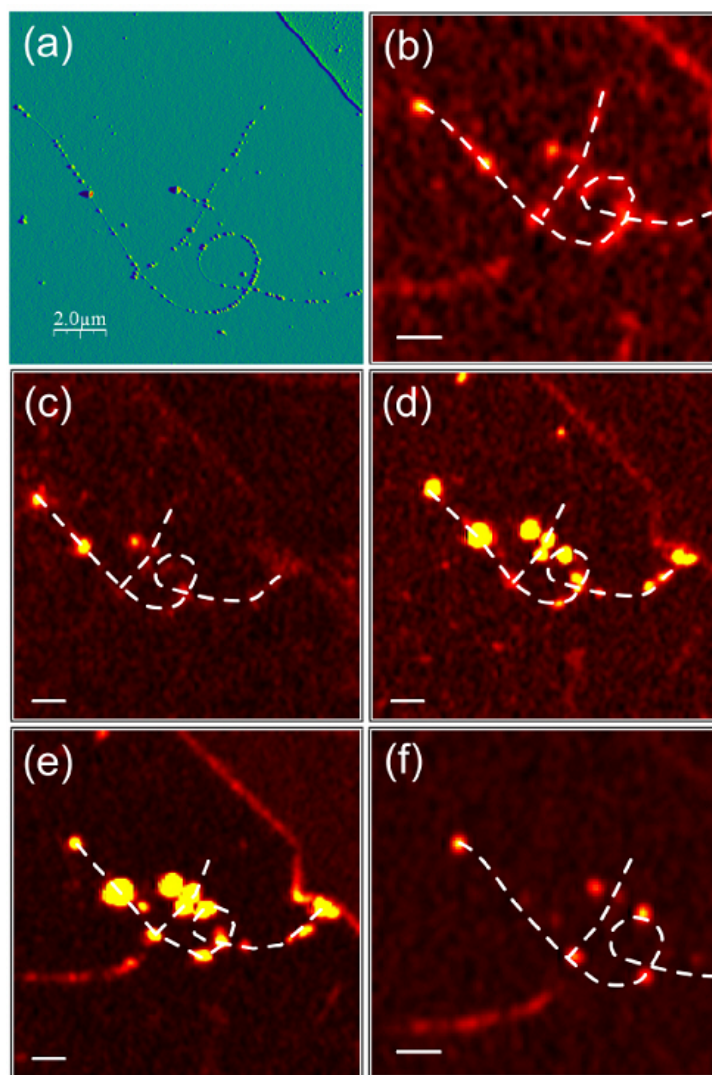

Figure 5.6: (a) AFM image and (b)-(f) G-band Raman imaging pictures of a nanoparticle-decorated nanotube at (b) 488nm, (c) 514nm, (d) 568nm, (e) 633nm and (f) 647nm.
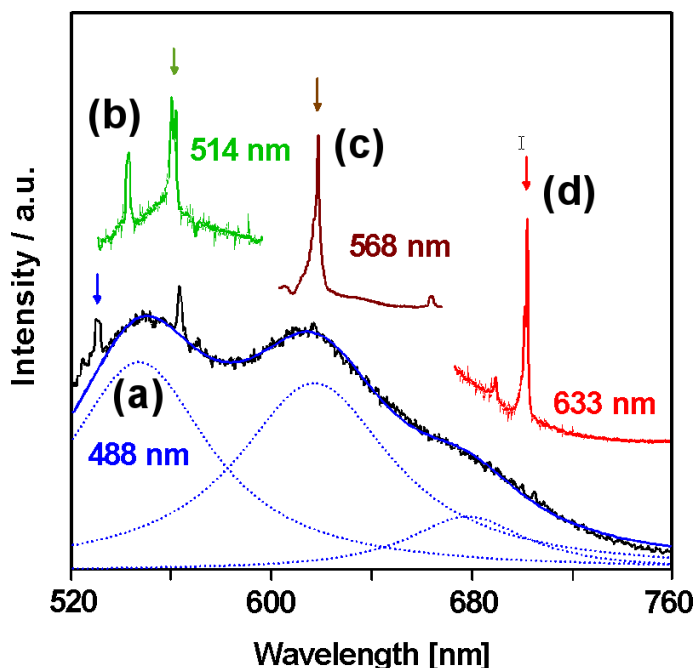
Figure 5.7: Experimentally observed superposition of fluorescence and Raman signal
for the following excitation wavelengths: (a) 488nm, (b) 514nm, (c) 568nm
and (d) 633nm. The Raman bands are shifting in wavelength.

Gold nanoparticles fluorescence is a three step process [84, 85, 86]:

- the **excitation** of an excited electron from an occupied d-band to an empty sp-band above the Fermi level upon light absorption.

- the **relaxation** of the electron in the sp-band to the Fermi level combined with a scattering of the holes in the d-band to a similar k-value as the electrons.

- the **recombination** of the electron-hole pair, which eventually results in photon emission.

The energy of the fluorescence photons should therefore be similar to the energetic separation between the Fermi-surface and the d-band at k-values, where the sp-band crosses the Fermi-surface. According to band structure calculations these crossing points are located close to the L- and X-symmetry points of the reciprocal space and the transitions should be observed at 639nm for the X-point and at 506nm for L-point, respectively [87]. Taking into account the width of the peaks this prediction agrees reasonably well with the experimental findings of 609nm for the X-point and 545nm

for the L-point. Although the shoulder appearing around 700nm cannot be assigned unambiguously, it has been tentatively attributed to intraband transitions or surface adsorbates in previous publications [88, 89].

While the energetic position of the fluorescence components remains largely unchanged for different particles, their relative intensity exhibits a strong size dependence. Fig. 5.8 displays a sequence of fluorescence spectra from several gold particles with different sizes on top of the carbon nanotubes upon excitation with 488nm. The relative intensity of the X-point transition increases with the size of the nanoparticles. This can be explained by a model, according to which the fluorescence is strongly enhanced if the transition energy is in resonance with the particle plasmon. Models based on local field enhancement predict, that the luminescence intensity is given by [85, 90]:

$$I \propto |E|^2 L(\omega_{\text{in}})^2 L(\omega_{\text{out}})^2 \beta \tag{5.3.1}$$

where E is the incident electromagnetic field, $L(\omega_{\text{in}})$ is the local-field factor at the incoming wavelength, $L(\omega_{\text{out}})$ is the local-field factor at the outgoing wavelength and β is a proportionality constant that includes the characteristic bulk gold fluorescence spectra. Therefore, there is a strong correlation between the frequency of the particle plasmon and the intensity of the fluorescence. For gold nanoparticles the plasmon absorption is very well described by Mie's theory, which shows that the absorption is broadening towards longer wavelength for increasing particle dimensions [91]. This will result in a stronger coupling with the long wavelength components of the intrinsic gold fluorescence and hence in an increase of the X-point fluorescence band.

5.4 Raman studies

Additionally to the observed fluorescence of the gold nanoparticles, an amplification of the carbon nanotube's Raman features is observed. The Raman amplification is due Surface-Enhanced Raman Scattering (SERS, see section 2.3.4 on page 23). It is noteworthy, that fluorescence and SERS are induced by the same nearfield and thus a strong Raman enhancement is always accompanied by a strong fluorescence. The surface-enhanced spectra can be classified into several subsets [92]:
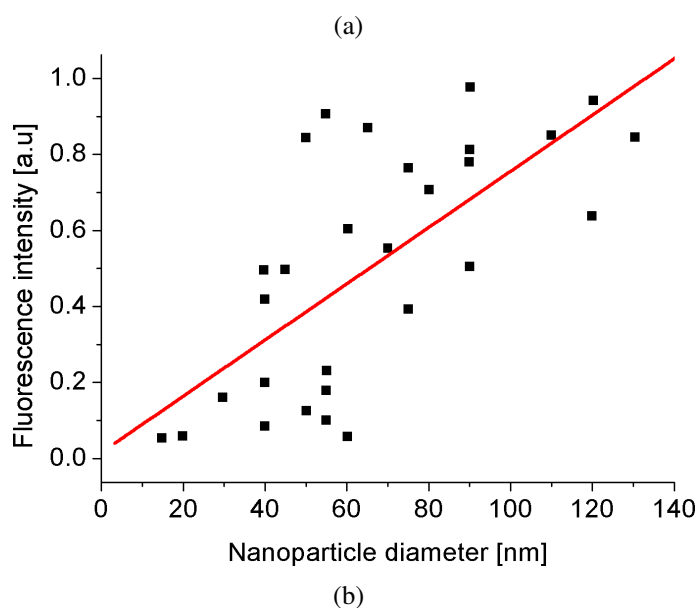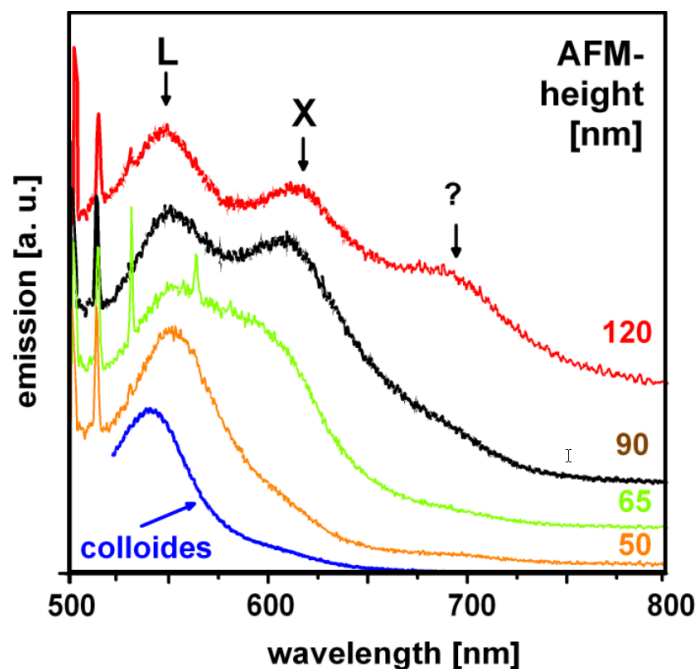
Figure 5.8: (a) Size dependence of the fluorescence for selected gold nanoparticles.
(b) X-band fluorescence intensity versus nanoparticle diameter. While the
intensities show a considerable variation, a fit (red line) shows a linear
intensity increase with the particle diameter.

- A tiny subset ($< 10\%$) comprises **significantly broadened Raman peaks** compared to the unmodified tubes (Fig. 5.9 a). Because fast spectral fluctuations on a millisecond range could be ruled out, the origin of this broadening might be due to the presence of amorphous carbon on the surface of the gold nanoparticle [93].

- Upon nanoparticle investigation with an excitation wavelength $> 600nm$, approximately (50%) of the spectra showed pronounced **spectral blinking** and spectral diffusion of the Raman bands. This phenomenon has frequently observed in previous SERS studies on small molecules and has been explained by local reorientations of the probed molecules [94]. However, for macromolecules like nanotubes a spontaneous rearrangement is very unlikely to take place. Additionally, since the fluctuations are rarely corresponding to normal nanotube Raman modes, the fluctuations are attributed to the presence of contaminants (e.g. coming from the electrochemical modification) acting like single molecules on the gold nanoparticle surface and emitting a surface-enhanced Raman signal (Fig. 5.9 b).

- The third subset if formed by the remaining spectra, which are stable in time, and display **well-defined Raman peaks** which closely resemble those of the pristine nanotubes, except for their intensity. The following investigation will focus on this subset exclusively.

5.4.1 Wavelength dependence of the surface enhancement

Two enhancement mechanisms have to be considered in order to explain the observed wavelength behaviour of the enhancement. Firstly, the Resonance Raman Effect occurs when the laser excitation energy matches the energy gap of two van Hove singularities (see section 2.3.2 on page 22).

Secondly the light absorption properties of the gold nanoparticles have to be considered. The absorption is broadened and shifted to higher wavelengths for larger nanoparticles. For the investigated nanoparticles ($\varnothing \approx 50nm$) the maximum absorption is at approximately 580nm citeSurface-Enhanced Raman Scattering:31Son2002.

Both enhancement mechanisms are operative simultaneously at certain wavelengths. The combination of RRS and the Surface-Enhanced Raman Scattering (SERS) is
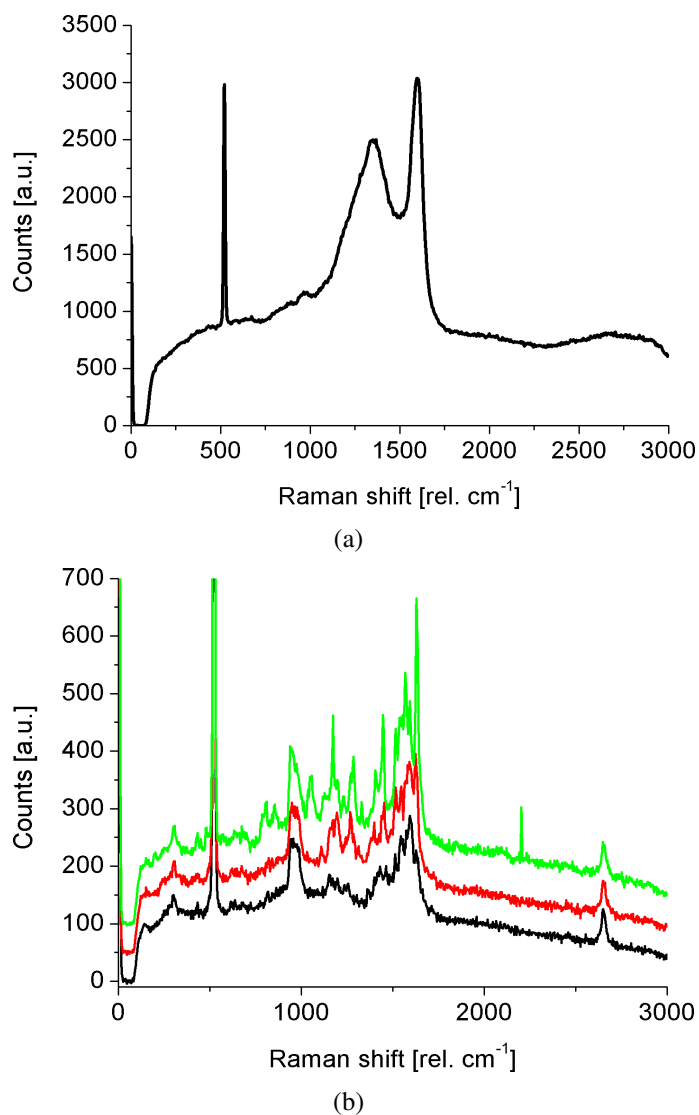
Figure 5.9: (a) Extreme broadening of D-band and G-band is observed for some emission spectra of a nanoparticle-decorated nanotube. For comparison, a normal resonance Raman spectrum can be found in Fig. 2.22 on page 30. (b) Three consecutive emission spectra ($\Delta t \approx 300ms$) on a nanoparticle with fluctuating emission. The spectra have been vertically offset for clarity.

referred to as Surface-Enhanced Resonance Raman Scattering (SERRS) [47]. From the
available laser wavelengths, the smallest deviations from the absorption maximum ($\approx$
580nm) is found for the 568nm line of an Argon-Krypton laser. Therefore, the biggest
SERRS enhancements are observed upon excitation with this wavelength. A detailed
analysis of the wavelength dependence can be found in table 5.1, which is based on an
analysis of the nanotube in Fig. 5.10.
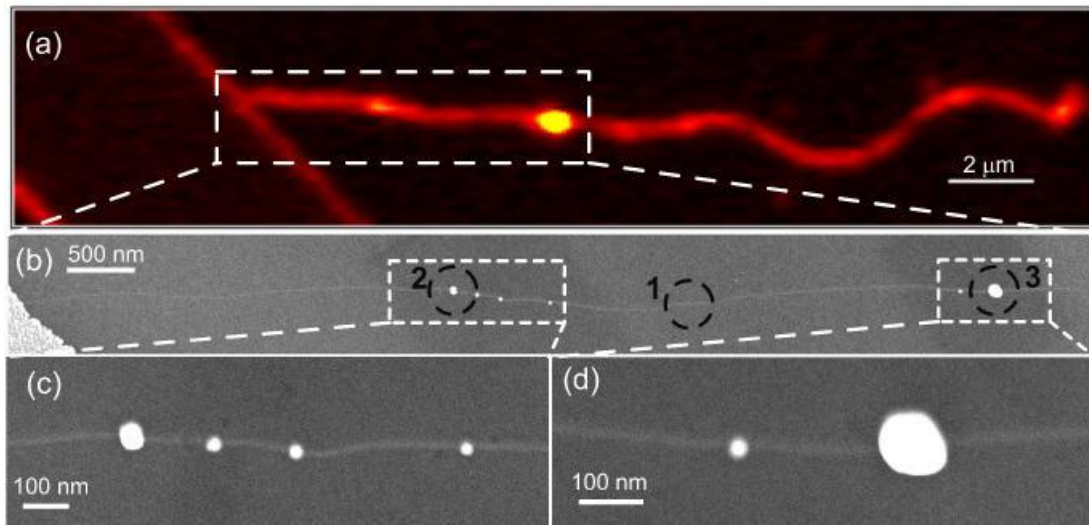
Figure 5.10: (a) G-band Raman imaging and (b)-(d) SEM images of a single nanotube
with electrochemically deposited gold clusters. The nanoparticle at posi-
tion 2 has a diameter of 35nm, the nanoparticle at position 3 has a diameter
of 70nm

Table 5.1: Table of the normalized enhancement factors from the positions denoted in
Fig. 5.10 for the main G-band component at $1590 cm^{-1}$.

Nanoparticle	Excitation wavelength			
	488nm	514nm	568nm	647nm
Pos. 1, unmodified	16.2	3.3	47.2	1
Pos.2, $\varnothing_{NP}$=35nm	20.5	4.3	90.1	1
Pos. 3 $\varnothing_{NP}$=70nm	20.5	2.3	739.5	36.6

5.4.2 Raman line positions in SERS spectra

In previous SERS studies on carbon nanotubes a number of interesting effect have been observed, including a Raman linewidth narrowing, Raman band position shift and changes in the relative band intensities. However, such effects have not been found in the present study, except for a disproportionate increase of the D-band, which has been observed in some cases, in agreement with the defect nucleation model. The absence of linewidth and band position changes indicate that only a small charge transfer between nanotube and nanoparticle is taking place. Additionally, as discussed in 2.3.4, linewidth and band position changes have previously been observed for large nanoparticle agglomerations, which give rise to hot spots with spectacular enhancements of up to 10^{14}, whereas for the present study individual nanoparticles with a maximum enhancement 10^5 were investigated. Hence, the absence of linewidth and band position changes might also be explained by the considerably lower enhancement factors. A summary of the observed linewidth and position shifts is given in table 5.2.

5.4.3 Polarization dependent Raman properties

In order to determine the symmetries of the underlying phonon modes (section 3.5.2 on page 53) polarization dependent Raman studies were performed [95]. So far, especially the A_1 symmetry of the RBM has only been indirectly determined experimentally by calculating the ratio $\bar{\alpha}^2/\gamma_s^2$ from the tensor invariants of the Raman tensor in backscattering configuration ($\bar{\alpha}^2$: isotropic part, γ_s^2: symmetric anisotropy) [96]. A direct verification of the symmetry has been hampered by the depolarization effect [97], which resulted in a sizable signal only if the polarization axis of the light coincided with the nanotube's orientation.

Owing to the high quality CVD samples, depolarization effects had only a minor influence on our measurements and thus the A_1 symmetry of the radial breathing mode could be verified in a direct experiment (Fig. 5.11). Previous VV/VH experiments on colloidal gold aggregates on top of carbon nanotubes have shown, that in this case it is not possible to directly extract the phonon symmetry from the polarization experiments [47]. Instead, a convolution of the phonon symmetry with the absorption properties of the gold nanoparticles is observed. In the previous study it was concluded

Table 5.2: Summary of the properties of the Raman bands for unmodified and gold decorated nanotubes. The positions are given in rel. cm^{-1}, the linewidths are given in nm.

|		RBM	D	G$^-$	G$^+$	G*	G$^+$/G$^-$	G$^+$/D	G*/D
NT 1	Position	242.7		1580.1	1593.1	2660.5	5.9		
unmodified	Linewidth	3.0		13.1	8.8	23.7			
NT 1 NP1	Δ Position	-3.1		-0.9	-0.1	0.4	5.3		
	Δ Linewidth	1.9		1.8	1.0	-1.3			
	Amplification	0.5		2.1	1.8	1.8			
NT 1 NP2	Δ Position	-6.0		-0.7	0.6	1.3	3.7		
	Δ Linewidth	1.2		6.8	2.9	1.5			
	Amplification	0.9		14.9	9.3	9.2			
NT 2	Position	159.5	1335.5	1572.4	1593.7	2670.9	5.8	53.8	1.7
unmodified	Linewidth	8.8	28.1	11.5	9.7	25.1			
NT 2 NP1	Δ Position	-1.3	-3.0	-3.2	-2.8	-5.7	4.6	18.2	0.5
	Δ Linewidth	4.7	1.2	1.6	1.4	-1.4			
	Amplification	11.1	16.5	7.1	5.6	4.9			
NT 3	Position	214.5		1574.9	1591.9	2671.7	6.1		
unmodified	Linewidth	4.9		11.3	10.0	40.7			
NT 3 NP1	Δ Position	-2.7			-2.5	-4.0			
	Δ Linewidth	2.6			2.9	-7.3			
	Amplification	20.0			28.5	39.1			
NT 3 NP2	Δ Position	-2.2		-3.5	-2.8	-2.8	12.8		
	Δ Linewidth	4.0		-0.3	0.1	0.6			
	Amplification	7.6		9.5	19.8	22.0			
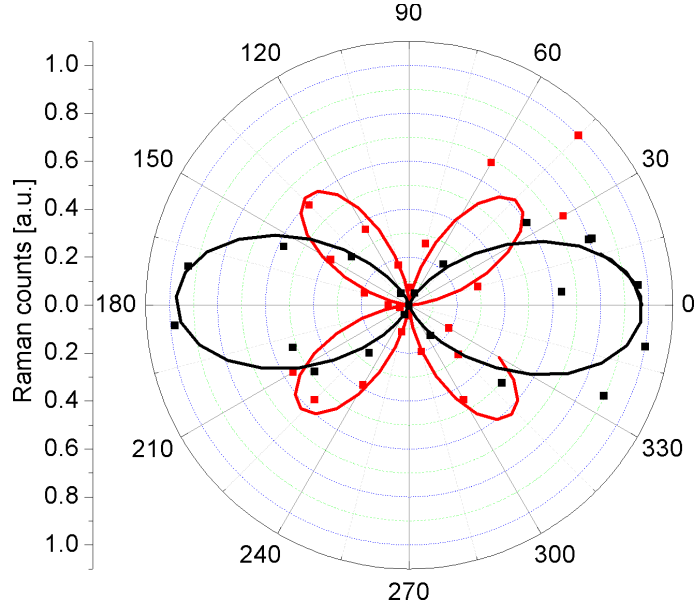
Figure 5.11: Normalized VV (black) and VH (red) angular dependence of the RBM amplitude on an bare nanotube. The curves are consistent with A_1 symmetry (see Fig. 3.16 on page 57).

that insight into the phonon symmetry can only be gained by avoiding the SERS technique altogether. However, as it turns out this argument is not true for individual nanoparticles: pIn Fig. 5.12, the Raman spectrum collected over an isolated nanoparticle (size $\sim 40nm$) on top of a SWCNT is displayed. Based upon Kataura's plot [23, 30], the measured RBM position $\omega_{RBM} = 161cm^{-1}$ and the used excitation wavelength ($\lambda_{exc} = 568nm$), this SWCNT is tentatively assigned to the semiconducting (15,7) tube. The presence of a semiconducting tube is corroborated by the absence of a BWF resonance within the G-band, and the observation that nanotubes with $v = (n - m)$ mod $3 = -1$ have a higher Raman cross section than other tubes [30]. Compared to the bare segment on the same tube, the presence of the nanoparticle causes an increase of the RBM and G-band intensity by a factor of ~ 4. In order to compare this to enhancement factors for molecules as reported in the literature [43, 44] it has to be taken into account that the local electromagnetic field from surface plasmons decays very rapidly from the nanoparticle surface. Accordingly, the Raman signal is only enhanced for molecules in the range of just a few nm from the particle surface. Assuming that only a few % of the CNT within the diffraction limited laser spot ($d \approx 500nm$) is enhanced by the nanoparticle, the local enhancement would be 2-3 orders of magnitude, consistent with theory [98].
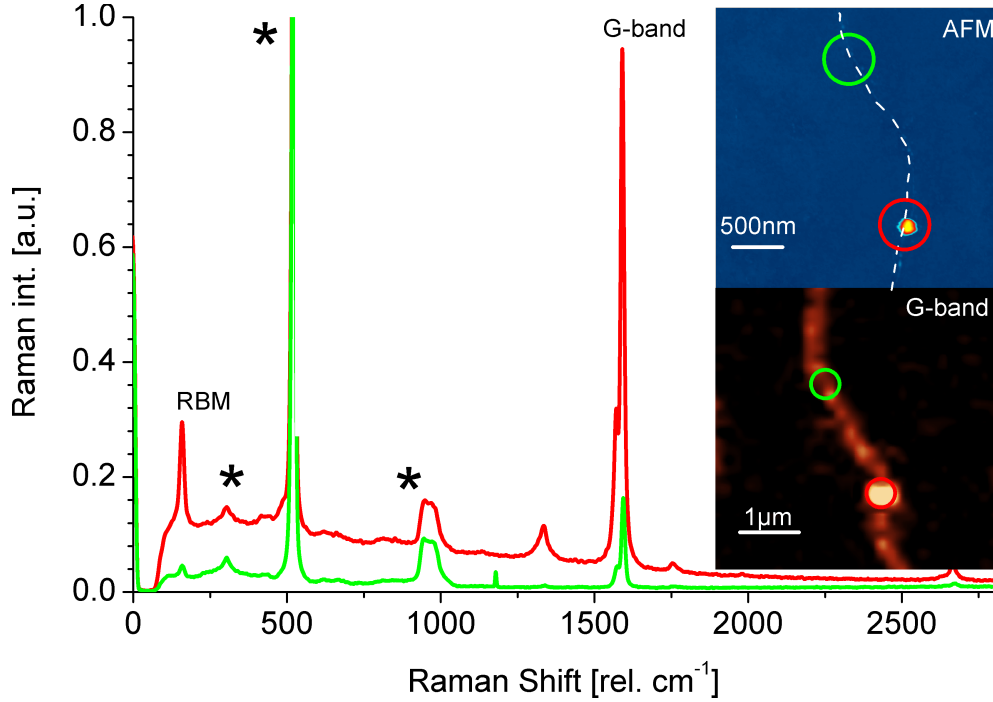
Figure 5.12: Raman spectra recorded at two different positions along a SWNT (NT1). Comparison between the spectra taken on the bare tube (green line) and over a gold particle deposited onto the tube (red line) reveals an enhancement of the G-band and RBM by a factor of ~ 4. Substrate peaks are labeled by *. The insets show an AFM and a Raman G-band image of the investigated tube with two circles denoting the positions at which the spectra were taken. By AFM cross-sectional analysis, the size of the particle was determined to be $\sim 40nm$. The location of the nanotube has been highlighted by a dashed line in the AFM image.

Raman spectra acquired from another SWCNT, decorated with a small agglomeration of gold nanoparticles, are presented in Fig. 5.13. Using Kataura's plot from [23, 30], the measured RBM position $\omega_{RBM} = 221cm^{-1}$ and $\lambda_{exc} = 568nm$, this SWCNT is assigned to the metallic (13,1) tube. The broadened G-band displayed by this nanotube is indicative of a BWF resonance, and consistent with its metallic character. For this tube, the Raman intensity increase is found to be approximately three orders of magnitude upon particle decoration. Several other SWCNTs decorated by nanoparticle agglomerates of similar size yielded enhancement factors ranging between one and four orders of magnitude, independently of the electronic properties of the tubes. This observation is in accord with the existence of enhanced electromagnetic fields inside cavities formed between nanoparticles with a separation of the order of a few nanometers
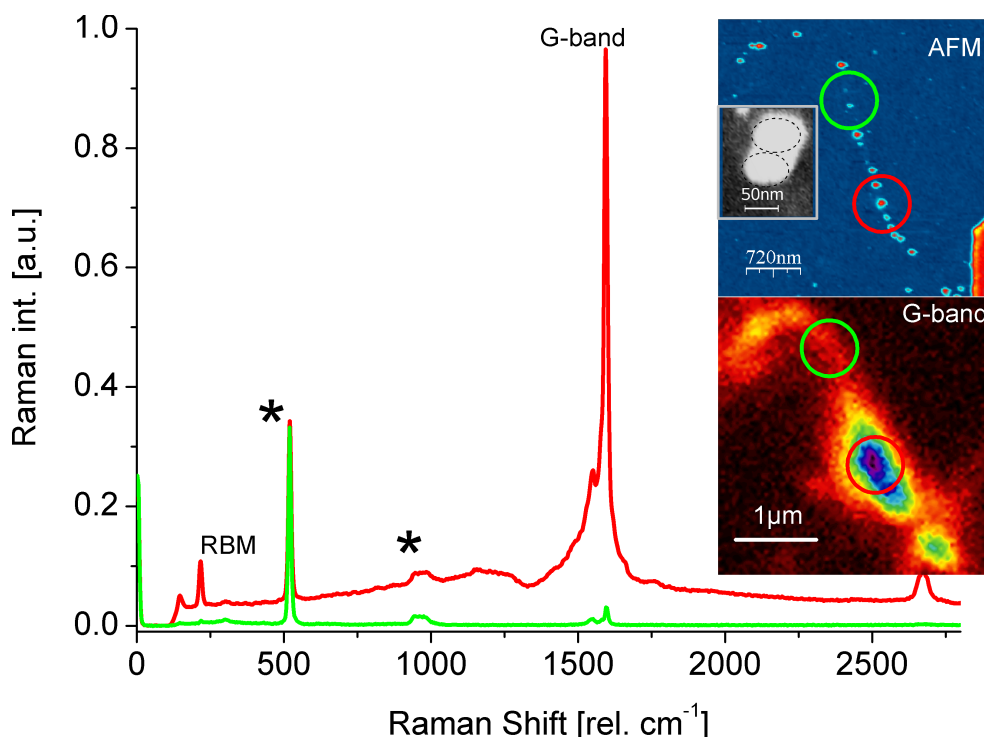
Figure 5.13: Raman spectra of a second SWCNT (NT2), acquired on a bare tube section (green line) and above an agglomeration of several gold nanoparticles (red line). Substrate peaks are labeled by *. In the enhanced spectrum, the G-band and RBM appear with two orders of magnitude increased intensity. The insets show an AFM and a Raman G-band image of the investigated tube with two circles denoting the positions at which the spectra were taken. The AFM image contains a SEM inset of the particle agglomeration.

[99]. For instance, from electromagnetic theories it is predicted that the enhancement factors in the centre of particle dimers with an interparticle distance of just a few nm can be orders of magnitudes higher than at the surface of individual particles, albeit they are also very sensitive to the geometry of the aggregate [98].

The number and arrangement of the nanoparticles on the tubes exerted a profound influence on the Raman response, as apparent from Fig. 5.14 which plots the polarization angle dependence of RBM and G-band (maximum intensity component at $1590 cm^{-1}$) for the SWCNTs of figures 5.12 and 5.13. It is noteworthy that the other components of the G-band (at $1570 cm^{-1}$ and $1550 cm^{-1}$) showed similar behaviour as the $1590 cm^{-1}$ component. First, NT1 bearing an isolated nanoparticle is addressed. The data gained in (V-) configuration (Fig. 5.14a,b) provide evidence, that the tube absorbs most strongly
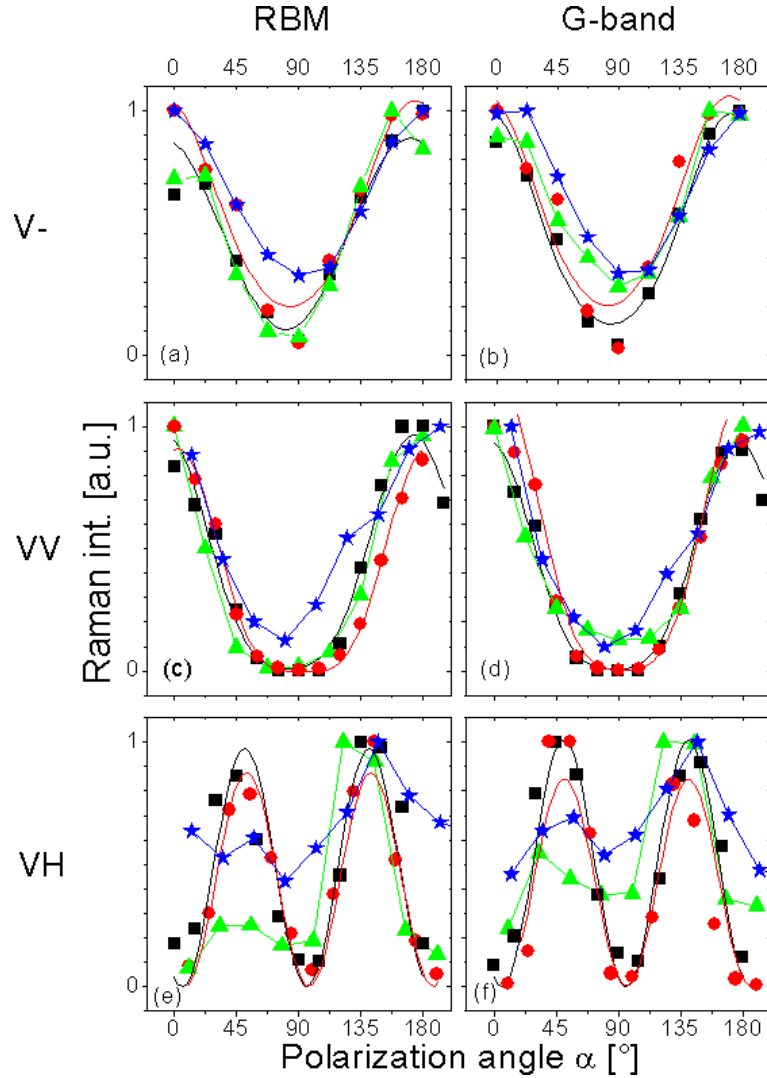
Figure 5.14: Normalized polarization dependence of the RBM and G-band intensity measured on NT1 ($\omega_{RBM} = 161 cm^{-1}$) and NT2 ($\omega_{RBM} = 221 cm^{-1}$). In case of NT1, the bare tube (black ■) is compared with a section modified by a single gold nanoparticle (red ●). The NT2 spectra were acquired above two different gold nanoparticle agglomerations (green ▲ and blue ★) on the nanotube, which differ in the geometrical arrangement of the particles. For NT1 (black and red), the solid lines are fits to the models mentioned in the text, whereas for NT2 (green and blue) a straight connection of the data points is presented, since there is no model available.

when the polarization vector of the incoming light is parallel to be tube axis, independent of the presence of the nanoparticle. This finding reflects the well-documented antenna effect of CNTs [100].

In the (VV) configuration (Fig. 5.14c,d), the bare NT1 displays a $\cos(\alpha)^4$ dependence of the Raman intensity, as expected from theory. Similar agreement with theory exists in case of the (VH) configuration, for which a $\cos(\alpha)^2 \sin(\alpha)^2$ dependence is observed (Fig. 5.14e,f). Essentially the same dependencies can be discerned over the nanoparticle, despite the 40-fold Raman enhancement that it generates. Such a negligible influence on the polarization dependence was found for all investigated isolated nanoparticles on different SWCNTs. This observation demonstrates, that the single particle induces an isotropic SERS effect with the field component along the tube axis enhancing the absorption and hence the Raman cross-section of the tube. In contrast, for the two different nanoparticle agglomerations on NT2, a clear tendency to absorb light also when the polarization is perpendicular to the tube axis can be seen in the (V-) (Fig. 5.14a,b) and (VV) configurations (Fig. 5.14c,d), i.e., the Raman intensity does not approach zero for $\alpha = 90°$.

Even more pronounced differences are apparent from the data collected in the (VH) configuration, as manifested by a pronounced flattening of the angular dependence for both agglomerates (Fig. 5.14e,f). Especially the second aggregate (blue stars) displays an almost complete loss of the characteristic angular dependence. This behaviour indicates, that the measured polarization dependence is predominantly dictated by the electromagnetic enhancement governed by the geometry of the nanoparticle agglomerates. In fact, gold nanoparticle agglomerates such as the present ones can have a complex electromagnetic near-field distribution with a strong preferential orientation as well as only a tiny angular dependence [101].

5.5 Comparison to colloidal gold particles

In order to compare the optical properties of the electrochemically grown gold nanoparticles with commercially available gold colloids ($\varnothing \approx 60nm$) [102], the latter were deposited on a SiO_2 surface covered with carbon nanotubes. On the surface, the colloids tend to form agglomerations instead of individual nanoparticles (see Fig. 5.15).

While the colloids displayed an optically similar emission as the electrochemically grown nanoparticles (see Fig. 5.8), no clear surface enhancement effect could be observed for the colloidal particles. The reason for the absence of SERS in this case might be the nanoparticle to nanotube distance: While for the electrochemically grown nanoparticles direct contact to the nanotube is ensured due to the growth conditions, the nanotubes might not be within the optical nearfield of the weakly physisorbed colloidal gold nanoparticles.
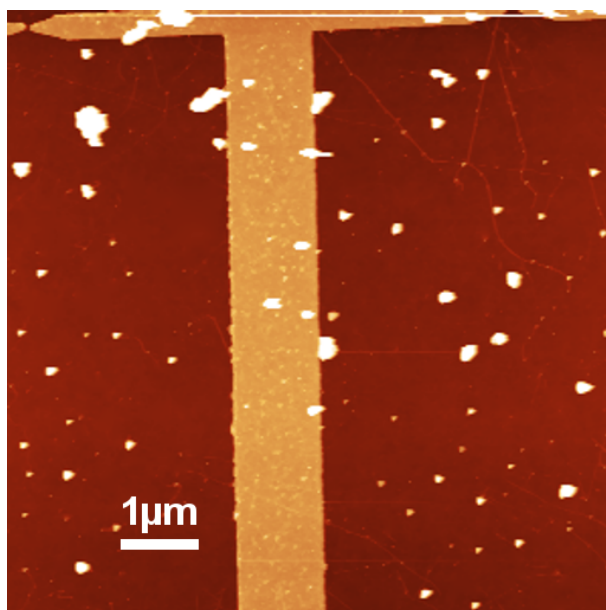

Figure 5.15: AFM image of individual and agglomerated colloidal gold nanoparticles ($\varnothing \approx 60nm$) on a SiO$_2$ sample with contacted nanotubes.

6 Summary and Conclusion

In this thesis, functionalization strategies of carbon nanotubes with organic dye molecules and metal nanoparticles have been investigated. While the former approach was directed towards photoinduced switching of the nanotube's electrical conductivity, the latter focused on changes in the nanotube's Raman spectrum induced by the metal nanoparticles upon laser illumination.

The possibility to detect electrical charge transfer between a nanotube and a noncovalently linked molecule has been investigated by electrical transport measurement using strong organic donor and acceptor molecules (TTF/TCNQ). Indeed, the conductivity was decreased for the donor molecule, while it was increased for the acceptor molecule. Based on these results, an optoelectronic conductivity switch was envisioned from molecules, which were photoswitchable between two conformations: Whereas in one conformation the molecule would noncovalently bind to the nanotube and donate or accept electrons, in the other conformation no bond would be formed due to steric hindrance. However, either the molecular interaction was too weak to result in a detectable conductivity change (bisanthracene switch), or the effect vas veiled by the strong conductivity change induced by the accompanying azopyridine (Zn-porphyrin switch). In the case of Sudan Red B, a pronounced switching of the conductivity could be observed, however, due to the low reproducibility it was not possible to unambiguously interpret the experiments.

Covalently attached molecules were used as a second approach in order to optically switch the nanotube's conductivity: In the case of the pentacene derivative, the extreme oxygen sensitivity did not allow to draw clear conclusions. Even when stabilized in a tris buffer solution, no sign for the formation of covalent links between nanotube and pentacene could be detected. In contrast to this, acridine diazonium salt and a Ru-based diazonium salt gave clear proofs, that covalent bonds were created, since an increase in

the Raman D-band, a decrease of conductivity and a height increase of the nanotube structure in the AFM images were observed. Despite this, both diazonium salts did not induce a sizable photoswichting of the nanotube's conductivity, which might be due to a polymerization effect that destroys the chromophores. Additionally, during the experiments it was found, that a sizable conductivity switch could be realized by simply illuminating a bare semiconducting nanotube with UV light under ambient conditions.

Concluding the photoswitching project, it has been demonstrated, that by illuminating functionalized nanotubes with visible light, the tube's electrical conductivity can be reversibly switched by over one order of magnitude. However, the experiments also show, that full control of the experimental parameters is needed in order to gain reproducible switching properties. Since the development of a reliable optoelectronic switch based on carbon nanotubes remains an attractive task, a main aspect of future research in this area should target reproducible conditions.

The properties of gold, silver and palladium nanoparticles, electrodeposited onto carbon nanotubes were studied. Since the silver nanoparticles rapidly oxidized and no sufficient control on the decoration density of the palladium nanoparticles could be achieved, the experiments were focused on the analysis of gold nanoparticles. While the functionalization with gold nanoparticles resulted in very changes of the nanotube's electrical conductivity, the nanotube-nanoparticle system exhibited a number of interesting optical effects when illuminated with a laser: The nanoparticles were luminescent; the L and X symmetry points of the inverse gold lattice could be identified as the origin of the luminescence. Furthermore, in the vicinity of the nanoparticles, a pronounced enhancement of the nanotube's Raman bands induced by the surface plasmon of the nanoparticle was observed (Surface-enhanced Raman scattering, SERS). The SERS enhancement was strongly dependent on the excitation laser wavelength, being maximal when the wavelength coincided with the maximum absorption wavelength of the nanoparticles.

The excellent control on nanoparticle density and size allowed for the first time to study the SERS effect at the individual nanotube - individual nanoparticle level. Unlike previous investigations in more complex systems, which concluded, that the symmetry of the phonon modes responsible for the Raman signal cannot be determined by SERS due to a convolution with the angular intensity dependence of the surface plasmons, it was shown in this study, that an individual nanoparticle creates an isotropic enhancement

and thus, the symmetry of the phonons remains accessible. On the contrary, already a dimer of nanoparticles destroys the isotropic enhancement effect.

Concluding the metal nanoparticle electrodeposition experiments, the newly developed nanoparticle-nanotube system for the first time allowed studying the SERS effect at its most fundamental level: A single molecule in the nearfield of a single nanoparticle. Important insights into the SERS enhancement process could be obtained. Furthermore, the discovery of an isotropic SERS enhancement for individual nanoparticles allowed for a determination of the symmetry of the underlying vibrations also under SERS enhancement conditions. Since the SERS effect is widely used for spectroscopic analysis of molecules, this extension of the SERS applicability can most likely be used for many spectroscopic studies to gain new insights into single molecules.

Bibliography

[1] D. Harden. The glass of the caesars. *The British Museum Press*, (139): 245, 1988.

[2] M. Reibold, P. Paufler, A. A. Levin, W. Kochmann, N. Patzke, and D. C. Meyer. Materials - carbon nanotubes in an ancient damascus sabre. *Nature*, 444(7117): 286–86, 2006.

[3] R. P. Feynman. There's plenty of room at the bottom. *Engineering and Science Magazine*, 23(5), 1960.

[4] G. Binnig, H. Rohrer, C. Gerber, and E. Weibel. Tunneling through a controllable vacuum gap. *Appl. Phys. Lett.*, 40(2): 178–80, 1982.

[5] S. Iijima and T. Ichihashi. Single-shell carbon nanotubes of 1-nm diameter. *Nature*, 363(6430): 603–05, 1993.

[6] http://en.wikipedia.org *Wikipedia*, 2007.

[7] H. W. Kroto, J. R. Heath, S. C. Obrien, R. F. Curl, and R. E. Smalley. C-60 - buckminsterfullerene. *Nature*, 318(6042): 162–63, 1985.

[8] M. Monthioux and V. L. Kuznetsov. Who should be given the credit for the discovery of carbon nanotubes? *Carbon*, 44(9): 1621–23, 2006.

[9] L. Radushkevich and V. Lukyanovich. O strukture ugleroda, obrazujucegosja pri termiceskom razlozenii okisi ugleroda na zeleznom kontakte. *Zurn Fisic Chim*, 26:88–95, 1952.

[10] A. Oberlin, M. Endo, and T. Koyama. Filamentous growth of carbon through benzene decomposition. *J. Cryst. Growth*, 32(3): 335–49, 1976.

[11] A. Krishnan, E. Dujardin, T. W. Ebbesen, P. N. Yianilos, and M. M. J. Treacy. Young's modulus of single-walled nanotubes. *Phys. Rev. B*, 58(20): 14013–19, 1998.

[12] B. G. Demczyk, Y. M. Wang, J. Cumings, M. Hetman, W. Han, A. Zettl, and

R. O. Ritchie. Direct mechanical measurement of the tensile strength and elastic modulus of multiwalled carbon nanotubes. *Materials Science And Engineering A-Structural Materials Properties Microstructure And Processing*, 334(1-2): 173–78, 2002.

[13] B. Q. Wei, R. Vajtai, and P. M. Ajayan. Reliability and current carrying capacity of carbon nanotubes. *Appl. Phys. Lett.*, 79(8): 1172–74, 2001.

[14] T. Durkop, S. A. Getty, E. Cobas, and M. S. Fuhrer. Extraordinary mobility in semiconducting carbon nanotubes. *Nano Letters*, 4(1): 35–39, 2004.

[15] H. W. Zhu, C. L. Xu, D. H. Wu, B. Q. Wei, R. Vajtai, and P. M. Ajayan. Direct synthesis of long single-walled carbon nanotube strands. *Science*, 296(5569): 884–86, 2002.

[16] L. X. Zheng, M. J. O'Connell, S. K. Doorn, X. Z. Liao, Y. H. Zhao, E. A. Akhadov, M. A. Hoffbauer, B. J. Roop, Q. X. Jia, R. C. Dye, D. E. Peterson, S. M. Huang, J. Liu, and Y. T. Zhu. Ultralong single-wall carbon nanotubes. *Nature Materials*, 3(10): 673–76, 2004.

[17] J. Kurti, V. Zolyomi, M. Kertesz, G. Sun, R. H. Baughman, and H. Kuzmany. Individualities and average behavior in the physical properties of small diameter single-walled carbon nanotubes. *Carbon*, 42(5-6): 971–78, 2004.

[18] R. Saito, M. Fujita, G. Dresselhaus, and M. S. Dresselhaus. Electronic-structure of chiral graphene tubules. *Appl. Phys. Lett.*, 60(18): 2204–06, 1992.

[19] R. Saito, M. Fujita, G. Dresselhaus, and M. S. Dresselhaus. Electronic-structure of graphene tubules based on c-60. *Phys. Rev. B*, 46(3): 1804–11, 1992.

[20] R. Saito, G. Dresselhaus, and M. S. Dresselhaus. *Physical Properties of Carbon Nanotubes*. Imperial College Press: London. 1998.

[21] N. W. Ashcroft and N. D. Mermin. Solid state physics. *Saunders College Publishing*, 1976.

[22] L. Van Hove. The occurrence of singularities in the elastic frequency distribution of a crystal. *Physical Review*, 89(6): 1189–93, 1953.

[23] H. Kataura, Y. Kumazawa, Y. Maniwa, I. Umezu, S. Suzuki, Y. Ohtsuka, and Y. Achiba. Optical properties of single-wall carbon nanotubes. *Synth. Met.*, 103(1-3): 2555–58, 1999.

[24] J. W. Mintmire, B. I. Dunlap, and C. T. White. Are fullerene tubules metallic. *Phys. Rev. Lett.*, 68(5): 631–34, 1992.

[25] J. W. Mintmire, D. H. Robertson, and C. T. White. Properties of fullerene nanotubules. *J. Phys. Chem. Solids*, 54(12): 1835–40, 1993.

[26] M. S. Dresselhaus and P. C. Eklund. Phonons in carbon nanotubes. *Advances In Physics*, 49(6): 705–814, 2000.

[27] C. V. Raman. A change of wave-length in light scattering. *Nature*, 121:619–19, 1928.

[28] C. V. Raman and K. S. Krishnan. A new type of secondary radiation. *Nature*, 121:501–02, 1928.

[29] D. G. Rea. On the theory of the resonance raman effect. *J. Mol. Spectrosc.*, 4(6): 499–506, 1960.

[30] C. Thomsen, H. Telg, J. Maultzsch, and S. Reich. Chirality assignments in carbon nanotubes based on resonant raman scattering. *Physica Status Solidi B-Basic Solid State Physics*, 242(9): 1802–06, 2005.

[31] J. Maultzsch, H. Telg, S. Reich, and C. Thomsen. Radial breathing mode of single-walled carbon nanotubes: Optical transition energies and chiral-index assignment. *Phys. Rev. B*, 72(20), 2005.

[32] M. Fleischman, P. J. Hendra, and AJ. McQuilla. Raman-spectra of pyridine adsorbed at a silver electrode. *Chem. Phys. Lett.*, 26(2): 163–66, 1974.

[33] D. L. Jeanmaire and R. P. Vanduyne. Surface raman spectroelectrochemistry.1. heterocyclic, aromatic, and aliphatic-amines adsorbed on anodized silver electrode. *Journal Of Electroanalytical Chemistry*, 84(1): 1–20, 1977.

[34] M. G. Albrecht and J. A. Creighton. Anomalously intense raman-spectra of pyridine at a silver electrode. *J. Am. Chem. Soc.*, 99(15): 5215–17, 1977.

[35] M. Moskovits. Surface-enhanced spectroscopy. *Rev. Mod. Phys.*, 57(3): 783–826, 1985.

[36] A. Campion and P. Kambhampati. Surface-enhanced raman scattering. *Chem. Soc. Rev.*, 27(4): 241–50, 1998.

[37] G. C. Schatz, M. A. Young, and R. P. Van Duyne. Electromagnetic mechanism of SERS. In *Surface-Enhanced Raman Scattering: Physics And Applications*, volume 103 of *Topics In Applied Physics*, pages 19–45. 2006.

[38] http://plasmonicfocus.googlepages.com , 2007.

[39] E. Hao and G. C. Schatz. Electromagnetic fields around silver nanoparticles and

dimers. *J. Chem. Phys.*, 120(1): 357–66, 2004.

[40] K. Kneipp and H. Kneipp. Single molecule raman scattering. *Appl. Spectrosc.*, 60(12): 322A–34A, 2006.

[41] A. Otto. The 'chemical' (electronic) contribution to surface-enhanced raman scattering. *J. Raman Spectrosc.*, 36(6-7): 497–509, 2005.

[42] A. Otto. Theory of first layer and single molecule surface enhanced raman scattering (SERS). *Physica Status Solidi A-Applied Research*, 188(4): 1455–70, 2001.

[43] S. M. Nie and S. R. Emery. Probing single molecules and single nanoparticles by surface-enhanced raman scattering. *Science*, 275(5303): 1102–06, 1997.

[44] K. Kneipp, Y. Wang, H. Kneipp, L. T. Perelman, I. Itzkan, R. Dasari, and M. S. Feld. Single molecule detection using surface-enhanced Raman scattering (SERS). *Phys. Rev. Lett.*, 78(9): 1667–70, 1997.

[45] M. Moskovits, L. L. Tay, J. Yang, and T. Haslett. SERS and the single molecule. In *Optical Properties Of Nanostructured Random Media*, volume 82 of *Topics In Applied Physics*, pages 215–26. 2002.

[46] K. Kneipp, H. Kneipp, and H. G. Bohr. Single-molecule SERS spectroscopy. In *Surface-Enhanced Raman Scattering: Physics And Applications*, volume 103 of *Topics In Applied Physics*, pages 261–77. 2006.

[47] K. Kneipp, A. Jorio, H. Kneipp, S. D. M. Brown, K. Shafer, J. Motz, R. Saito, G. Dresselhaus, and M. S. Dresselhaus. Polarization effects in surface-enhanced resonant Raman scattering of single-wall carbon nanotubes on colloidal silver clusters. *Phys. Rev. B*, 6308(8), 2001.

[48] K. Kneipp, L. T. Perelman, H. Kneipp, V. Backman, A. Jorio, G. Dresselhaus, and M. S. Dresselhaus. Coupling and scattering power exchange between phonon modes observed in surface-enhanced Raman spectra of single-wall carbon nanotubes on silver colloidal clusters. *Phys. Rev. B*, 63(19), 2001.

[49] A. Jorio, M. A. Pimenta, C. Fantini, M. Souza, A. G. Souza, G. G. Samsonidze, G. Dresselhaus, M. S. Dresselhaus, and R. Saito. Advances in single nanotube spectroscopy: Raman spectra from cross-polarized light and chirality dependence of Raman frequencies. *Carbon*, 42(5-6): 1067–69, 2004.

[50] R. C. Maher, L. F. Cohen, P. Etchegoin, H. J. N. Hartigan, R. J. C. Brown, and M. J. T. Milton. Stokes/anti-stokes anomalies under surface enhanced Raman scattering conditions. *J. Chem. Phys.*, 120(24): 11746–53, 2004.

[51] S. M. Bachilo, M. S. Strano, C. Kittrell, R. H. Hauge, R. E. Smalley, and R. B. Weisman. Structure-assigned optical spectra of single-walled carbon nanotubes. *Science*, 298(5602): 2361–66, 2002.

[52] A. Hamwi, H. Alvergnat, S. Bonnamy, and F. Beguin. Fluorination of carbon nanotubes. *Carbon*, 35(6): 723–28, 1997.

[53] E. Unger, A. Graham, F. Kreupl, M. Liebau, and W. Hoenlein. Electrochemical functionalization of multi-walled carbon nanotubes for solvation and purification. *Current Applied Physics*, 2(2): 107–11, 2002.

[54] B. Khare, M. Meyyappan, M. H. Moore, P. Wilhite, H. Imanaka, and B. Chen. Proton irradiation of carbon nanotubes. *Nano Letters*, 3(5): 643–46, 2003.

[55] Y. Chen, R. C. Haddon, S. Fang, A. M. Rao, W. H. Lee, E. C. Dickey, E. A. Grulke, J. C. Pendergrass, A. Chavan, B. E. Haley, and R. E. Smalley. Chemical attachment of organic functional groups to single-walled carbon nanotube material. *J. Mater. Res.*, 13(9): 2423–31, 1998.

[56] S. Banerjee and S. S. Wong. Rational sidewall functionalization and purification of single-walled carbon nanotubes by solution-phase ozonolysis. *J. Phys. Chem. B*, 106(47): 12144–51, 2002.

[57] A. Koshio, M. Yudasaka, M. Zhang, and S. Iijima. A simple way to chemically react single-wall carbon nanotubes with organic materials using ultrasonication. *Nano Letters*, 1(7): 361–63, 2001.

[58] Z. J. Jia, Z. Y. Wang, C. L. Xu, J. Liang, B. Q. Wei, D. H. Wu, and S. W. Zhu. Study on poly(methyl methacrylate)/carbon nanotube composites. *Materials Science And Engineering A-Structural Materials Properties Microstructure And Processing*, 271(1-2): 395–400, 1999.

[59] K. BalasubRamanian, M. Friedrich, C. Y. Jiang, Y. W. Fan, A. Mews, M. Burghard, and K. Kern. Electrical transport and confocal Raman studies of electrochemically modified individual carbon nanotubes. *Adv. Mater.*, 15(18): 1515–+, 2003.

[60] J. L. Bahr and J. M. Tour. Covalent chemistry of single-wall carbon nanotubes. *J. Mater. Chem.*, 12(7): 1952–58, 2002.

[61] H. Hu, P. Bhowmik, B. Zhao, M. A. Hamon, M. E. Itkis, and R. C. Haddon. Determination of the acidic sites of purified single-walled carbon nanotubes by acid-base titration. *Chem. Phys. Lett.*, 345(1-2): 25–28, 2001.

[62] A. C. Dillon, K. M. Jones, T. A. Bekkedahl, C. H. Kiang, D. S. Bethune, and

M. J. Heben. Storage of hydrogen in single-walled carbon nanotubes. *Nature*, 386(6623): 377–79, 1997.

[63] M. Muris, N. Dupont-Pavlovsky, M. Bienfait, and P. Zeppenfeld. Where are the molecules adsorbed on single-walled nanotubes? *Surf. Sci.*, 492(1-2): 67–74, 2001.

[64] H. Ulbricht, G. Moos, and T. Hertel. Physisorption of molecular oxygen on single-wall carbon nanotube bundles and graphite. *Phys. Rev. B*, 66(7), 2002.

[65] P. M. Ajayan, O. Stephan, C. Colliex, and D. Trauth. Aligned carbon nanotube arrays formed by cutting a polymer resin-nanotube composite. *Science*, 265(5176): 1212–14, 1994.

[66] M. L. de la Chapelle, C. Stephan, T. P. Nguyen, S. Lefrant, C. Journet, P. Bernier, E. Munoz, A. Benito, W. K. Maser, M. T. Martinez, G. F. de la Fuente, T. Guillard, G. Flamant, L. Alvarez, and D. Laplaze. Raman characterization of singlewalled carbon nanotubes and PMMA-nanotubes composites. *Synth. Met.*, 103(1-3): 2510–12, 1999.

[67] J. Oh, S. Roh, W. Yi, H. Lee, and J. Yoo. Conductivity change of carbon nanotube with strong electron-donating and withdrawing molecules. *Journal of Vacuum Science and Technology B*, 22(3): 1416–19, 2004.

[68] M. J. O'Connell, S. M. Bachilo, C. B. Huffman, V. C. Moore, M. S. Strano, E. H. Haroz, K. L. Rialon, P. J. Boul, W. H. Noon, C. Kittrell, J. P. Ma, R. H. Hauge, R. B. Weisman, and R. E. Smalley. Band gap fluorescence from individual single-walled carbon nanotubes. *Science*, 297(5581): 593–96, 2002.

[69] X. F. Guo, L. M. Huang, S. O'Brien, P. Kim, and C. Nuckolls. Directing and sensing changes in molecular conformation on individual carbon nanotube field effect transistors. *J. Am. Chem. Soc.*, 127(43): 15045–47, 2005.

[70] J. M. Simmons, I. In, V. E. Campbell, T. J. Mark, F. Léonard, P. Gopalan, and M. A. Eriksson. Optically modulated coduction in chromophore-functionalized single-wall carbon nanotubes. *Phys. Rev. Lett.*, 98(08): 086802, 2007.

[71] J. B. Cui, M. Burghard, and K. Kern. Reversible sidewall osmylation of individual carbon nanotubes. *Nano Letters*, 3(5): 613–15, 2003.

[72] G. Binnig, C. F. Quate, and C. Gerber. Atomic force microscope. *Phys. Rev. Lett.*, 56(9): 930–33, 1986.

[73] F. Koberling. *PhD thesis: Fluoreszenzmikroskopische Untersuchungen an einzelnen Halbleiter-Nanokristallen, Verlag Dr. Hut, München*, 2001.

[74] H. P. Li, B. Zhou, Y. Lin, L. R. Gu, W. Wang, K. A. S. Fernando, S. Kumar, L. F. Allard, and Y. P. Sun. Selective interactions of porphyrins with semiconducting single-walled carbon nanotubes. *J. Am. Chem. Soc.*, 126(4): 1014–15, 2004.

[75] J. Otsuki, A. Yasuda, and T. Takido. Non-covalent switch for intramolecular energy transfer. *Chemical Communications*, (5): 608–09, 2003.

[76] J. Otsuki, K. Narutaki, and J. M. Bakke. Light-triggered luminescence modulation using labile axial coordination to zinc-porphyrin. *Chem. Lett.*, 33(3): 356–57, 2004.

[77] G. G. Wildgoose, C. E. Banks, and R. G. Compton. Metal nanopartictes and related materials supported on carbon nanotubes: Methods and applications. *Small*, 2(2): 182–93, 2006.

[78] B. M. Quinn, C. Dekker, and S. G. Lemay. Electrodeposition of noble metal nanoparticles on carbon nanotubes. *J. Am. Chem. Soc.*, 127(17): 6146–47, 2005.

[79] Y. J. Xiong, I. Washio, J. Y. Chen, H. G. Cai, Z. Y. Li, and Y. N. Xia. Poly(vinyl pyrrolidone): A dual functional reductant and stabilizer for the facile synthesis of noble metal nanoplates in aqueous solutions. *Langmuir*, 22(20): 8563–70, 2006.

[80] M. Schlesinger and M. Paunovic. *Modern Electroplating, Wiley and Sons*, 2000.

[81] U. Schlecht, K. BalasubRamanian, M. Burghard, and K. Kern. Electrochemically decorated carbon nanotubes for hydrogen sensing. *Appl. Surf. Sci.*, accepted, 2007.

[82] B. M. Quinn and S. G. Lemay. Single-walled carbon nanotubes as templates and interconnects for nanoelectrodes. *Adv. Mater.*, 18(7): 855–+, 2006.

[83] I. Heller, J. Kong, H. A. Heering, K. A. Williams, S. G. Lemay, and C. Dekker. Individual single-walled carbon nanotubes as nanoelectrodes for electrochemistry. *Nano Letters*, 5(1): 137–42, 2005.

[84] A. Mooradian. Photoluminescence of metals. *Phys. Rev. Lett.*, 22(5): 185–89, 1969.

[85] G. T. Boyd, Z. H. Yu, and Y. R. Shen. Photoinduced luminescence from the noble-metals and its enhancement on roughened surfaces. *Phys. Rev. B*, 33(12): 7923–36, 1986.

[86] E. Dulkeith, T. Niedereichholz, T. A. Klar, J. Feldmann, G. von Plessen, D. I. Gittins, K. S. Mayya, and F. Caruso. Plasmon emission in photoexcited gold

nanoparticles. *Phys. Rev. B*, 70(20), 2004.

[87] M. Guerrisi, R. Rosei, and P. Winsemius. Splitting of interband absorption-edge in Au. *Phys. Rev. B*, 12(2): 557–63, 1975.

[88] S. Eustis and M. El-Sayed. Aspect ratio dependence of the enhanced fluorescence intensity of gold nanorods: Experimental and simulation study. *J. Phys. Chem. B*, 109(34): 16350–56, 2005.

[89] M. R. Beversluis, A. Bouhelier, and L. Novotny. Continuum generation from single gold nanostructures through near-field mediated intraband transitions. *Phys. Rev. B*, 68(11), 2003.

[90] P. Apell, R. Monreal, and S. Lundqvist. Photoluminescence of noble-metals. *Phys. Scr.*, 38(2): 174–79, 1988.

[91] C. Sonnichsen, T. Franzl, T. Wilk, G. von Plessen, and J. Feldmann. Plasmon resonances in large noble-metal clusters. *New J. Phys.*, 4, 2002.

[92] M. Scolari, T. Assmus, K. Balasubramanian, N. Fu, A. Myalitsin, A. Mews, M. Burghard, and K. Kern. Optical spectroscopy of individual carbon nanotubes with electrochemically deposited gold nanoparticles. *Nanoletters*, submitted, 2007.

[93] M. Veres, M. Fule, S. Toth, M. Koos, and I. Pocsik. Surface enhanced Raman scattering (SERS) investigation of amorphous carbon. *Diamond And Related Materials*, 13(4-8): 1412–15, 2004.

[94] Y. Maruyama, M. Ishikawa, and M. Futamata. Thermal activation of blinking in SERS signal. *J. Phys. Chem. B*, 108(2): 673–78, 2004.

[95] T. Assmus, K. BalasubRamanian, M. Burghard, K. Kern, M. Scolari, F. Nan, A. Myalitsin, and A. Mews. Raman properties of gold nanoparticle-decorated carbon nanotubes. *Appl. Phys. Lett.* 90 173109, 2007.

[96] S. Reich and C. Thomsen. Comment on polarized Raman study of aligned multiwalled carbon nanotubes. *Phys. Rev. Lett.*, 85(16): 3544–44, 2000.

[97] G. S. Duesberg, I. Loa, M. Burghard, K. Syassen, and S. Roth. Polarized Raman spectroscopy on isolated single-wall carbon nanotubes. *Phys. Rev. Lett.*, 85(25): 5436–39, 2000.

[98] H. X. Xu, J. Aizpurua, M. Kall, and P. Apell. Electromagnetic contributions to single-molecule sensitivity in surface-enhanced Raman scattering. *Physical Review E*, 62(3): 4318–24, 2000.

[99] K. Kneipp, H. Kneipp, and J. Kneipp. Surface-enhanced Raman scattering in local optical fields of silver and gold nanoaggregatess - from single-molecule Raman spectroscopy to ultrasensitive probing in live cells. *Acc. Chem. Res.*, 39(7): 443–50, 2006.

[100] A. Jorio, A. G. Souza, V. W. Brar, A. K. Swan, M. S. Unlu, B. B. Goldberg, A. Righi, J. H. Hafner, C. M. Lieber, R. Saito, G. Dresselhaus, and M. S. Dresselhaus. Polarized resonant Raman study of isolated single-wall carbon nanotubes: Symmetry selection rules, dipolar and multipolar antenna effects. *Phys. Rev. B*, 65(12), 2002.

[101] H. X. Xu and M. Käll. Polarization-dependent surface-enhanced Raman spectroscopy of isolated silver nanoaggregates. *Chemphyschem*, 4(9): 1001–05, 2003.

[102] http://www.bbigold.com. *British BioCell International*, 2006.

Publications

- Tilman Assmus, Kannan Balasubramanian, Marko Burghard, Klaus Kern, Matteo Scolari, Nan Fu, Anton Myalitsin and Alf Mews, Raman properties of gold nanoparticle-decorated individual carbon nanotubes, Applied Physics Letters **90**, 173109 (2007)

- Matteo Scolari, Tilman Assmus, Nan Fu, Anton Myalitsin, Alf Mews, Marko Burghard and Klaus Kern, Optical spectroscopy of individual carbon nanotubes with electrochemically deposited gold nanoparticles, submitted to Nano Letters (2007)

- Marko Burghard, Kannan Balasubramanian, Tilman Assmus, Alicia Forment-Aliaga, Eduardo Lee, Thomas Weitz, Matteo Scolari, Nan Fu, Alf Mews, and Klaus Kern, Electrochemically modified single-walled carbon nanotubes, submitted to Physica Status Solidi (c) (2007)

Tilman Assmus
Diplom-Physiker (M.Sc.)

Personal Information

date of birth	30 December, 1975
place of birth	Frankfurt am Main, Germany
nationality	German
personal status	unmarried
address	Hirschsprung 12 70569 Stuttgart, Germany

Education

2003-current	**PhD studies in Physics**, *Max-Planck-Institute for Solid State Research, Stuttgart, Germany and École Polytechnique Fédérale de Lausanne (EPFL),Lausanne Switzerland*. Thesis title: "Carbon nanotubes functionalized with dye molecules and metal nanoparticles" Thesis advisor: Dr. Marko Burghard Thesis supervisor: Prof. Dr. Klaus Kern
1996-2002	**Physics studies**, *University of Technology Darmstadt, Germany*. Master thesis title: "Aperiodic stochastic resonance in a Shinriki-type oscillator" Thesis supervisor: Prof. Dr. H. Benner Master thesis grade: 1.0 ("Very Good") Overall grade: "Very Good"
1995-1996	**alternative civilian service**, *First aid instructor for Johanniter-Unfall-Hilfe e.V.*.
1987–1995	**High School (Gymnasium)**, *Otto-Hahn-Schule, Hanau, Germany*. Average grade: 1.0
1982–1986	**Primary School**, *Erich-Kästner-Schule, Hanau, Germany*.

Acknowledgements